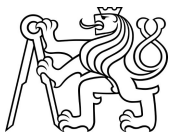

CZECH TECHNICAL UNIVERSITY IN PRAGUE

FACULTY OF BIOMEDICAL ENGINEERING
Department of Biomedical Technology

A Feasibility Study of Microwave Temperature Monitoring in the Pelvic Region During Regional Microwave Hyperthermia Treatment

Studie proveditelnosti mikrovlnného monitorování teploty v oblasti pánve léčené regionálním mikrovlnným hypertermickým systémem

Master's Thesis

Study Programme: Biomedical Engineering
Field of Study: Biomedical Engineer

Supervisor: doc. Dr.-Ing. Jan Vrba, M.Sc.
Consultant: Ing. Ondřej Fišer, Ph. D., Lorenzo Crocco, Ph. D. (IREA - Institute for the Electromagnetic Sensing of the Environment)

Bc. Hana Mózerová

Kladno 2020

MASTER'S THESIS ASSIGNMENT

I. PERSONAL AND STUDY DETAILS

Student's name:	**Mózerová Hana**	Personal ID number:	**434206**
Faculty:	**Faculty of Biomedical Engineering**		
Department:	**Katedra biomedicínské techniky**		
Study program:	**Biomedicínská a klinická technika**		
Branch of study:	**Biomedicínský inženýr (CEMACUBE)**		

II. MASTER'S THESIS DETAILS

Master's thesis title in English:

A Feasibility Study of Microwave Temperature Monitoring in the Pelvic Region During Regional Microwave Hyperthermia Treatment

Master's thesis title in Czech:

Studie proveditelnosti mikrovlnného monitorování teploty v oblasti pánve léčené regionálním mikrovlnným hypertermickým systémem

Guidelines:

Create an analytical layered 1D model and a numerical anatomically realistic 2D model of the pelvic region to evaluate the main parameters of electromagnetic wave propagation in this region. Using these models, determine the main guidelines to the design of the imaging device, that is frequency bands, the dielectric parameters of the matching medium, and the appropriate number of antenna elements. Validate the obtained guidelines with extended numerical simulations on anthropomorphic phantom. Design and implement a modification of an existing water phantom of the pelvic region so that it is possible to change the values of the dielectric parameters in a certain part of its volume to mimic the local temperature increase. Next, design an imaging system antenna array with suitable antenna elements and prepare a methodology for measuring S-parameters of the imaging system for various phantom configurations. Create a corresponding numerical model of the antenna array and phantom and calculate synthetic S-parameters. Use suitable differential microwave imaging algorithms to reconstruct changes in dielectric parameters from synthetic data mimicking regional microwave hyperthermia in the pelvic region.

Bibliography / sources:

[1] Raquel Cruz Conceicao, Johan Jacob Mohr, Martin O'Halloran, An Introduction to Microwave Imaging for Breast Cancer Detection, ed. 1st, Springer, 2016, 144 s., ISBN 978-3-319-27866-7
[2] Matteo Pastorino, Microwave Imaging, ed. 1st, John Wiley & Sons, Inc., 2010, ISBN 978-0-470-27800-0

Name of master's thesis supervisor:

doc. Dr.-Ing. Jan Vrba, MSc.

Name of master's thesis consultant:

Ing. Ondřej Fišer, Ph.D., Lorenzo Crocco, PhD (IREA - Institute for the Electromagnetic Sensing of the Environment)

Date of master's thesis assignment: **10.02.2020**
Assignment valid until: **19.09.2021**

Peter Kneppo Digitálně podepsal Peter Kneppo Datum: 2020.05.15 20:33:13 +02'00'

prof. Ing. Peter Kneppo, DrSc., dr.h.c.
Head of department's signature

prof. MUDr. Ivan Dylevský, DrSc. Digitálně podepsal prof. MUDr. Ivan Dylevský, DrSc. Datum: 2020.05.18 12:57:10 +02'00'

prof. MUDr. Ivan Dylevský, DrSc.
Dean's signature

III. PŘEVZETÍ ZADÁNÍ

Student(ka) bere na vědomí, že je povinnen(a) vypracovat diplomovou práci samostatně, bez cizí pomoci, s výjimkou poskytnutých konzultací. Seznam použité literatury, jiných pramenů a jmen konzultantů je třeba uvést v diplomové práci.

19.05.2020
Datum převzetí zadání

Podpis studenta(ky)

Declaration

I hereby declare that I have completed this thesis entitled "A Feasibility Study of Microwave Temperature Monitoring in the Pelvic Region During Regional Microwave Hyperthermia Treatment" independently and that I have listed all the literature and publications used.
I have no objection to usage of this work in compliance with the act §60 Zákon č. 121/2000Sb. (copyright law), and with the rights connected with the copyright act including the changes in the act.

Kladno May 21, 2020 ..... Hana Mózerová

Aknowledgements

I wish to express my deepest gratitude to my supervisor, doc. Dr.-Ing. Jan Vrba, M.Sc., for providing me invaluable guidance throughout this research. My sincere thanks also go to Lorenzo Crocco, Ph.D. and Rosa Scapaticci, Ph.D. for hosting my intership and for their continued support and encouragement. I would also like to thank Ing. Ondřej Fišer, Ph.D. and Ing. Jan Tesařík for their advices regarding the design of the experiment. Last but not least, I am extremely grateful to my parents who always supported and motivated me in my studies and to my boyfriend and friends for understanding, patience and cheering me up.

Abstract

The Master's thesis deals with the analysis of the feasibility of non-invasive 3D temperature measurement during microwave regional hyperthermia in the pelvic region using differential microwave imaging.

The main goal was to determine whether it is possible to detect qualitatively and quantitatively small changes in dielectric properties resulting from changes in tissue temperature in the area treated with hyperthermia using differential microwave imaging.

For this purpose, a 1D layered and 2D anthropomorphic numerical model of electromagnetic wave propagation in the pelvic region were gradually created. These temperature dependent models were used to analyze the influence of various parameters of microwave imaging and temperature contrast reconstruction using the distorted Born approximation (DBA) and TSVD regularization.

The analysis of these models showed that the most suitable operating frequencies are between 0.5 and 1.2 GHz, while with increasing frequency it is advantageous to use a matching medium with decreasing permittivity.

The results are similar for full and empty bladders.

Data obtained from 2D numerical simulations considering scenarios that are different in location, size and temperature change of a heated tissue have been used for reconstruction of a contrast in dielectric properties. The algorithm based on DBA and TSVD was able to detect temperature change higher than 3 °C with 35-70 % sensitivity, 4 mm localization error and NRMSE around 0.2. Also hot spots occurring simultaneously with a desirable hyperthermia heating were detected successfully.

An experiment validating the results of the synthetic analysis was designed, modelled in 3D and simulated numerically. In this case, the imaging algorithm didn't show satisfying results, which was probably caused by a low energy of the waves penetrated into the phantom.

Keywords

Microwave imaging, hyperthermia, inverse scattering, distorted Born approximation, TSVD regularization

Abstrakt

Diplomová práce se zabývá analýzou proveditelnosti 3D neinvazivního měření teploty během regionální mikrovlnné hypertermie v oblasti pánve pomocí diferenčního mikrovlnného zobrazování.

Hlavním cílem práce bylo určit, zda je možné detekovat jak kvalitativně, tak kvantitativně malé změny v dielektrických vlastnostech, které jsou výsledkem změn v teplotě tkáně v místě léčby hypertermie při použití diferenčního mikrovlnného zobrazování.

Pro tento účel byl postupně vytvořen 1D vrstevnatý a 2D numerický anatomicky věrný model představující oblast šíření elektromagnetických vln. Tyto teplotně závislé modely byly použity k analýze vlivu různých parametrů mikrovlnného zobrazování a rekonstrukce teplotního kontrastu pomocí zkreslené Bornovy aproximace (DBA) a TSVD regularizace.

Z analýzy těchto modelů vyplývá, že nejvhodnější pracovní frekvence jsou v rozmezí od 0,5 do 1,2 GHz, zatímco se vzrůstající frekvencí je výhodné použít pracovní prostředí o vyšší relativní permitivitě.

Mezi výsledky plného a prázdného močového měchýře nebyla zjištěna žádná výraznější změna.

Data získaná z 2D numerických simulací uvažujících scénáře lišící se v umístění, velikosti a teplotní změně zahřívané tkáně byla použita k rekonstrukci kontrastu v dielektrických vlastnostech. Algoritmus založený na DBA a TSVD byl schopen detekovat teplotní změnu vyšší než 3 °C s $35 - 50\%$ senzitivitou, chybou lokalizace 4 mm a normalizovaným kvadratickým průměrem odchylek zhruba 0,2. Úspěšně byla také detekována nežádoucí horká místa, tzv. hot-spoty, vzniklá souběžně s žádoucím hypertermickým zahříváním.

Dále byl navržen pokus validující výsledky analýzy na syntetických datech, který byl následně numericky modelován a simulován ve 3D. V tomto případě nebyly výsledky zobrazovacího algoritmu uspokojivé, což bylo pravděpodobně způsobeno nízkou energií elektromagnetických vln pronikajících do fantomu.

Klíčová slova

Mikrovlnné zobrazování, hypertermie, inverzní rozptyl, zkreslená Bornova aproximace, TSVD regularizace

Contents

List of symbols and abbreviations

List of abbreviations

MWI	microwave imaging
CT	computed tomography
MRI	magnetic resonance imaging
EM	electromagnetic
SAR	specific absorption rate
S-parameters	scattering parameters
MWT	microwave tomography
MoM	method of moments
FEM	finite element method
S	scattering matrix
DBA	distorted Born approximation
TSVD	truncated singular value decomposition
SNR	signal-to-noise ratio
IPA	isopropyl alcohol
DAK	Dielectric Assessment Kit
CTU	Czech Technical University
NRMSE	normalized root mean square error
RMSE	root mean square error
UWB	ultra-wide band

List of symbols

ω	$(\mathrm{rad} \cdot \mathrm{s}^{-1})$	angular frequency
$\boldsymbol{\epsilon_r}$	$(-)$	complex relative permittivity
ϵ_{r_∞}	$(-)$	relative permittivity at high frequencies
$\Delta\epsilon_r$	$(-)$	magnitude of the dispersion
τ	(s)	relaxation time
σ_i	$(\mathrm{S} \cdot \mathrm{m}^{-1})$	static ionic conductivity
ϵ_0	$(\mathrm{F} \cdot \mathrm{m}^{-1})$	permittivity of vacuum
ϑ	(°C)	temperature
ϵ_r'	$(-)$	relative permittivity
ϵ_r''	$(-)$	relative dielectric loss
f	(Hz)	frequency
λ	(m)	wavelength
$\boldsymbol{Z}$		impedance
μ_0	$(\mathrm{H} \cdot \mathrm{m}^{-1})$	permeability of vacuum
$\boldsymbol{\gamma}$	$(\mathrm{rad} \cdot \mathrm{m}^{-1})$	complex propagation constant
$\boldsymbol{\Gamma}$	$(-)$	reflection coefficient
$\boldsymbol{T}$	$(-)$	power transmission coefficient
J	$(-)$	normalized magnitude of induced current density
$\mathbf{S}_{\vartheta_n}$	$(-)$	scattering matrix at n^{th} temperature state
TP	(-)	true positive
TN	(-)	true negative
FP	(-)	false positive
FN	(-)	false negative
u_A	(-)	type A uncertainty
u_B	(-)	type B uncertainty
u_C	(-)	type C uncertainty

Chapter 1

Introduction

Microwave imaging (MWI) is a promising tool in many medical applications. It uses non-ionizing low power electromagnetic signals in the frequency range from hundreds of MHz to few GHz that makes the technique not harmful for patients health. Other advantages are low manufacturing and working costs and small dimensions of the devices. MWI devices are easily portable and thanks to that available almost every time and everywhere it is needed. On the other hand, as compared to other technologies used for medical imaging (such for instance computed tomography (CT) or magnetic resonance imaging (MRI)), MWI has an intrinsic limitation in terms of achievable spatial resolution. [1]

The reason why it is possible to image biological tissues through MWI is their variation in dielectric properties. The electromagnetic (EM) waves propagating through the material are scattered on each interface of two different permittivity and conductivity levels, are attenuated and their phase rotates. Thanks to this fact, MWI can be used for example for detecting brain strokes or tumors of different type. The temperature dependence of dielectric properties of tissues indicates another possible application of MWI as it can bring an improvement of an useful auxiliary medical cancer treatment called hyperthermia. [2]

Hyperthermia complements commonly used cancer treatments such as radiotherapy and chemotherapy making them more effective. Through delivering an energy to specific region, the tissue is heated and becomes more susceptible to the basic applied treatment. To be successful, hyperthermia should focus the EM energy in the region to be treated without heating other parts of the body, which causes patients discomfort or pain. [3]

With the help of real time temperature monitoring the undesirable effects could be avoided and MWI appears to be an useful tool to fulfil this task effectively [4].

1.1 State of the art

Hyperthermia is gaining an increasing relevance in the clinical practice as an adjuvant anti-cancer therapy, thanks to its demonstrated capability of enhancing the effectiveness of radiotherapy and chemotherapy [3]. In particular, the therapeutic goal is to drive the region under treatment to a supraphysiologic temperature (between 40 and 48 °C) [5] by conveying therein the energy radiated by an applicator, typically consisting of a properly fed phased array. Malignant cell's proteins heated to the hyperthermia range denaturate and subsequently destabilize the intracelular environment together with DNA repair system [5]. Damage to the cancerous cells is magnified also by environmental and vascular conditions. In healthy tissue, the dilating vessels increase the blood flow in the region and so decrease the temperature. In a tumor, the pathological vessels are not able to dilate which causes higher sensitivity to the heat [5].

There appear to be three different methods of hyperthermia treatment depending on location, depth and staging of the tumor: local, regional and whole-body hyperthermia. Deep seated tumors located in the pelvic region, such as cervical, rectal, bladder or prostate cancer, belong to the regional type of treatment [5]. It was demonstrated in [6] that in case of cervical, rectal and bladder cancer adding the hyperthermia to radiotherapy treatment increases the therapeutic response (the disappearance of all signs of cancer in response to treatment) from 39 to 55 %. In 2017, more than 1.7 million people died due to the cancer in the pelvic region worldwide, more than 7 thousands in Czech republic for the same reason [7]. Although these types of cancer show higher five year survival rate than many other types in case of Czech republic, their values (prostate - 83.1%, cervix - 64.5%, rectum - 50.3% [7]) could be enhanced.

Effect of hyperthermia is strongly dependent on the temperature delivered in the tumor [3] but the controlled administration of the electromagnetic energy is a complicated task and undesirable underheating of tumor or overheating of healthy tissue can appear. The overheated areas - so called hot spots - mainly occur at tissue interfaces due to large variations in tissue properties [3]. While a small increase in temperature has no permanent effect on the patient, development of hot spots may lead to patient discomfort or even pain [8] which impairs the optimal hyperthermia treatment. To overcome such undesirable side effects, a water bolus placed between the applicator and the body is typically used to avoid the exceeding heating of the tissue located close to the antennas, whereas patient-specific

treatment planning procedures are exploited to control the power deposition inside the body and therefore maximize the effect in the target area while reducing occurring of unwanted hot spots elsewhere.

While the above procedures have certainly contributed to increase the confidence in hyperthermia as a reliable clinical tool, still there is a room for improvement. As a matter of fact, in the current clinical practice, patient complaints during the treatment are handled by rerunning the treatment planning on the fly to adjust some parameters (e.g. in an optimization framework by penalizing power deposition in a healthy area which the patient feels as too heated). For example in [9] data from 35 cervical tumor patients treated with deep hyperthermia controlled by extensive treatment planning showed that the patient pain is very common. Average number of patient complaints per treatment was 13.3. The majority of complaints occurred in the abdomen and lower back which is most likely caused by the anatomy of the pelvic bones. Canters et al. [9] summed up the factors which are involved in optimizing of the specific absorption rate (SAR) distribution: patient and model related. Patient's ability to localize the hot spot depends on the innervation which differs from region to region and may be damaged. The patients sensitivity varies from person to person and can be influenced by other factors like blood perfusion [10]. Last but not least, the accuracy of the positioning of the patient, the accuracy of amplitude and phase settings and uncertainty in dielectric properties of the tissues complicate the correct treatment planning.

Due to these facts, the safe clinical application of hyperthermia requires control of the administrated temperature [11]. Tools for this control would indeed allow an objective assessment of what is otherwise prone to patient subjective perceptions. In the practice this is typically done by using invasive techniques - catheters with temperature probes, which need to be in the contact with the measured target. The invasiveness is their main drawback and this is why it is not possible to monitor the temperature in a large number of points due to the clinical trauma [12]. Two main invasive sensors are used in clinical treatment. The first sensors are thermocouples which are cost-effective, quite accurate with wide measurement range. Their small size also allows a quick response to the changes. On the other hand, their metallic structure highly absorbs the radiation which increases local temperature and causes a significant overestimation of the values [12]. Second, fiber-optic sensors have gained more attention in the last two decades due to their increasingly reduced cost. Rapid response, electromagnetic inert nature, biocompatibility and chemical inertness make these sensors

more practical, on the other side, artefacts induced by organ movements or by encapsulation in black-pigmented coating complicates the application [12].

In order to improve the patient's comfort and reliability of the treatment, there is a large attention in developing non-invasive tools capable of in-line monitoring of the temperature evolution during the treatment possibly by producing images. Even though CT-based thermometry is not invasive and there is temperature and CT-value relationship [13], the ionizing radiation discourages the clinicians from using this method on patients. Ultra-sound based thermometry is promising thanks to real time visualisation capabilities and the widespread availability of the ultrasound technology [12]. However, artefacts caused by breathing and pulse and necessity of prior knowledge speed of sound and thermal-expansion coefficients must be taken into account [14]. Magnetic Resonance Imaging (MRI) has been considered in this framework and it is certainly a promising tool, given the remarkable capabilities of MRI and its being well know by clinicians [11]. However, besides the cost factor, MRI requires development of specialized hyperthermia applicators that can work within the MRI coils without interfering with its operation [15].

As an alternative, it is possible to consider the fact that temperature variations correspond to (more or less slight) variations of the electromagnetic properties of the heated tissue [16]. As such, it is possible to exploit microwave imaging to pursue the task and take an advantage from its noninvasiveness, cost-effectivity and transportability. Such an idea has been indeed explored in microwave hyperthermia using broadband devices [17], as well as in the monitoring of head and neck hyperthermia [2] and breast hyperthermia [4]. Also, an experimental demonstration of the possibility of tracking temperature-induced changes of EM properties has been given for the case of ablation, which is another microwave-based thermal treatment wherein higher temperatures are achieved to produce an irreversible damages of the heated tissue [18]. Furthermore, an animal experiment has been conducted using antenna array in the frequency range of 300 MHz to 1 GHz and surgically implanted tube with temperature controlled saline [19]. The system was able to image the decrease of conductivity and increase of permittivity with descending temperature. The same authors also constructed and tested microwave imaging temperature monitoring system combined with focused ultrasound heating [20]. In this case, indirect linear relationship between the retrieved conductivity and actual temperature was proven. Lastly, numerical simulations and phantom experiments [21], concerned with the possibility to image temperature in pelvic region and thorax, reported that the Born approximation algorithm is capable to monitor

temperature changes in homogeneous medium only in the form of qualitative images. Moreover, in inhomogeneous scenarios like pelvic region, many artefacts distort the results. In the subsequent study an iterative algorithm [22] was applied for imaging the permittivity quantitatively in the whole thorax region at the cost of a huge computational time and amount of memory [23], which makes the method not practical in clinical hyperthermia treatment.

Although the feasibility of microwave temperature imaging in pelvis region treatment has been tested [21], this is still an open issue. In the thesis, we deal with the same problem but using probably different techniques in both synthetic and experimental analysis. In this area, still no quantitative images were achieved not even a relationship between the imaged properties and temperature was proposed. Also, the use of different robust and fast imaging algorithms for the case of pelvic organs is worth trying.

1.2 The goals of the thesis

The main goal of this thesis was to conduct a feasibility study of microwave temperature monitoring in the pelvic region during regional microwave hyperthermia treatment. The aim was to prove, that a microwave imaging system can be capable of detecting slight changes in dielectric properties arising due to the temperature change. Next, that there is an imaging algorithm which gives quantitative results and has a potential to be calibrated to accurately appraise the value of the temperature. In order to fulfil the main goals, the partial goals were set. First, creating an analytical layered 1D model and a numerical anatomically realistic 2D model of the pelvic region. Using these models, proper working conditions can be set, such as working frequency, properties of the matching medium and number of transmitting and receiving antennas. Validation of the obtained guidelines with extended numerical simulations on antropomorphic phantom should support the implementation of the experiment. Appropriate differential imaging algorithm should be applied on data from the simulations and the results should be evaluated.

After the synthetic analysis, the experiment should be designed which in the beginning requires a suitable antenna element design with respect to known proper frequency and matching medium properties. As a next step, the previous projects [24, 25], the prototype of a regional hyperthermia system and water phantom of the pelvic region, should be modified. The antenna holder should be optimized for antennas incorporation and the water phantom

should enable to change dielectric properties in a certain part of its volume to mimic the local temperature increase. The appropriate methodology for preparing a liquid phantom must be designed, which includes proper materials choice and finding their optimal ratio.

When the experiment is designed, the goal is to build a corresponding 3D numerical model of the system and use it for calculation of the synthetic S-parameters when different size and locations of the hyperthermia target are mimicked. The data should be processed by imaging algorithm and a final image of dielectric properties change should be gained and evaluated. The differences between the 2D antropomorphic and 3D homogeneous results should be discussed.

Chapter 2

Methods

2.1 Numerical phantom

As a main organ of interest in our analysis, the urinary bladder was chosen. In order to analyze the effect of the working frequency and matching medium on the capability of waves to penetrate into the body and probe the bladder, we set a scenario in which the Zubal's numerical phantom was used [26]. This 3D phantom of the whole human body consists of voxels having the size of 4 mm which represent different human tissues. A horizontal cross section in which the bladder is located has been selected while a missing skin layer was added all around the body. According to [27], the average skin thickness is 2.3 mm, so after increasing the resolution of the original phantom, the thickness of the skin layer was set to 2 mm. Whole pelvic cross section of the phantom is shown in Fig. 2.1, the bladder is highlighted in yellow.

Dielectric properties of different tissues are changing according to the frequency of the electromagnetic waves. The tissue properties in the numerical phantom were modelled dependent on angular frequency ω by using the single-pole Cole-Cole model.

$$\boldsymbol{\epsilon_r}(\omega) = \epsilon_{r_\infty} + \frac{\Delta\epsilon_r}{1 + i\omega\tau^{1-\alpha}} + \frac{\sigma_i}{i\omega\epsilon_0}, \tag{2.1}$$

where ϵ_{r_∞} is relative permittivity at high frequencies, $\Delta\epsilon$ the magnitude of the dispersion, τ the relaxation time, α the parameter that allows for the broadening of the dispersion, σ_i static ionic conductivity and ϵ_0 is permittivity of vacuum. The parameters can be found in

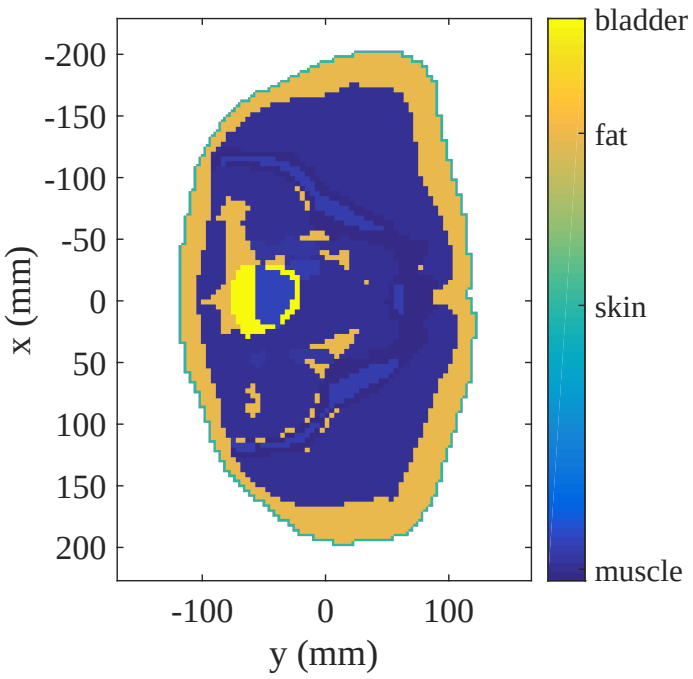

Figure 2.1: Cross section of Zubal's phantom in the region of bladder. The bladder is highlighted in yellow [26].

the literature [28] and for reader's convenience, the parameters for the tissues involved in the signal penetration analysis are displayed in Table 2.1.

Table 2.1: Cole-Cole parameters of the tissues included in 1D model [28]

tissue	skin	fat	muscle	bladder wall
ϵ_{r_∞}	4	2.5	4	2.5
$\Delta\epsilon_r$	32	3.0	50	16
$\tau(ps)$	7.23	7.96	7.23	8.842
α	0	0.2	0.10	0.1
$\sigma_i(S/m)$	0.002	0.01	0.2	0.2

Another important material which has to be considered is urine and its Cole-Cole parameters can be also found in [28]. However, this model gives at 1 GHz frequency a value of 35.75 which is too low for a tissue consisting in 95 % of water. For this reason, we have considered another study which investigated human urine dielectric properties [29]. In this work, the properties were measured at different temperatures (one of them was 37 °C) and

the results were fit with a single-pole Debye model. The Debye model looks similarily to the Cole-Cole model (see 2.1) but assumes $\alpha = 0$. Although the Cole-Cole model is respected as the most reliable fitting technique to describe the change in dielectric properties, the study [30] showed that the Debye model is accurate enough for a large class of actual wideband sources. Even in case of materials containing mainly one type of molecules, the Debye parameters are more suitable for permittivity dependence modelling than Cole-Cole parameters (personal communication with doc. Dr.-Ing. Jan Vrba, M.Sc., November 15, 2019). Despite such an inconsistency, the Debye model was used for modelling the urine.

As mentioned above, dielectric properties of different tissues are not only dependent on the frequency of electromagnetic waves, but also on the temperature [16]. The complex relative permittivity $\boldsymbol{\epsilon_r}$ and the effective conductivity σ with respect to angular frequency ω and temperature ϑ are expressed as [16]:

$$\boldsymbol{\epsilon_r}(\omega, \vartheta) = \epsilon_r'(\omega, \vartheta) - i\epsilon_r''(\omega, \vartheta) \tag{2.2}$$

$$\sigma(\omega, \vartheta) = \omega\epsilon_0\epsilon_r''(\omega, \vartheta), \tag{2.3}$$

where ϵ_r' represents the relative permittivity and ϵ_r'' the relative dielectric loss.

In the study [16], the two-pole Cole-Cole model was determined to enable to calculate the relative permittivity and effective conductivity at any frequency and temperature in a range between 0.5 GHz and 7 GHz and between 30 and 50 °C , respectively. The two-pole Cole-Cole model (see Eq. 2.4) was chosen according to the electromagnetic bandwidth

$$\boldsymbol{\epsilon_r}(\omega, \vartheta) = \epsilon_{r_\infty}(\vartheta) + \frac{\Delta\epsilon_{r,1}(\vartheta)}{1 + i\omega\tau_1(\vartheta)^{1-\alpha_1}} + \frac{\Delta\epsilon_{r,2}(\vartheta)}{1 + i\omega\tau_2(\vartheta)^{1-\alpha_2}} + \frac{\sigma_s}{i\omega\epsilon_0}. \tag{2.4}$$

In [16], the Cole-Cole parameters were fit to the experimental data and a second order polynomial was used to fit the temperature dependency of the Cole-Cole parameters 2.5.

$$\begin{aligned}
\epsilon_{r_{\infty,fit}}(\vartheta) &= A_1\vartheta^2 + B_1\vartheta + C_1 \\
\Delta\epsilon_{r_{1,fit}}(\vartheta) &= A_2\vartheta^2 + B_2\vartheta + C_2 \\
\tau_{1,fit}(\vartheta) &= A_3\vartheta^2 + B_3\vartheta + C_3 \\
\Delta\epsilon_{r_{2,fit}}(\vartheta) &= A_4\vartheta^2 + B_4\vartheta + C_4 \\
\tau_{2,fit}(\vartheta) &= A_5\vartheta^2 + B_5\vartheta + C_5 \\
\sigma_{s,fit}(\vartheta) &= A_6\vartheta^2 + B_6\vartheta + C_6
\end{aligned} \tag{2.5}$$

Aiming to keep the method more consistent, only one-pole model for temperature dependence was implemented, in other words, the coefficients $\Delta\epsilon_{r_2}, \tau_2$ and α_2 were neglected. The reason was that in the case of urine, only one-pole coefficients are known and the implementation is less complicated. Also, the difference between the one and two-pole model is negligible.

Because in the study [16] the bladder was not measured (only liver, muscle, fat and blood), we had to find the way to model the other tissues, especially bladder wall. The first idea was to choose one known tissue which has the most similar behaviour to the unknown. The anatomical structure of the urinary bladder wall consists of layers while the principal layer is made up of the smooth fibres (detrusor muscle) which are arranged in the layer in three different ways [31]. This indicates, that the muscle tissue is the closest approximation. However, we displayed the real and imaginary part of the complex permittivity of tissues on different frequencies using the not temperature dependent single-pole Cole-Cole model (Fig. 2.2) and it is clear, that the properties of a bladder differ from the measured tissues significantly. Due to this fact, different approach was searched for estimation the changes of the properties in temperature variance.

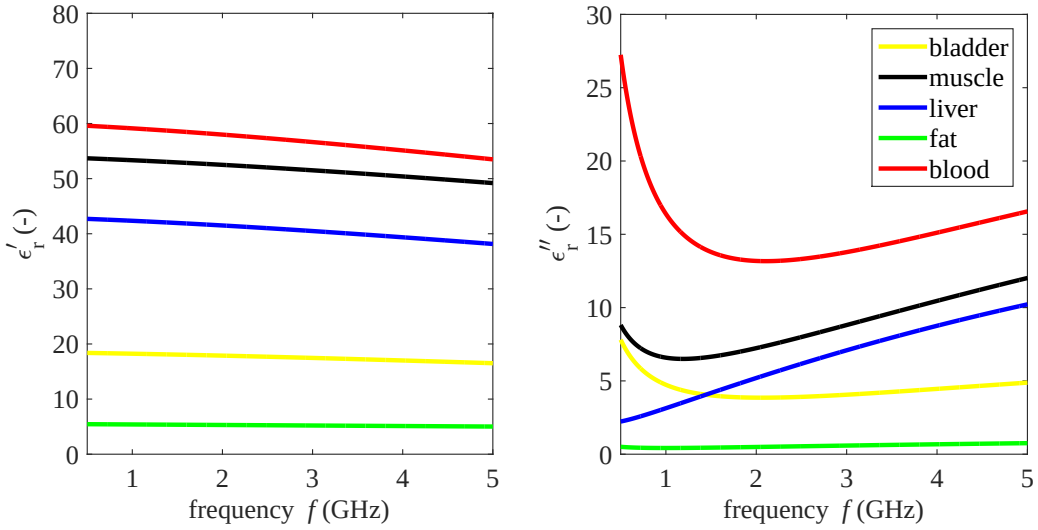

Figure 2.2: Comparison of complex permittivity of different tissues using single-pole Cole-Cole model

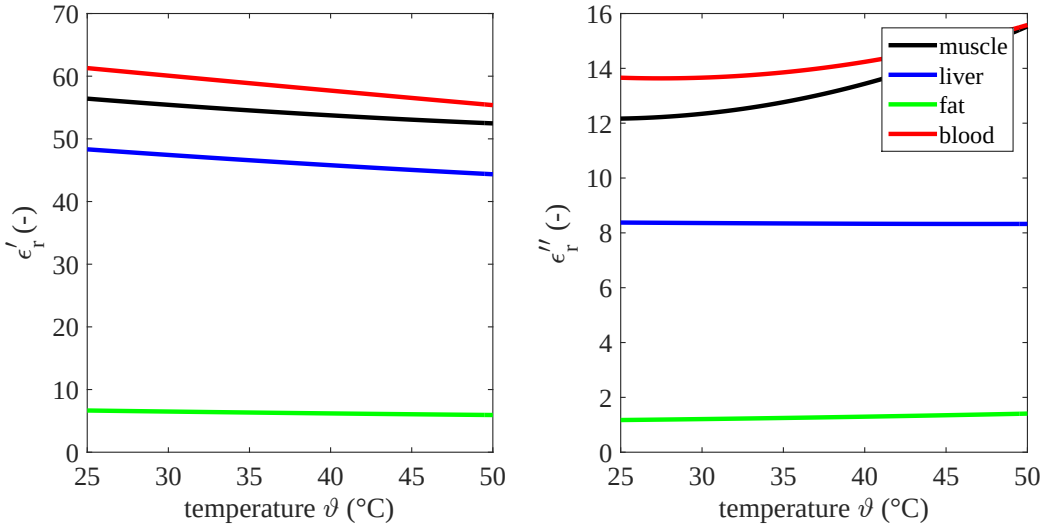

Figure 2.3: Dependence of complex permittivity on temperature for 4 different tissues (1 GHz)

The temperature dependence of the complex permittivity of 4 different tissues for the frequency of 1 GHz calculated using the equations proposed in [16] are shown in Fig. 2.3.

Since the dependencies are almost linear, we fitted the points by a linear function, found the slope for each tissue and the mean of all the slopes was used for modelling of the dependence of other tissues of interest. As a starting point we considered the result of single-pole Cole-Cole model at given frequency which corresponds to the temperature 25 °C for bladder and intestine tissue and the Debye model at given frequency which corresponds to temperature 37 °C for urine. All these was calculated in complex numbers so both the relative permittivity and electric conductivity were obtained.

This method was used for modelling parameters of bladder, urine and intestine because these tissues are located in the region which is mainly heated. The skin, the bone, the bone marrow and the spinal chord were not calculated as dependent on the temperature, because we assume that first they are not heated on purpose and second they are not close to the bladder. In case of the 4 tissues known from [16], we used the A, B and C parameters (Eq. 2.5) for changing Cole-Cole parameters.

Since the bladder's function is storage of urine and emptying, smooth muscles of the bladder (detrusors) serve for the switching between these two states. Storage of urine occurs at low pressure, which implies that the bladder relaxes during the filling phase and the muscles contract when the bladder is full and the urine needs to be pushed to urethra. [32]

When modelling an empty bladder, the same pixel phantom was used as for a full one, but considering that empty bladder is much smaller than the full one and having thicker wall, the interior of the bladder was determined as bladder wall and the former bladder got properties of muscle tissue surrounding it.

In Figs. 2.4 and 2.5, the relative permittivity and the equivalent conductivity in the 2D phantom are displayed in case of full and empty bladder, respectively.

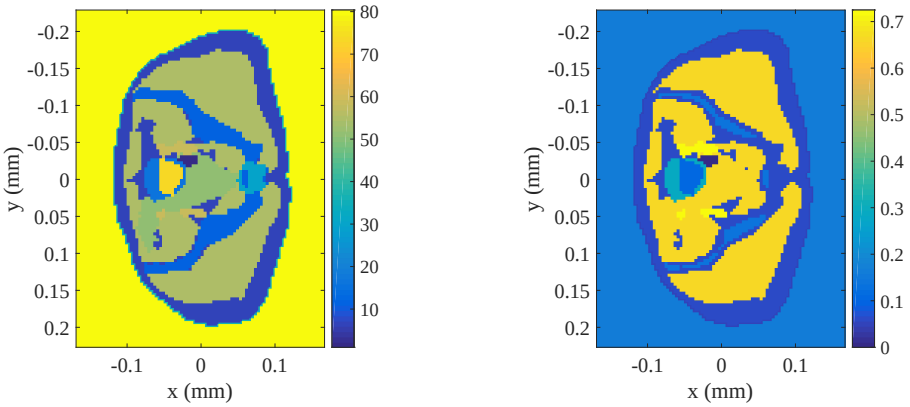

(a) Relative permittivity ϵ_r (-) (b) Equivalent conductivity σ (S/m)

Figure 2.4: Relative permittivity and the equivalent conductivity in the 2D phantom of pelvic region (frequency = 800 MHz) - full bladder

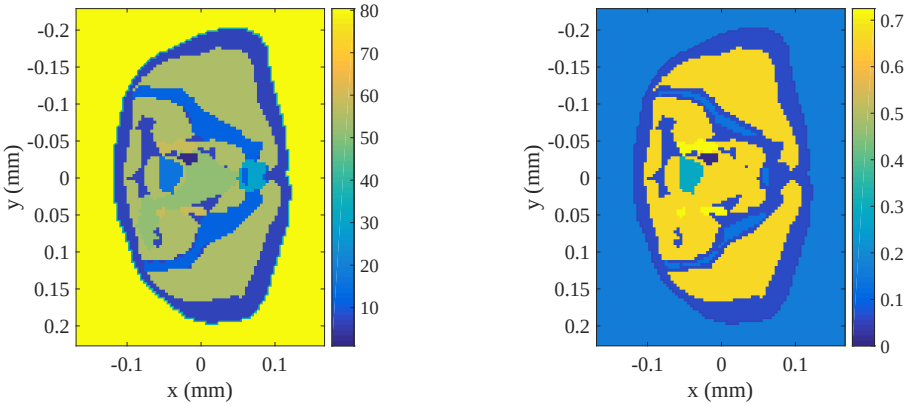

(a) Relative permittivity ϵ_r (-) (b) Equivalent conductivity σ (S/m)

Figure 2.5: Relative permittivity and the equivalent conductivity in the 2D phantom of pelvic region (frequency = 800 MHz) - empty bladder

2.2 1D analytical analysis

In [33], a simple design tool was introduced which enables to find the proper working conditions for microwave tomography (MWT). The tool searches for an optimal working frequency and electric properties of a matching medium such that the maximum amount of incident power penetrates into the imaged area, a meaningful backscattered signal arises and the spatial resolution is high as much as possible. The transmitted power in a stratified medium impinged by a plane wave was analysed using transmission line model in Fig. 2.6 being considered equivalent to the layered model. The formulas needed to the analysis are described on following pages [34].

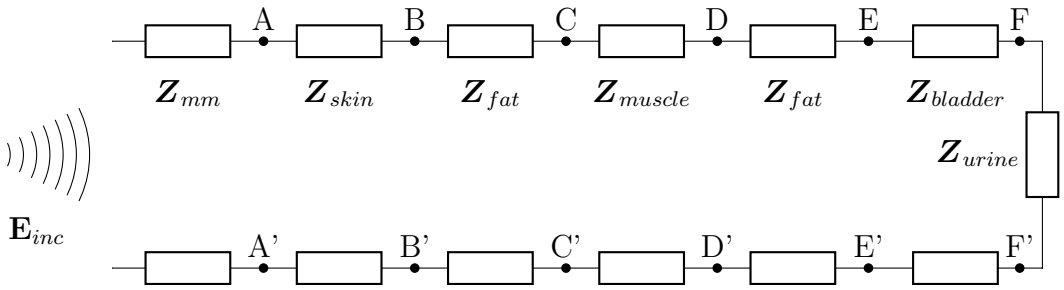

Figure 2.6: Equivalent transmission line model for pelvic region with full bladder (inspired by [33]).

The characteristic impedance of every tissue is given by $\boldsymbol{Z}_n = \sqrt{\frac{\mu_0}{\epsilon_0 \boldsymbol{\epsilon_{r,n}}}}$, where $\boldsymbol{\epsilon_{r,n}}$ is the complex relative permittivity of the n^{th} tissue.

Characteristic impedance of the matching medium is calculated as:

$$\boldsymbol{Z}_{mm} = \sqrt{\frac{\mu_0}{\epsilon_0(\epsilon_{r,mm} - \frac{i\sigma_{mm}}{\omega\epsilon_0})}}. \tag{2.6}$$

Once the overall scenario has been set, the impedance of the interface between matching medium and the first tissue (skin) has been calculated by means of the impedance transfer equation for lossless media.

$$\boldsymbol{Z}_T = \boldsymbol{Z}_{line}\frac{\boldsymbol{Z}_{load} + \boldsymbol{Z}_{line}\tanh(\boldsymbol{\gamma}_n l_n)}{\boldsymbol{Z}_{line} + \boldsymbol{Z}_{load}\tanh(\boldsymbol{\gamma}_n l_n)}, \tag{2.7}$$

where $\boldsymbol{Z}_T$ is an impedance at the input of the transmission line, $\boldsymbol{Z}_{line}$ is the characteristic impedance of the tissue behind the interface, $\boldsymbol{Z}_{load}$ is the impedance impedance at the

output of a particular layer, l_n is the thickness of the tissue behind the interface and $\boldsymbol{\gamma}_n$ is the complex propagation constant of the tissue behind the interface defined as

$$\boldsymbol{\gamma}_n = i\sqrt{\mu_0 \boldsymbol{\epsilon_{r,n}} \epsilon_0}\omega. \tag{2.8}$$

The Eq. 2.7 is calculated repeatedly starting with $\boldsymbol{Z}_{urine}$ as $\boldsymbol{Z}_{load}$, which is gradually transformed into the AA' interface. As a next step, reflection coefficient on the interface AA' is calculated as

$$\boldsymbol{\Gamma} = \frac{\boldsymbol{Z}_{AA'} - \boldsymbol{Z}_{mm}}{\boldsymbol{Z}_{AA'} + \boldsymbol{Z}_{mm}}. \tag{2.9}$$

With the knowledge of reflection coefficient, the power transmission coefficient $\boldsymbol{T}$ is easily calculated as

$$\boldsymbol{T} = 1 - |\boldsymbol{\Gamma}|^2. \tag{2.10}$$

The power transmission coefficient evaluates the amount of the incoming power penetrating into the body and is calculated using 3 different variables. Frequency in range $0.5 - 2.0$ GHz, relative permittivity of matching medium $1 - 80$ and the effective conductivity of the matching medium from 0 to 1.

Each layer of the medium (see transmission line model in Fig. 2.6) has been modelled with the properties of the tissues encountered (according to the Debye model) by propagating from the matching medium into the body. In building such a model, a peculiar aspect has to be considered, namely the fact that the bladder can be either filled with urine or empty. Notably, each of two states may be identified as a requirement with respect to treatment and monitoring. Accordingly, the power transmission coefficient has been appraised for both the cases of an empty bladder and a full bladder.

In [33], the last tissue in the model was brain, which is big in comparison to the other layers in the head and could be considered as infinite. In our case, the bladder wall is thin and that is why we are making big error considering it as infinitely extended. Due to this fact, not the bladder wall, but the bladder content was determined as a target. The 1D layered model, inspired by the shortest line between the surface and the bladder in the Zubal phantom cross section, looks accordingly: skin 2 mm, fat 12 mm, muscle 12 mm, fat 16 mm, bladder 20 mm. The bladder wall thickness doesn't correspond to the average value 3.35 mm [35] because the horizontal cut being located in the upper part of the bladder. For general analysis the thickness of the tissues was rounded to whole millimetres: skin 2 mm, fat 12 mm, muscle 12 mm, fat 16 mm, bladder 3 mm and urine as a last tissue in case of full

bladder. When considering the empty bladder case, only 4 layers were used in the equivalent transmission line model, remaining bladder as a target, and muscle tissue was increased to 16 mm.

The analysis is not optimal, because the calculations assume, that electrical conductivity of matching liquid remains constant through all frequencies. As long as an existing prototype of a regional hyperthermia system [24] uses a bolus of deionized water with a temperature between 18 and 20 °C, the matching medium we consider for imaging must have the properties of the deionized water. Using a static conductivity value, which is very low ($\sigma_{static} = 5,5 \cdot 10^{-6}$) [36], is true when very low working frequency is applied. However, in case of higher working frequency, the equivalent conductivity of water caused by rotational polarization of water molecules $\sigma_e = \sigma_i + \omega\epsilon''$ increases. The model of dielectric properties of water dependent on frequency and temperature was proposed by Ellison [37] and we used it for more realistic scenario. The 1D analysis was modified and the computation of the power transmission coefficient was only done for a deionized water whose permittivity and conductivity are changing according to the model from [37].

2.3 Numerical simulations

Numerical simulations are an useful engineering tool for investigating and predicting the evolution of the electromagnetic waves in specified space. There are many different mathematical methods and two of them were used in this work.

Method of Moments (MoM) is a technique used to solve differential or integral equations. The approximation lies in the substituting of the unknown function by a series of known functions with unknown expansion coefficients. The approximate equations are tested so that the weighted residual is zero. The resulting algebraic system of linear equations is solved for the unknown coefficients. [38]

MoM is a basic principle of solving the electromagnetic radiation and scattering problems and many methods can be derived from that. The difference lies only in using different expansion and weighting functions and in equation solution methods. [39]

The finite element method (FEM) makes a discretization of the original problem and aproximates it with a problem with a finite number of unknown parameters [40]. Division of the whole investigated body into system of smaller bodies or units interconnected at nodal

points or boundary lines allows to formulate the equation of each element and gain the solution by their combination instead of solving the whole problem in one operation, which is in case of complicated geometries and material properties impossible [41]. As a consequence, finite element excel at solving geometrically and materially complicated configurations.

Because of easy implementation of the anatomically realistic Zubal's phantom into the solver based on MoM, all of the 2D simulations were made using MoM whereas the simulations using real antenna and 3D phantom geometry ran in the commercial software COMSOL Multiphysics using FEM.

Similar to [1], a single-frequency multistatic multiview measurement configuration has been adopted considering all antennas working as both transmitters and receivers. The antennas were modelled as filamentary currents with unitary excitation. When i^{th} antenna is transmitting, all the other antennas are recording the induced field and the process iterates until all the antennas were active. In the end, not all the recordings are necessary thanks to reciprocity principle, although the reciprocal measurement can reduce noise. The number of iterations in the algorithm till it reaches the final accuracy 10^{-6} and therefore also the computation time depends on the wavelength of the electromagnetic radiation in the medium, which is defined accordingly:

$$\lambda = \frac{c}{f\sqrt{\varepsilon_b}}, \tag{2.11}$$

where c is the speed of light in a free space, f is the frequency of the incident field and ε_b is the relative permittivity of the matching medium (background). In case of fixed geometrical dimensions, the bigger the wavelength is, the smaller number of iterations is needed for a reliable result.

As an input for the forward solver, the contrast function $\boldsymbol{\chi}$ is needed. This function is calculated with knowledge of the complex relative permittivity distribution map ($\boldsymbol{\varepsilon_x}$) and the complex relative permittivity of matching medium ($\boldsymbol{\varepsilon_b}$).

$$\boldsymbol{\chi} = \frac{\boldsymbol{\varepsilon_x}}{\boldsymbol{\varepsilon_b}} - 1 \tag{2.12}$$

This contrast function must be specified for the frequency and for the permittivity of matching medium which is used in the scenario.

Taking into account that the bladder is the main organ of interest, the antennas should be placed as close to it as possible, which means frontally to the body. A simple set up was used to compare the simulation with full and empty bladder and so to support the results of

the 1D analysis. Considering the adopted 19 °C water bolus as a design constraint (as this medium also plays a role as thermo-stabilizer), temperature dependent pelvic region model was set to 37 °C of all tissues and 10 antennas in a line radiated with 800 MHz frequency acting as both receivers and transmitters were simulated for both cases - full and empty bladder. The results are displayed in form of induced current density J normalized with respect to its maximum

$$J \propto \left| \sum_{n=1}^{N} \boldsymbol{E_{tot,n}} \cdot \boldsymbol{\sigma_x} \right|, \tag{2.13}$$

where $\boldsymbol{E_{tot,n}}$ is the n^{th} component of total field and N is number of antenna measurements.

The same results validation was done in case of searching proper working frequency. The tissue properties were set to 37 °C and the bladder was considered empty in order to work under consistent conditions. Again, 10 antennas and water bolus (19 °C) were used. The normalized induced current density was calculated using 0.6, 0.8, 1.0 and 1.2 GHz.

Scattering matrix ($\mathbf{S}$) is an important output from an electromagnetic simulation because it provides a description behaviour in the antenna network. $\mathbf{S}$ enables to determine the output of all ports, when their input is known, in other words, it describes the transmission between individual ports. The diagonal values represent reflection coefficients (quantities used to determine the amount of the incident signal reflected back into the originating port) and the other values represent transmission coefficients (quantities used to determine the amount of the incident signal transmitted from the transmitting antenna port into the receiving antenna ports). [42]

As long as the differences in dielectric properties of human tissues due to applied hyperthermia are low, the question arises if the existing measuring devices are able to detect these changes. Since hyperthermia is a planned treatment, it is possible to measure the $\mathbf{S}$ at the normal state (before the treatment) and also in the hyperthermia state (during the treatment) and therefore use differential data. 4 different numerical simulations were made for specific frequency - temperature of the bladder wall tissue was set to 37, 42, 45 and 50 °C . The physiological temperature, two levels of common hyperthermia value and one slightly higher which can occur accidentally. In order to find compare the resulting dynamic ranges (DR), following approach was used

$$DR = 20 \cdot \log_{10} \left| \frac{\mathbf{S}_{\vartheta_2} - \mathbf{S}_{\vartheta_1}}{\mathbf{S}_{\vartheta_1}} \right|. \tag{2.14}$$

Another approach to evaluate the DR of measurement was inspired by [43]. The Frobenius norm, defined for matrix A as [44]

$$\|\mathrm{A}\|_{\mathrm{F}} = \left(\sum_{i=1}^{m} \sum_{j=1}^{n} a_{ij}^2 \right)^{1/2}, \tag{2.15}$$

was used as follows. Norm of $\mathbf{S}_{\vartheta_1}$ at 37 °C and $\Delta\mathbf{S}_{\vartheta_1\vartheta_2}$ between different temperatures have been normalized to the Frobenius norm of the data matrix of the total measured field ($\mathbf{E}_{ta}$) corresponding to sum of the field scattered by the body ($\mathbf{S}_{\vartheta_1}$) and the direct field from transmitters to receivers ($\mathbf{E}_{ia}$)

$$\begin{aligned} DR =& 20 \cdot \log_{10} \left(\frac{\|\mathbf{S}_{\vartheta_1}\|_{\mathrm{F}}}{\|\mathbf{E}_{ta}\|_{\mathrm{F}}} \right) \\ DR =& 20 \cdot \log_{10} \left(\frac{\|\Delta\mathbf{S}_{\vartheta_1\vartheta_2}\|_{\mathrm{F}}}{\|\mathbf{E}_{ta}\|_{\mathrm{F}}} \right) \\ \mathbf{E}_{ta} =& \mathbf{S}_{\vartheta_1} + \mathbf{E}_{ia} \end{aligned} \tag{2.16}$$

The question may arise if the linear antenna arrangement is preferable or the antenna elements should rather be placed in such a way to conform to the shape of the body while being each one at the same distance from it. This new arrangement with antennas shifted so that they were always 3 cm from the skin was tested at 1 GHz frequency.

2.3.1 Hot spot detection

In hyperthermia, we are not only interested in seeing how the target tissue is heated, but also if some unwanted hot spots occur. These hot spots are dangerous and painful for the patients and must be avoided in a succesfull treatment. Hot spots mainly occur at tissue interfaces due to large variations in tissue dielectric properties and due to insufficient blood perfusion [3]. The variations in tissue properties cause power absorption and a slow blood perfusion is not able to remove the heat from the tissue which leads to temperature increase [3]. The location of the hot spots may differ from the hyperthermia target's location that is why the whole body should be controlled by the antennas and not only the portion facing the antennas. An antenna holder with a water bolus for regional hyperthermia prototype was designed and created in the Czech Technical University [24] together with a phantom of pelvic region [25]. The simplified geometry of the antenna holder is shown in Fig. 2.7.

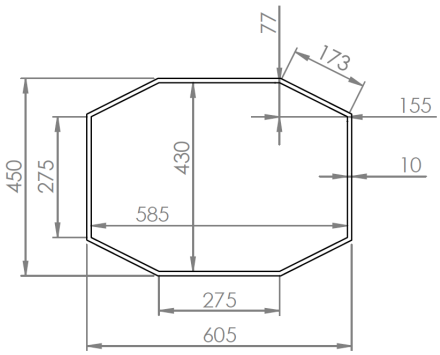

Figure 2.7: Symplified geometry of an antenna holder for regional hyperthermia system [24], front view, dimensions in mm

The maximum number of available transmitting and receiving channels is 24 with 3 antennas placed on each side of the octagon (Fig. 2.8) operated at the working frequency of 1 GHz. The simulations were performed for various scenarios, when the bladder temperature ranges from 37 to 50 °C with a step of 1 °C while the temperature of other tissues remains physiologic. The results of the simulations were first evaluated in form of a normalized induced current density in the phantom, in form of normalized differential scattering matrices and in form of Frobenius norm analysis.

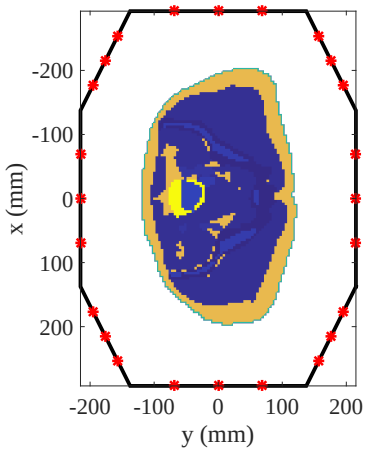

Figure 2.8: 24 antennas configuration (red stars) around the pelvic region phantom located on an antenna holder (black octagon) [24] .

With the goal to get the information about the sensitivity of the system, hot spots were introduced in the numerical phantom. The hot spot was modelled as a circular region defined by x and y coordinates of center, radius and temperature. In this region, the complex

permittivity of tissue was changed (if the tissue was modelled as temperature dependent). In a different way than before, the skin was modelled as temperature dependent thereby the malfunction of cooling water bolus was considered also. 5 scenarios differed in temperature of bladder and the hotspot and in location and size of the hotspot. To have a better overview the characteristics are shown in Table 2.2. Once, the hot spot was modelled at the tissue interface where usually occurs and at the same time close to the bladder imitating the situation that the hyperthermia treatment planning missed the target. The challenging problem in this case lies in the different temperature dependence of different tissues. For example muscle changes its properties extensively in comparison to fat and the contrast in fat tissue is then harder to detect. Another scenarios model the situation when the bladder is heated and simultaneously different temperature hot spots occur. In the end, the ability of detecting a very small radius of hot spot was tested.

Table 2.2: Properties of scenarios differing in temperature of a bladder and hot spot and location and radius of a hotspot.

scenario	$\vartheta_{bladder}$(°C)	$\vartheta_{hotspot}$(°C)	centerX(m)	centerY(m)	radius (m)
a	37	50	-0.11	0	0.02
b	37	50	0.05	0.1	0.02
c	42	50	0.05	0.1	0.02
d	42	42	0.05	0.1	0.02
e	42	50	0.08	0.1	0.005

2.3.2 Variability in tissue properties

In reality, the tissue properties are not homogeneous because of many factors. That is why the complex permittivity of each pixel in the target (not in the background medium) was randomly decreased or increased in the range between -5 % and $+5$ %. By contrast, the heating dependence of the tissue remained the same because we assume, that this variability doesn't change at the certain patient. Again, different scenarios were simulated using 24 antennas on an octagon with 1 GHz working frequency:

- scenario f: bladder 42 °C , no hot spot
- scenario g: bladder 42 °C , hot spot 42 °C

2.4 Imaging

When a non-homogenous matter is exposed to the incident electromagnetic field, electromagnetic scattering phenomenon occurs. This means that the incident wave is scattered and a total field can be described as a sum of the original incident field and the scattered one. The direct scattering problem tries to determine the scattered field when the incident field and the properties of the scatterer are known. On the contrary, the goal of the inverse problem is to find physical reconstruction of the scatterer with the help of incident and scattered wave at large distances of the scatterer. One of the mathematical problems one must face is ill-possedness which creates an artificial oscillation of the solution. That's why an incorporation of the regularization at some step of the implementation is necessary. [45]

Difficulties of the inverse scattering problems in case of imaging of big regions of biological tissues are following. The scattered fields can be only measured in the limited space, not inside the object domain. When modelling electromagnetic wave propagation in the range of microwaves, one must consider the diffraction effects. Due to the big wavelength, which is only a few times smaller than the object, the wave can't be simplified to a ray. Lastly, the contribution of the inner body structures is easily masked due to the high contrast of the external layers and the ambient environment. [23]

As far as the image algorithm is concerned, the initial goal in this thesis is to verify the possibility of qualitatively imaging the variations induced by the EM energy deposition in the target region. Based on this assumption and noticing that the relative changes in complex permittivity with temperature do not correspond to a large contrast (in terms of the relative variation with respect to the baseline given by the initial value), the scattering phenomenon has been modeled with the distorted Born approximation (DBA) and the resulting linear ill-posed inverse problem has been solved in a stable way by using the truncated singular value decomposition (TSVD), similarly to what is done in [1].

The different time instants in our case are specified by the modified temperature. For reader's convenience, the mathematical background according to [1] is described in the following lines. Stating that array of P antennas is located on a surface D, the time-harmonic scattered field measured at one time instant by the receivers located in $\mathbf{r}_p \in D$ when the probe in $\mathbf{r}_q \in D$ is radiating can be expressed as

$$\mathbf{E}_s^n(\mathbf{r}_p, \mathbf{r}_q) = \int_\Omega \mathbf{G}_e(\mathbf{r}_p, \mathbf{r}) \cdot \mathbf{E}^n(\mathbf{r}, \mathbf{r}_q)\boldsymbol{\chi}^n(\mathbf{r})dr, \tag{2.17}$$

where Ω represents the investigated domain, $\mathbf{G}_e$ the Green's function for the reference scenario, $\mathbf{E}^n(\mathbf{r}, \mathbf{r}_q)$ is the total field (sum of incident and scattered field) at one time instant and $\boldsymbol{\chi}^n(\mathbf{r})$ is the function of electric contrast: map of electric properties according to the geometry and material of the imaging scenario with respect to the properties of background medium.

The location of heated region where temperature variation occurs between the two time instants (before and during or after application of hyperthermia treatment) can be expressed thanks to Maxwell's equation linearity using differential field $\Delta\mathbf{E}_s$

$$\Delta\mathbf{E}_s(\mathbf{r}_p, \mathbf{r}_q) = \int_\Omega (\mathbf{G}_e(\mathbf{r}_p, \mathbf{r}) \cdot \mathbf{E}^1(\mathbf{r}, \mathbf{r}_q)\boldsymbol{\chi}^1(\mathbf{r}) - \mathbf{G}_e(\mathbf{r}_p, \mathbf{r}) \cdot \mathbf{E}^0(\mathbf{r}, \mathbf{r}_q)\boldsymbol{\chi}^0(\mathbf{r}))dr. \tag{2.18}$$

The Green's function in both temperature instants remains the same but the total field alters as long as it is dependent on contrast. Without some approximation, the Eq. 2.18 can't be simplified, but since the variation between the two contrast functions is very weak in values and also small in size, the total field after the hyperthermia can be considered unchanged. This approach corresponds to the distorted Born approximation and therefore the equation can be rewritten as follows and the integral can be substitute by a linear operator $\mathbf{L}_e$

$$\begin{aligned} \Delta\mathbf{E}_s(\mathbf{r}_p, \mathbf{r}_q) &= \int_\Omega \mathbf{G}_e(\mathbf{r}_p, \mathbf{r}) \cdot \mathbf{E}^0(\mathbf{r}, \mathbf{r}_q)\delta\boldsymbol{\chi}(\mathbf{r})dr \\ &= \mathbf{L}_e\delta\boldsymbol{\chi}. \end{aligned} \tag{2.19}$$

The resulting inverse problem is linear and ill-posed which requires an adoption of suitable regularization tool. Since the monitored temperature changes quickly in time, fast and simple methods are necessary to be used for getting a fast response - in the best case a real time monitoring. TSVD scheme is a suitable tool meeting the requirements and the differential contrast can be retrieved from an inversion formula:

$$\delta\boldsymbol{\chi} = \sum_{n=1}^{N} \frac{1}{\sigma_n}\langle\Delta\mathbf{E}_s, \mathrm{U}_n\rangle\mathrm{V}_n, \tag{2.20}$$

where σ_n, U_n and V_n denote the singular values and the left and right singular vectors of the linear operator $\mathbf{L}_e$. The truncation index N is a regularization parameter and its value can

be chosen according to the singular values spectrum (location of a change in slope). If this is an optimal truncation index setting, still remains an open question. In this thesis, more levels of the index was tested and after that the optimal index was chosen for the specific problem.

A slight modification of the linear operator by multiplying it by squared wave number and surface area of one pixel provides a quantitatively more accurate result of the final image, because it comes from the correct scattering equations. The solution of the TSVD can be usually overestimated in case of some pixels, especially, when focusing on a small region in the searching domain. However, the integral over the retrieved image should be very close to the integral of the actual contrast. (personal communication with Rosa Scapaticci, Ph. D.)

The imaging algorithm based on a DBA and TSVD was first tested on data obtained from forward simulations with 10 antennas placed in a line operated at their working frequency 1 GHz. As the initial scenario the pelvic region with tissue properties at 37 °C was considered and the change was imaged with respect to the same scenario but with the bladder properties at 42; 45 and 50 °C separately. The bladder was always considered empty. White Gaussian noise was added to each of the simulated scattering matrices with the implemented MATLAB function awgn. This function computes the signal level of the input matrix first and with respect to this level generates white Gaussian noise (different value for each element in matrix) with set level of SNR (in this thesis mainly 80 dB), while starting at the random number - seed. Afterwards, this noise is added to the input matrix. Because the matrices are subtracted later and same noise would be lost, it is necessary to specify different seeds at both matrices. Next, monostatic part of the matrices was set to 0, giving bigger significance to the transmitting coefficients with an order lower signal value. The truncation index in the TSVD was set taking the index corresponding to a -40 dB threshold for the normalized singular values.

As a next step, similar imaging process was applied to data gained from numerical simulations with 24 antennas on an octagon, described in subsection 2.3.1. Aiming to evaluate the dependence of temperature change on the imaged results, 13 levels of temperature increase were imaged in a single plot. Only one horizontal line of each result was displayed and distinguished from the others by the color. Next, the minimal values of the retrieved differential contrasts were compared with the actual differential contrast for each temperature change.

The main reason, why the 24 antennas scenario has been implemented, was the need of examination the whole body due to the risk of hot spots occurrence. Data from scenarios simulating the hot spots (described in Table 2.2) have been used for imaging while they have been deteriorated by a noise (SNR = 80 dB) and truncation index corresponding to a -40 dB threshold for the normalized singular values was used.

Afterwards, the same imaging setting was used for retrieving a differential contrast from simulations with variability in tissue properties as described in section 2.3.2.

When a hyperthermia target is clearly defined, it is possible to focus just to this region in the imaging process. The only necessary step is to choose from simulated total fields the values situated in this region, in our case, the bladder region. This approach was applied on data with 24 antenna configuration deteriorated by a noise (SNR = 80 dB) using singular value threshold corresponding to -30 dB. Area of the target was simply specified as a square from -38 to 40 mm in x-direction and from -88 to -10 mm in y-direction.

From the analysis of numerical simulations in the former section follows that more levels of frequency are possible to use for measurement which leads to an opportunity to perform multi-frequency imaging. The modification of the algorithm was implemented and used on data simulated by 0.8, 1.0 and 1.2 GHz, 24 antennas on octagon configuration and bladder heated to 42 °C . The modification consists in adding another dimension to the linear operator and $\mathbf{S}$. The monostatic part of the scattering matrices and of the linear operator was set to 0, noise added to the $\mathbf{S}$ corresponded to SNR = 80 dB and threshold chosen for the truncation index was -40 dB.

An important question about the measurement is how many antennas are necessary to gain the satisfying result. To answer this question without doing more simulations it is possible to take just some part of the data we already simulated and reconstruct the image like that. The data used for this analysis corresponds to 24 antennas on an octagon configuration and 1 GHz frequency. The bladder was heated to 42 °C and the dielectric properties of the tissues were considered homogeneous. Imaging capability using 16 and 12 antennas with different distributions were tested while the antenna positions remained the most symmetrical as possible maintaining the ability to monitor the hot spot occurring. For all the cases, 80 dB noise was added and truncation index used corresponded to -40 dB of normalized singular values.

2.5 Images evaluation

An easy evaluation of the resulting images can be done by subjective decision if there is a location of significantly higher contrast than in the rest of the imaging domain. When choosing the optimal threshold for truncation index, different values were tested and the result with the subjectively highest contrast was searched. Afterwards, for more objective comparison of the results with the actual contrast, following methods have been chosen.

In order to objectively retrieve the qualitative information of the result (where is the temperature change located), the absolute value of the computed contrast was normalized first - input image $a(m,n)$. After that, a simple thresholding was used for segmentation of the image to hyperthermia target (1) and background (0) - output binary image $b(m,n)$. For each pixel (m,n) [46]

$$b(m,n) = \begin{cases} 1 & \text{for} \quad a(m,n) \geq \text{Threshold}, \\ 0 & \text{for} \quad a(m,n) < \text{Threshold}. \end{cases} \tag{2.21}$$

Threshold was chosen as a level of dB with respect to the maximum of the image. The Eg. 2.21 was implemented by using a MATLAB function im2bw, which requires as inputs an image and threshold in the range between 0 and 1.

In some cases, pixels of the target have the same level as artefacts of a small area. Expecting that the hyperthermia can't be so narrowly situated, these spots are removed from the image by morphological opening, while the shape and size of the removed artefacts can be controlled by a structuring element. In this case, disk shaped element with variation in radius was used.

When the target was defined, the sensitivity, specificity and accuracy of the method was evaluated taking into consideration true or false classification of every single pixel in the retrieved image as target or not, with respect to the actual contrast,

$$\begin{aligned} sensitivity &= \frac{TP}{TP+FN} \\ specificity &= \frac{TN}{TN+FP} \\ accuracy &= \frac{TN+TP}{TN+TP+FN+FP} \end{aligned} \tag{2.22}$$

where TP, FP, TN and FN correspond to true and false positive and true and false negative decisions respectively. Sensitivity is the proportion of true positives that are correctly identified by a diagnostic method. It shows how good the method is at detecting a hyperthermic location. Specificity is the proportion of the true negatives correctly identified by a diagnostic method. It suggests how good the method is at identifying normal (negative) condition. Accuracy is the proportion of true results, either true positive or true negative, in the whole imaging domain. In other words, it measures the degree of veracity of a diagnostic method on a condition. [47]

While this method tends to give results which are de-localized, many FP and FN pixels may occur, although the reliable shape is retrieved. (personal communication with Rosa Scapaticci, Ph. D.) Therefore another parameters were evaluated: areal ratio, describing the area classified as target with respect to the area of actual target, and localization error, describing the distance between the center of gravity of the retrieved and actual target. In this case, quantitative retrieved contrast is used while only pixels of the target are taken into consideration.

In order to evaluate the quantitative information about the temperature, integral over the values in the region of target was compared with an integral of the actual contrast.

Similar to [1], normalized root mean square error (NRMSE) was calculated for every retrieved image section including the bladder (x-coordinates in range from -0.088 to -0.010 m and y-coordinates in range from -0.038 to 0.040 m). The root mean square error (RMSE) defined as [48]

$$RMSE = \sqrt{\frac{\sum_{i=1}^{I}\sum_{j=1}^{J}[\delta\chi_{actual}(i,j) - \delta\chi_{retrieved}(i,j)]^2}{I \cdot J}} \tag{2.23}$$

where I and J correspond to number of x and y-coordinates, respectively, was normalized by the range of the retrieved signal ($\delta\chi_{actual_{max}} - \delta\chi_{actual_{min}}$) in order to be comparable between different scenarios. This value gives the information about a normalized distance of the retrieved matrix from the actual.

An important step in the evaluation is choosing an optimal threshold in assigning into the target or not target group. A threshold used the most frequently is -3 dB. (personal communication with Rosa Scapaticci, Ph. D.) When searching for a target, lower threshold could be chosen and still no or just few artefacts would have the same level. Therefore also threshold -6 dB was tested.

All of this classifications were applied to the scenarios simulating heating of the bladder in the range from 38 °C to 50 °C , when 24 antennas at frequency 1 GHz were radiated. Partial results showing an example of evaluation are shown in Fig. 3.25, next numerical results which are relatively constant for all the 13 different cases are displayed in Table 3.2 in form of the mean ± standard deviation.

2.6 Experiment

2.6.1 Antenna element

Ultra-wide frequency band (UWB) bow-tie antenna was designed, fabricated and tested for microwave imaging of change of dielectric properties in liquid muscle tissue phantom [49]. Basic bow-tie geometry is very simple and broadband and a proper broadband balun ensures symmetrical feeding of the bow-tie dipole by transforming the unbalanced input of a coaxial connector to balanced output.

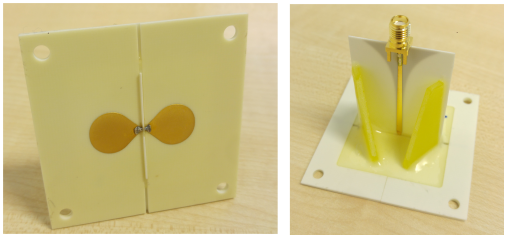

Figure 2.9: Fabricated UWB bow-tie antenna with tapered balun feed. [49]

The antenna was optimized for being attached directly to the muscle phantom and its behaviour when being attached to water bolus was unclear. Therefore, numerical simulations have been carried out mimicking the antenna radiation into water while S_{11} parameter (reflection coefficient) in dependence on frequency was measured (see Fig. 2.10). The coefficient reaches lower values than -10 dB at frequencies over 0.6 GHz which indicates, that the penetrated energy into the tissue is sufficiently high and thus the antenna applicable in our system.

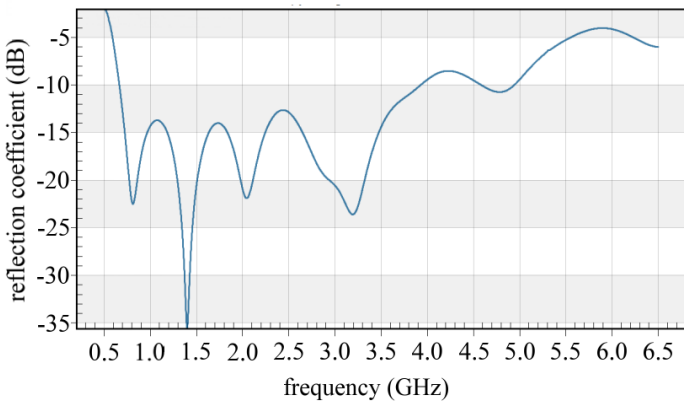

Figure 2.10: Absolute value of reflection coefficient with respect to frequency

2.6.2 Placing of the hyperthermia phantoms

When mimicking regional hyperthermia in pelvic region, we decided to focus on urinary bladder, cervix and rectum cancer.

The bladder grows with age and the size of female bladder (and so its capacity) is comparatively smaller than in males. The male bladder is located between the pubic symphysis and rectum while bladder in females lies anterior to the vagina and inferior to the uterus. [31]

The size of the tumor is very various and determines the stage of the disease. From a very small carcinoma can become a tumor invading prostate, uterus or vagina. [50]

The cervix lies between the urinary bladder anteriorly and the bowel (rectum) posteriorly and in physiological state, it is approximately 3 cm in diameter. However, the size changes for women having and not having offspring or with their reproductive age. [51] In staging system, the size of the cervical cancer can be less than 2 cm in I., 4 cm or more in II. and bigger in next stages when cancer has grown into the bladder or rectum or to far away organs like lungs or bones. [52]

Transversal CT scan of quite developed cervix cancer is shown in Fig. 2.11. As can be seen, rectum lies posteriorly to the cervix in females and to the prostate in males.

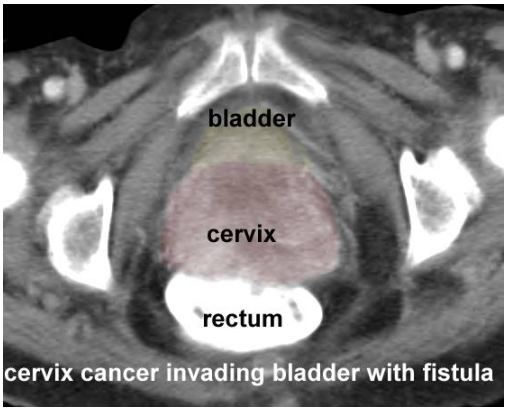

Figure 2.11: Transversal CT scan of cervix cancer with organs highlighted.[53]

In the real experiment, only liquid phantom with properties of muscle was used, but the size and location of the hyperthermia scenarios were considered according to real anatomy of organs mentioned in this section. The placing of the hyperthermia phantom in the center of the pelvic region phantom should symbolize the cervical tumour treatment, while its shifting 5 cm anteriorly should stand for the bladder or rectum cancer treatment. We decided to

simulate temperature change targets from 5 to 10 cm diameter corresponding to smaller and bigger tumour and more or less focused hyperthermia treatment.

2.6.3 Liquid muscle phantom

For the plastic container of phantom, the liquid with the same properties as muscle must be prepared. We decided not to heat the target phantom, because if we do it, the surrounding phantom of pelvic region will be heated as well. This, without a proper temperature in the whole pelvic phantom volume, would lead to changes in temperature during the measurement. Such a behaviour of each element in volume would be difficult to control and results of the measurements couldn't be evaluated with respect to the actual scenario. Moreover, preparation of a liquid which has the same temperature and frequency dependence as muscle is also not an easy task. Therefore, the temperature change was simulated only by modifying dielectric properties with the usage of known models [16].

According to [54], since different dielectric relaxation phenomena are dependent on tissue cell membrane as well as ionic properties, it is impossible to develop one phantom material to simulate tissue at all frequencies. Although the frequency range from 600 MHz to 1.0 GHz was determined possible for microwave imaging for this case, only one frequency could be chosen and the medium value from this range (800 MHz) has been considered as the most appropriate for searching for a right content of each ingredients for the phantom.

Similar to [49] destilled water, isopropyl alcohol (IPA) and NaCl were chosen as ingredients. The IPA decreeses, with its relative permittivity ca. $\epsilon_r = 20$, the permittivity of the mixture [55] while added NaCl causes the conductivity increase.

For initial estimation of ratio between water and IPA content, the measurement from [55] was used - a sample of 500 ml volume was mixed with 304 ml water and 196 ml IPA. The volume was measured by an 250 ml graduated cylinder and 5 ml automatic pipette. The exothermic reaction raised the temperature ca. from 23 °C to 29 °C and since the dielectric properties are highly dependent on temperature, the sample was cooled down to laboratory temperature. The important thing is, that the sample must be sealed during the cooling, because the IPA evaporates quickly which causes the permittivity increase.

The samples were measured by Dielectric Assessment Kit (DAK 4 MHz – 3 GHz) from SPEAG [56]. As the measured permittivity of the sample was lower than expected, the

water was added as long as it corresponded with the value of muscle at 37 °C . After that the conductivity was adjusted by adding NaCl.

When the right amounts of water and NaCl were found to model muscle at 37 °C , the IPA was added to decrease the permittivity and NaCl to increase the conductivity again and so model the temperature change. Small amounts of each ingredient were added and the samples were measured since the approximate values were gained.

The final recipe for preparing this phantom in terms of amounts is shown in Table 3.4 for all the chosen temperatures always for 800 MHz frequency.

When the content of the ingredients in all temperature cases was defined, a new samples of all temperatures were prepared based on the recipe in order to test the correctness of the measurement before. In each case, the sample was measured ten times so the type A uncertainty (u_A) could be calculated, while type B uncertainty (u_B) is determined by DAK device producer for a certain frequency range. Combined type C uncertainty (u_C) is calculated by Eq. 2.24.

$$u_C = \sqrt{u_A^2 + u_B^2} \tag{2.24}$$

2.6.4 Realization of the experiment

Firstly, the experiment was planned to be undertaken with the already existing antenna holder with water bolus [24] and the pelvic region phantom [25] (see Fig. 2.14). A container had to be chosen, which should mimic the local temperature increase. The material must have low permittivity and conductivity values, the shape should resemble the bladder or other hyperthermia target geometry, while the dimensions should be clearly defined and also available in some variations. Next, the container should be easily placed into the pelvic phantom with clearly defined coordinates. We decided not to consider 3D shape of the organs but only focus on its cross-section which led to a choice of cylindrical pipe. The drain pipes made from Polypropylene are available in every building supply store in various radii for a low prize. For the imaging analysis, 3 different diameters were chosen: 50, 75 and 100 mm, all of them in 50 cm length. For sealing off, plugs from both sides are used, but they can't be easily opened again when necessary and due to this fact, pipe cleaning fitting was incorporated which enables an easy access to the liquid. Lastly, an adapter for additional pipe connection is needed. Photographs of all of the parts are shown in Fig. 2.12.

(a) Drain pipe (b) Plug (c) Pipe fitting (d) Adapter

Figure 2.12: Parts of the temperature phantom container [57].

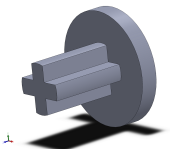

Figure 2.13: Geometry of a plastic pin facilitating phantom positioning.

The containers for liquid target phantoms were equipped with a pin (Fig. 2.13) in the middle of the pipe plug which should enable a precise positioning and stabilization of the phantom. These pins were modelled in Solidworks and printed out on the 3D printer (Prusa i3 mk2 MK3S, Prusa Research, Czech Republic) from PETG material having diameter of the circular plane 20 mm and of the cross shaped plane 9 mm.

The antenna holder with water bolus and pelvic region phantom (depicted in Fig. 2.14) are optimized for the horizontal position of the patient and they are not optimal for our experiment for following reasons. Firstly, the pelvic phantom has huge volume of ca. 108 l, which is very impractical for using liquid muscle phantom. In that case, approximately 43 l of IPA are required, which is expensive and due to its evaporation complicated to work with. Nevertheless, the preparation of the solution with specific properties is more complicated in a bigger volume. In the end, such a big amount of the liquid is not necessary because one half of the phantom volume is not used for measurement.

Second not convenient property of the phantom is, that there is only limited aperture for inserting phantom with different properties. On the one hand, we want the phantom to be as long as the hyperthermia system (50 cm), on the other hand, the phantom can not be too long making inserting inside impossible.

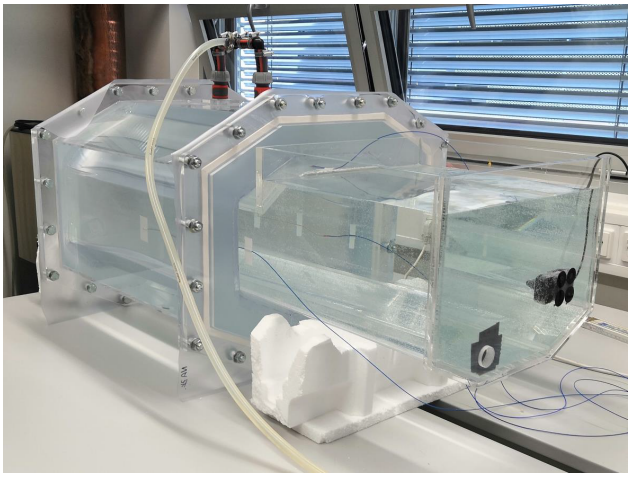

Figure 2.14: Antenna holder with water bolus and the pelvic region phantom filled with medium [25]

The idea how to decrease the necessary liquid phantom volume was to use the system vertically. In that case, only the space inside the antenna holder would be needed to be filled, but is not easy to change the position due to the water bolus. First, the existing inputs for water are located in the middle of the holder and in case of vertical position, only one half could be filled. This could be overcome by making another input in the upper part or using some tubule leading from the existing input up. The other option would be filling the bolus in the horizontal position and then turn it over, but taking into account, that the pelvic phantom must be already inserted inside and that the bolus volume is around 60 l, it would be very complicated to move this weight. Some mechanism would be required to make this possible.

Because of these limitations, the easiest solution seemed to be a creation of a new similar phantom and antenna holder optimized for the vertical case. This arrangement has been used successfully already [49].

One of the octagonal sides of the antenna holder was changed to be full plexiglass, creating the pedestal of the whole system and the flexible foil was removed because it is not needed in this configuration. In the bottom, a form was incorporated which facilitates the correct positioning of the pelvic region phantom in the middle of the antenna holder. The upper octagonal side remained opened to be easy filled with needed liquids. In the middle of the height, 24 square shaped holes were created being necessary for inserting antennas with balun and some mechanical support preventing the balun from breaking. Due to the antenna element size [49], it wasn't possible to incorporate the elements in the same way it was done in the 2D simulations (3 antennas on each side), so 4 of them were incorporated on the

longer side and 2 on the shorter one. In the corners of each hole, 4 small circular holes were designated for screwing antennas to the holder.

The phantom of the pelvic region was designed similarly. The orientation was changed to vertical, the upper part remained opened and the bottom turned into pedestal in which small holes were incorporated in the regular grid. They shall serve for precise positioning of a cylinder filled with liquid with different dielectric properties. A cover from a plexiglass was created in order to prevent the liquid muscle phantom to evaporate when letting it be unused for a longer time. We decided the pelvic region phantom not to be incorporated into the whole system for two reasons. First, the antenna holder will be more flexible to be used for other scenarios, second, the internal space will be better accessible for antennas incorporation. For creating the geometry of the whole system the programs COMSOL Multiphysics and Solidworks were used.

In order to complete the preparation for the experiment, individual pieces of antennas have to be manufactured by an external company, put together in a laboratory and their radiation characteristics have to be measured in the same way it was done in [49]. When all of the elements behave similarly, they must be incorporated into the antenna holder by screwing and the small holes between two parts of substrate (arisen due to the balun substrate insertion) must be sealed in order to prevent the water to leak. Later, the antenna ports have to be connected via semi-rigid coaxial cables to the switching matrix which is controlled by a vector network analyser. As long as the analyser have only 2 ports, the switching matrix enables to change its input and output port connection in all possible 24 antenna combinations without moving any cables.

When this is finished, liquid phantoms can be prepared and poured into the system and the experiment itself can start. Its protocol is described in the section 3.5.3.

2.7 3D simulations

The 3D numerical simulations should model the realistic experiment in order to predict the electromagnetic behaviour. All the components of the experimental set were modelled in the COMSOL Multiphysics before which also served as instructions for the phantom and holder manufacturing. The modelled antennas from [49] were incorporated into the antenna holder from inside in the way, that the substrate and the plexiglass wall were closely connected. The cylindric temperature-phantom was inserted into the model, neglecting the plastic material of the pipe which should not affect the scattering, and the geometry was finished by creation of the surrounding of the system in an octagonal shape which enabled the port-side of antennas to be outside of the computational domain. The complete geometry without the octagonal background is shown in Fig. 2.15.

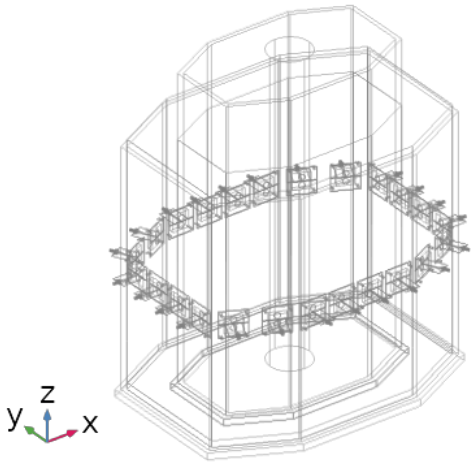

Figure 2.15: Final geometry of the 3D simulations.

The material properties were set accordingly. The antenna holder and container for water bolus and phantom are made from Poly(methylmethacrylat) i.e. plexiglass, which properties are stated in [58] and in [59]. Although, in the references the properties were not exactly determined for our frequency range, we chose a rounded value 2.6 for permittivity and 0.01 S/m for electric conductivity. Such a low value which is very different from the biological tissues should not affect the results and therefore its accuracy is not so important. Materials used on antennas were adopted from [49], substrate: $\epsilon_r = 3.65$, $\sigma = 0.0004$ S/m; teflon: $\epsilon_r = 2.1$, $\sigma = 0.0004$ S/m. Liquid phantom and water bolus were modelled with the use of MATLAB functions imported into the COMSOL Multiphysics with respect to

frequency and temperature according to the same models as in the 2D simulations. As a surrounding medium, properties of air were set. The outside boundaries of this surrounding medium were determined as scattering boundary conditions ensuring that there will be no unwanted reflections.

The mesh, which is necessary for FEM, was chosen to be tetrahedral and its size was set individually for each material. The rule was respected, that the maximum element edge size can be $\lambda/5$ [60] which is computed by the Eq. 2.11 with respect to the correct permittivity. This condition should guarantee, that the numerical solution will converge. However, the geometry of the antennas involves very small domains and edges, which are smaller than the minimal size of one element. In these cases, the minimal value was decreased.

Single-frequency multistatic multiview measurement was arranged by a parametric sweep where the changing parameter PortName switched from the first to the last one.

As a first scenario, 600 MHz frequency was used and 42 °C hyperthermia target was situated in the center of the octagon with its radius 50 mm, which should represent heated cervix. In the next scenario, the target was shifted to the side and so represent a bladder treatment when the heated area is big. In comparison, next scenario was similar, but the target's radius was set to one half − 25 mm.

Second tested frequency was 800 MHz and the scenario simulated small 42 °C bladder (shifted to the side with radius 25 mm).

Similar to the imaging in 2D, the monostatic part of the matrices and linear operator was set to 0, $\mathbf{S}$ were deteriorated by a noise (SNR = 80 dB) and truncation index was set to −50 dB according to the plot of normalized singular values. Only one horizontal slice in the middle of antennas was chosen and the linear operator was built by using summed intensity of electric field in all three dimensions. The multiplication factor of the linear operator was also modified - pixel area was substituted by a voxel volume. In the resulting contrast mainly on the edge of the phantom, few tiny artefacts occurred with a very high value, which masked the meaningful signal. Therefore, a moving average filter 5x5 was applied on the contrast through convolution in 2D (MATLAB function `conv2`). Properties of the retrieved image were evaluated as it is described in section 2.5.

Chapter 3

Results

3.1 1D analytical analysis

In order to find proper matching medium properties and suitable working frequency, the power transmission coefficient was calculated. The results obtained through this analysis, considering the matching medium conductivity of deionized water at 1 GHz ($\sigma = 0.27384 S/m$), are shown in Fig. 3.1.

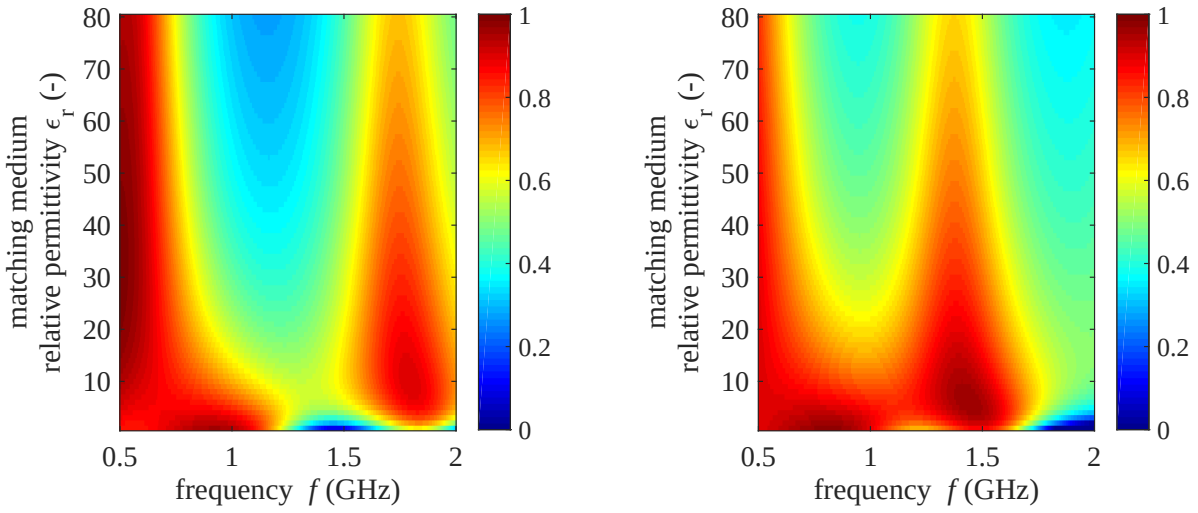

(a) Full bladder

(b) Empty bladder

Figure 3.1: Normalized power transmission coefficient with dependence on frequency and matching medium relative permittivity

As can be seen, the power transmission coefficient shows higher values in case of lower frequency for all permittivity values. The frequencies around 1 GHz would be more convenient with using low matching medium permittivity. The full bladder result shows bigger and faster coefficient decline for higher permittivity values than for the case of the empty bladder. For this case, the conditions of permittivity lower than 20 and frequency lower than 1.5 GHz should suit the best.

A better comparison of the two scenarios is shown in Fig. 3.2. The plot describes the dependence of the power transmission coefficient on the frequency for the only case of permittivity and conductivity, which corresponds to the actually adopted matching medium (i.e. deionized water bolus), which permittivity is change according to the frequency. One must take into account, that with increasing frequency the attenuation increases too. From this plot, it appears that lower frequencies seem more appropriate for this case at the cost of lower resolution. The scenario with an empty bladder doesn't show such a big decline and low minimum value as the full bladder case and although low frequency values of full bladder outperform the empty one, the empty one appears more suitable.

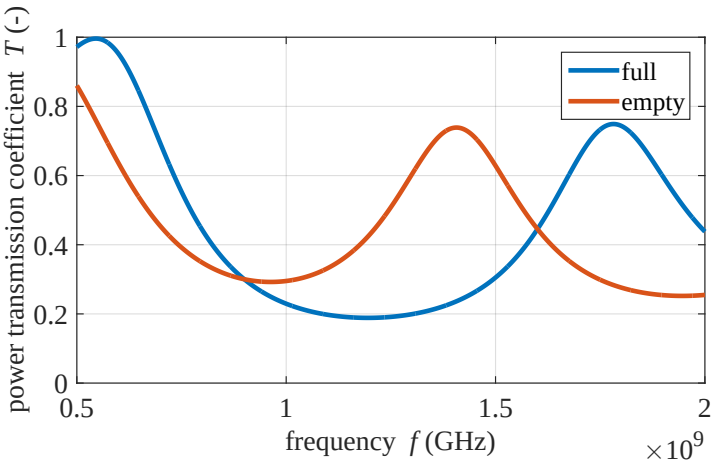

Figure 3.2: Normalized power transmission coefficient with dependence on frequency. Only for one matching medium - deionized water, temperature = 19 °C

3.2 Numerical simulations

A requirement with respect to treatment and monitoring was searched between the two states: full end empty bladder. A simple antenna configuration represented by a linear array with ten elements was used. The array is shown in the figures as red stars. The result of the simulation of 800 MHz (calculated according to the Eg. 2.13) are shown in Fig. 3.3. The lighter the color is, the more energy penetrates into the tissue and let the currents be induced. Both results are very similar, so it is not possible to decide, which condition is more suitable for temperature monitoring. Since the empty bladder is a clearly defined state, unlike the different possible volumes of full bladder, it is more convenient to ask the patient to empty its bladder before the treatment.

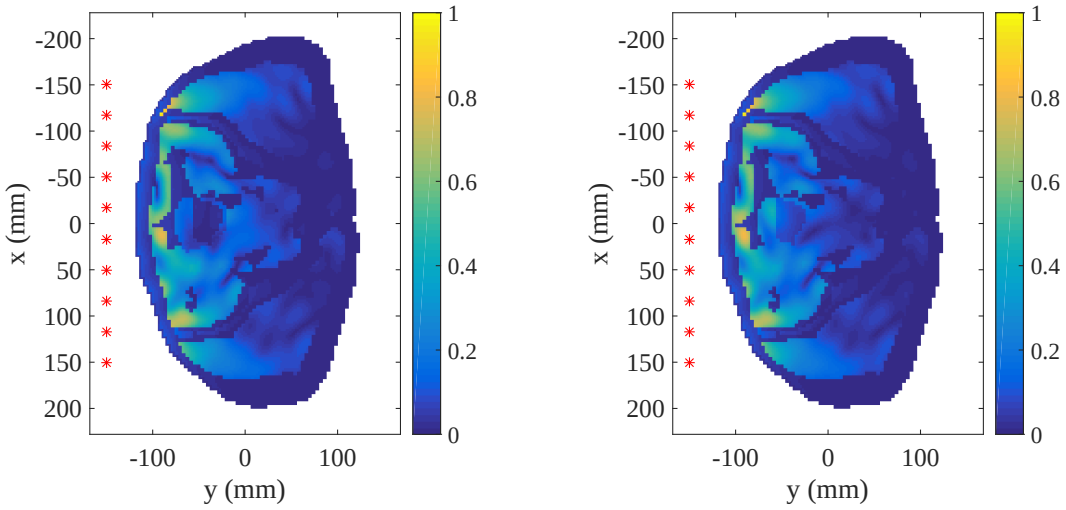

(a) Bladder filled with urine

(b) Empty bladder

Figure 3.3: Normalized induced current density for scenarios with full (left) and empty (right) bladder. 10 antennas in a line in the left side of the body were used. In this case, the dielectric properties are temperature dependent set to 37 °C . The deionized water was considered to have 19 °C . Working frequency: 800 MHz

Comparison of results in the form of normalized induced current density using frequency from 0.6 to 1.2 GHz are shown in Fig. 3.4. It can be noted, that with increasing frequency the attenuation increases too, as expected. This is not only due to the frequency itself, but also due to the increasing conductivity of the deionized water.

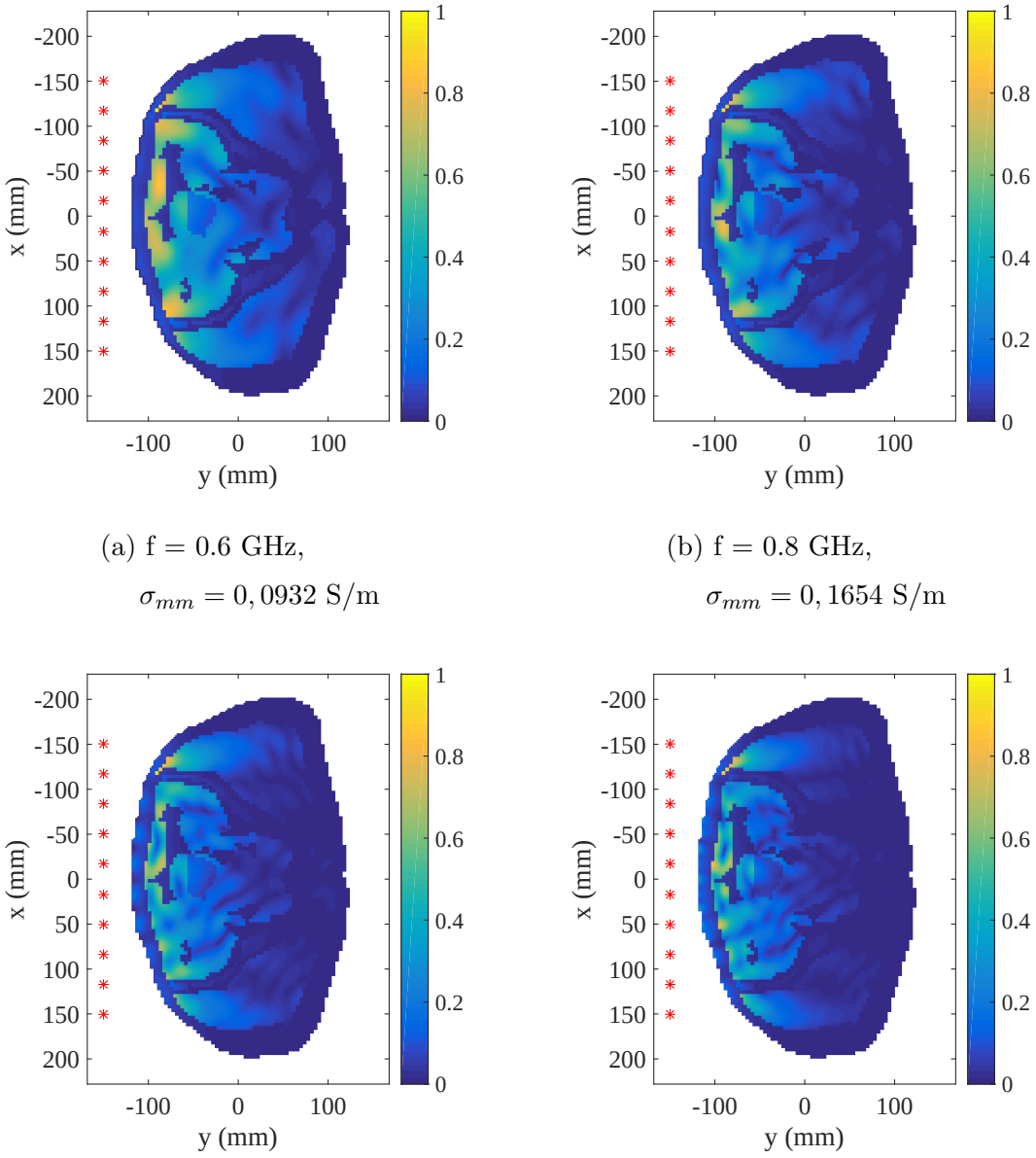

(a) f = 0.6 GHz, $\sigma_{mm} = 0,0932$ S/m

(b) f = 0.8 GHz, $\sigma_{mm} = 0,1654$ S/m

(c) f = 1.0 GHz, $\sigma_{mm} = 0,2581$ S/m

(d) f = 1.2 GHz, $\sigma_{mm} = 0,3710$ S/m

Figure 3.4: Induced current density for different frequency scenarios with use of 10 antennas in a line in the front side of the pelvis (red stars).

Scattering matrix of the 37 °C scenario is shown in Fig. 3.5 (amplitude and phase). Because the signal measured by the probes is lower than 1, the amplitude in dB shows how attenuated the received signal is in relation to the incident signal in the input. Signals close to the diagonal are less attenuated which validates the assumption that the reflected signals

have larger intensity. The longer the distance between antenna is (antennas number 1 and 10) the more attenuation occurs. The symmetrical distribution of matrix elements is in accordance with the principle of reciprocity $S_{ij} = S_{ji}$, i.e. that the transmission coefficient from antenna j to antenna i is identical with the transmission coefficient from antenna i to j.

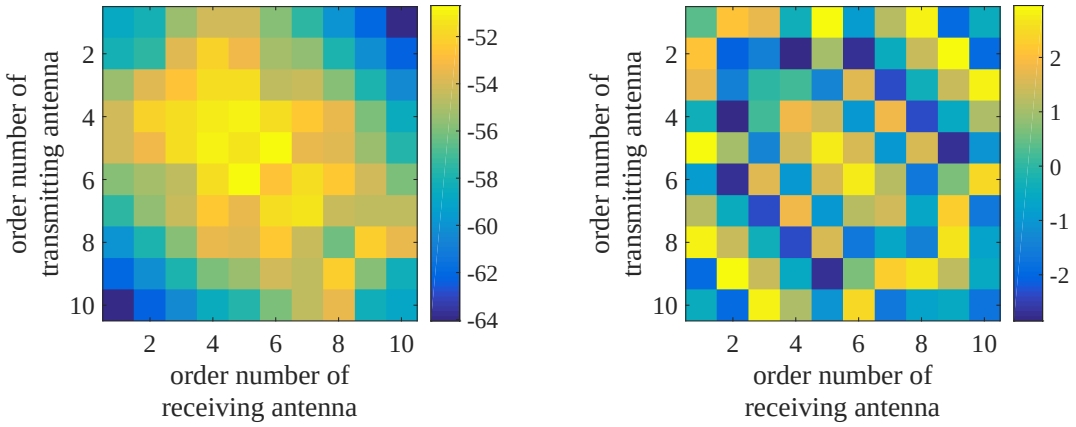

(a) Amplitude (dB) (b) Phase (-)

Figure 3.5: Scattering matrix. Working frequency: 800 MHz

Normalized $\Delta\mathbf{S}_{\vartheta_1\vartheta_2}$ in dB at different bladder temperatures are shown in Fig. 3.6 (calculated according to the Eq. 2.14). In the first one, the difference between physiological temperature and desirable hyperthermia temperature (42 °C) and in the second, the undesirable hot spot temperature (50 °C) are shown. Again, the value in dB demonstrates the level of attenuation, so the most noticeable areas are in the middle, mainly in region of 4^{th} - to 6^{th} antenna. It is important to point out, that although both matrices look very similar, their colorbar's ranges are different. This allows the reader to compare the maximal and minimal value in both cases. In the smaller difference case, we monitor the biggest value around -45 dB while in the second case around -40 dB. As expected, a bigger change in properties is registered better.

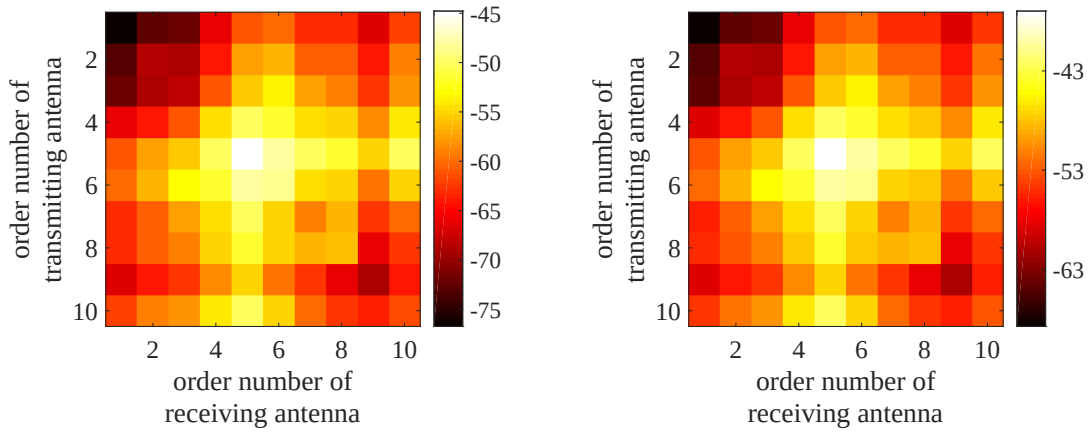

(a) 5 °C difference (b) 13 °C difference

Figure 3.6: Normalized scattering matrix differences in dB. In (a) 5 °C temperature difference is shown between temperature 42 and 37 °C and in (b) 13 °C difference between 50 and 37 °C . Working frequency: 800 MHz

The dynamic range calculated according to Eq. 2.16 of the measuring device in dB which is needed to detect the signal or signal difference at given frequency when the temperature is changed is shown in Figs. 3.7 and 3.8. It is computed from the scattering matrix at 37 °C in the first case and in the second from a difference between signal at 37 °C and at 42, 45 and 50 °C. In the not differential case, the values range from -6.8 to -7.8 dB and indicate, that the signal is easy to detect. On the other hand, it is comprehensible, that the differential case must appraise lower values hence bigger dynamic range. The values range from -50 to -65 dB giving smaller values for smaller temperature difference.

The existing microwave measurement devices have different dynamic ranges, but in the cases of more sophisticated and more expensive models the limit of the detection capability is -140 dB. The measuring device available in the CTU laboratory uses a switching matrix with maximum of 24 measuring ports while the coupling between individual ports can not be avoided. That is the reason why the real dynamic range is around -95 dB. (personal communication with Doc. Dr.-Ing. Jan Vrba, M-Sc., October 18, 2019)

According to results from the Frobenius norm analysis (Eq. 2.16), which show the lowest value around -65 dB, the differences between the different temperature scenarios should be detectable and available for using in imaging.

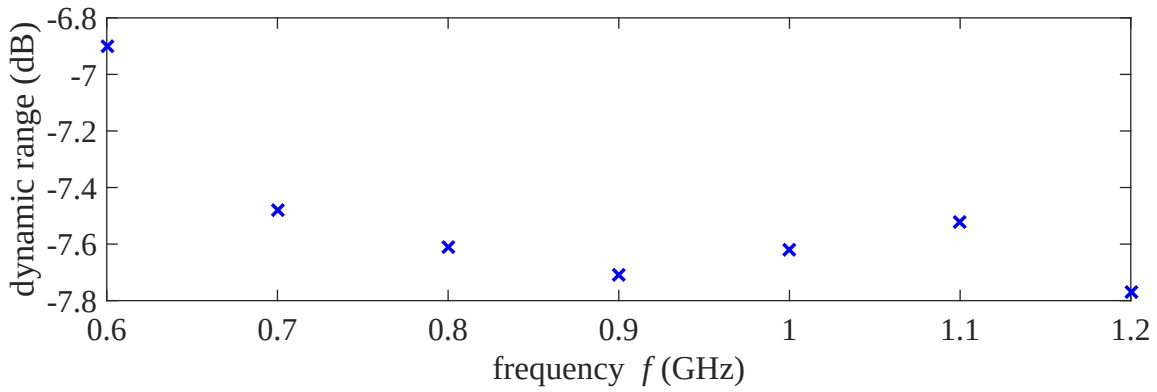

Figure 3.7: Normalized Frobenius norm of the scattering matrices at different frequencies at 37 °C .

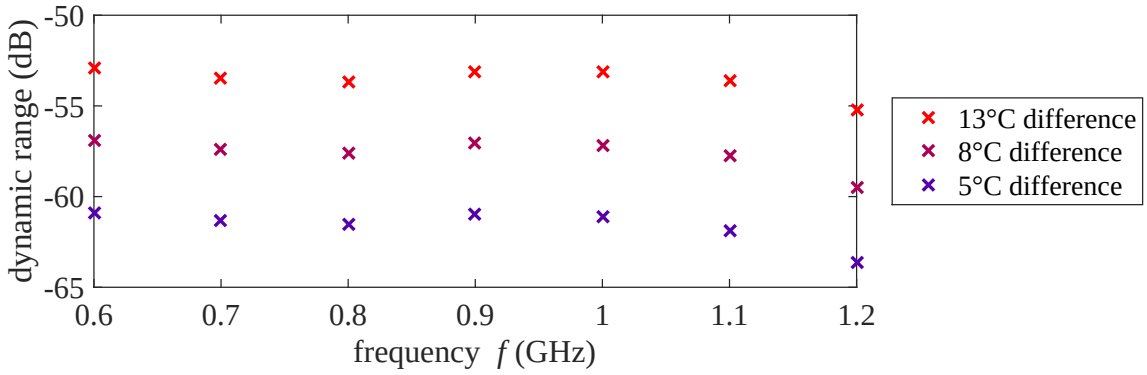

Figure 3.8: Normalized Frobenius norm of the differential scattering matrices at different frequencies at 40, 42 and 50 °C .

Fig. 3.9 allows to compare normalized induced current density in the phantom for two different antenna arrangements when 800 MHz radiation is applied. The antennas, highlighted as red stars, are positioned in a line or in a not symmetrical ellipse conformed to the shape of the phantom at a distance of 3 cm. Only slightly lower attenuation can be recognized from the figures indicating that the simpler arrangement is sufficient. Similar conclusions were gained by the Frobenius norm analysis displayed in Table 3.1. These values even indicate, that the ellipse arrangement is slightly worse, in other words a device with a bigger dynamic range is necessary for measurement.

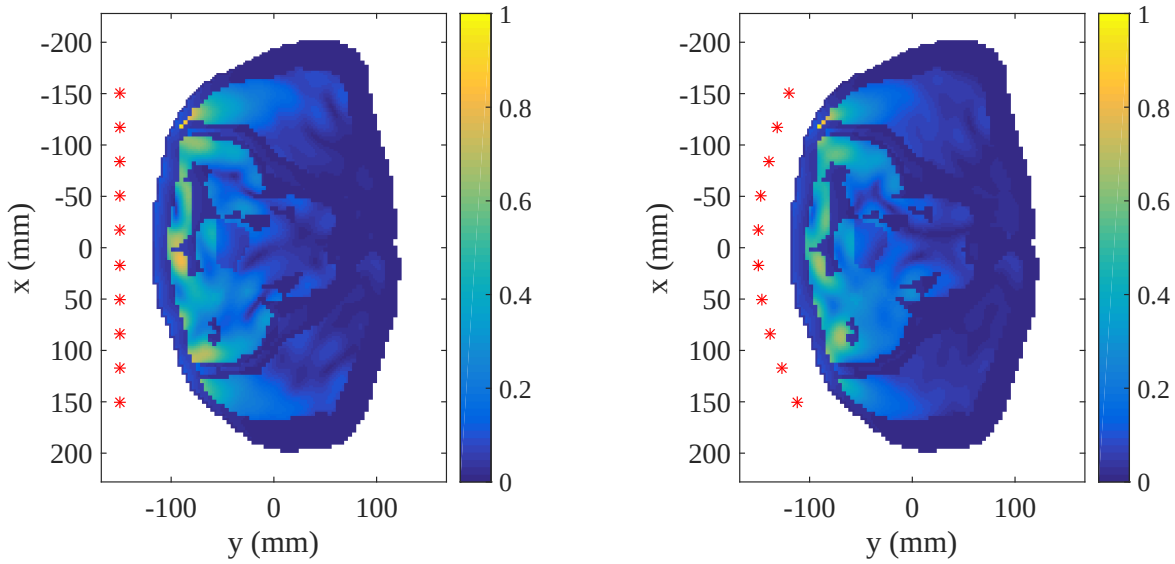

(a) in line

(b) 3 cm from the skin

Figure 3.9: Normalized induced current density for working frequency 800 MHz with use of 10 antennas in a line or in a ellipse in the front side of the pelvis (red stars).

Table 3.1: The dynamics of the measuring device in dB which is needed to detect the signal difference at given frequency (800 MHz) when the temperature is changed. It is computed from the difference between signal at 37 °C and at 42, 45 and 50 °C for different antenna configurations.

		Antenna arrangement	
		in line	ellipse
Temperature difference	5 °C	−61.13	−61.93
	8 °C	−57.16	−57.96
	13 °C	−53.15	−53.95

In Fig. 3.10, the induced current density describes the EM distribution in the tissue by the 24 antennas set-up. Due to the quite high frequency, the penetration is not optimal. However, the normalized differential S (Fig. 3.11) showed bigger signal level than −95 dB (minimum detectable with an existing device). The Frobenius norm analysis for scattering matrix at the temperature 37 °C and for difference in matrices between 37 and 42, 45 and 50 °C resulted in values −13.19 dB, −87.91 dB; −83.88 dB and −79.76 dB, which is close to the lowest detectable signal level, but still higher and therefore meaningful.

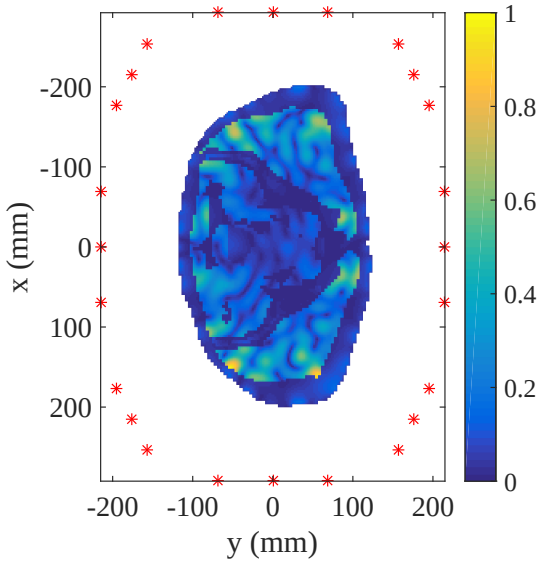

Figure 3.10: Normalized induced current density from all the 24 antennas around the phantom on the antenna holder. Working frequency: 1 GHz

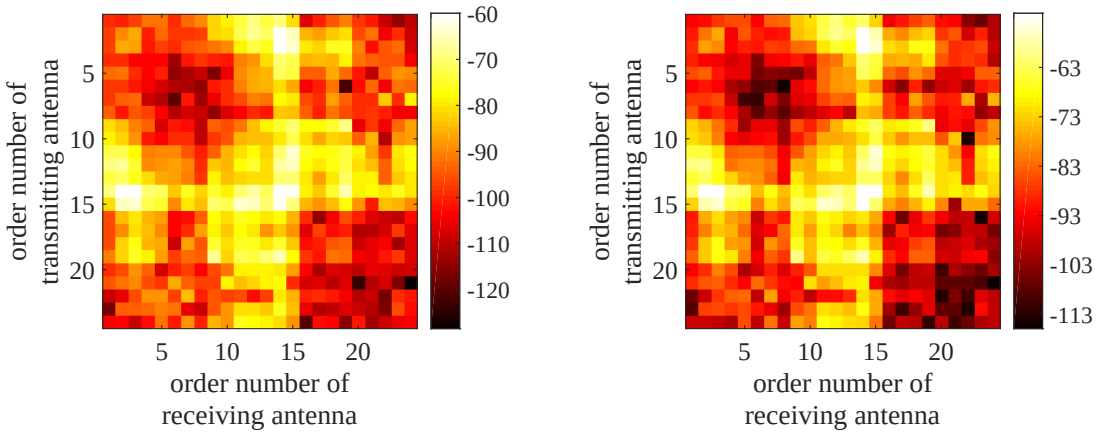

(a) 5 °C difference

(b) 13 °C difference

Figure 3.11: Normalized scattering matrix differences in dB. In (a) 5 °C temperature difference is shown between temperature 42 and 37 °C and in (b) 13 °C difference between 50 and 37 °C . Working frequency: 1 GHz

3.3 Imaging

The Fig. 3.12 shows the behaviour exhibited by the singular values of the linear operator L computed by distorted Born approximation obtained from forward simulations with 10 antennas placed on a line operated at their working frequency 1 GHz. Due to reciprocity principle only $\frac{N \cdot (N-1)}{2}$ singular values are displayed. In ideal case, the curve would firstly behave constant or slightly decrease and at some point fall steeply indicating that some values represent the most significant part of the spectrum thus the optimal threshold for TSVD selection would be easier. In Fig. 3.12, we observed some steeper intervals which seem convenient to help to choose the threshold. However, the drop around singular value index 18 corresponds to -10 dB which is too less and an important information would be lost. Threshold corresponding to level -40 dB was chosen to eliminate the effect of the noise.

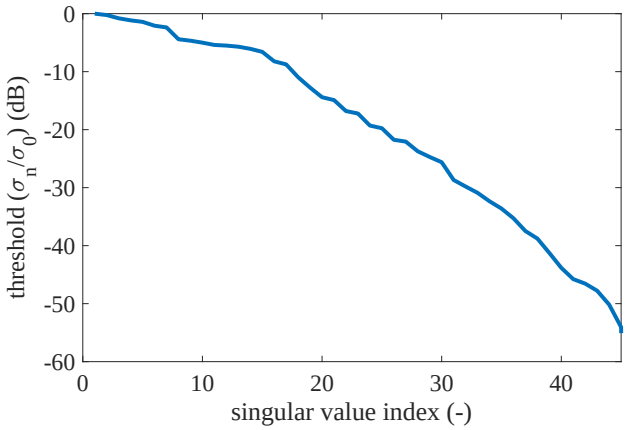

Figure 3.12: Normalized singular values, 10 antennas in a line

In Fig. 3.14 the real and imaginary parts of the actual differential contrast for the three scenarios (42, 45 and 50 °C) are depicted when working frequency 1 GHz was applied. The color scale shows the absolute differential contrast, while the values are negative in real and positive in imaginary part. As can be seen, the amplitude of the differential contrast increases with an increasing temperature change.

Next, Fig. 3.15 shows the corresponding retrieved contrast in case of 10 antenna elements in a line in front of the body. As long as the permittivity decrease in real and increase in imaginary part is the behaviour we expect, the opposite value artefacts were neglected and

set to 0. The results confirm that it is possible to image the location where the variation is occurring in all cases. Moreover, it can be appreciated that even if the actual values are not correct, the peak value of the reconstructed contrast increases (in amplitude) with the temperature increase, therefore providing a qualitative indicator of the ongoing treatment. Thanks to the artefacts appeared only in the front part of the body, it is noticeable that the signal didn't penetrate through all the tissues. In spite of this, the place of the heating is clearly determined being also similar to the actual shape in case of relative permittivity.

In Fig. 3.13, normalized singular values are shown computed from data obtained from forward simulations using 24 antennas on an octagon around the body. In Fig. 3.16, the retrieved differential contrast from the data is shown. Again, the location and shape of the target is clearly visible, very accurately in case of relative permittivity. The increasing behaviour of the amplitude with increasing temperature difference remains similar like in the previous cases.

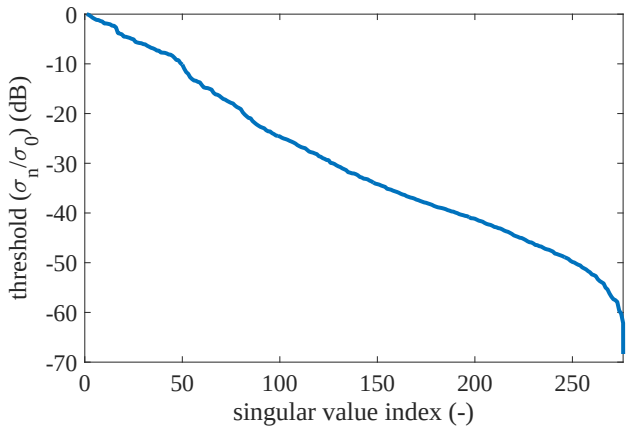

Figure 3.13: Normalized singular values, 24 antennas on octagon

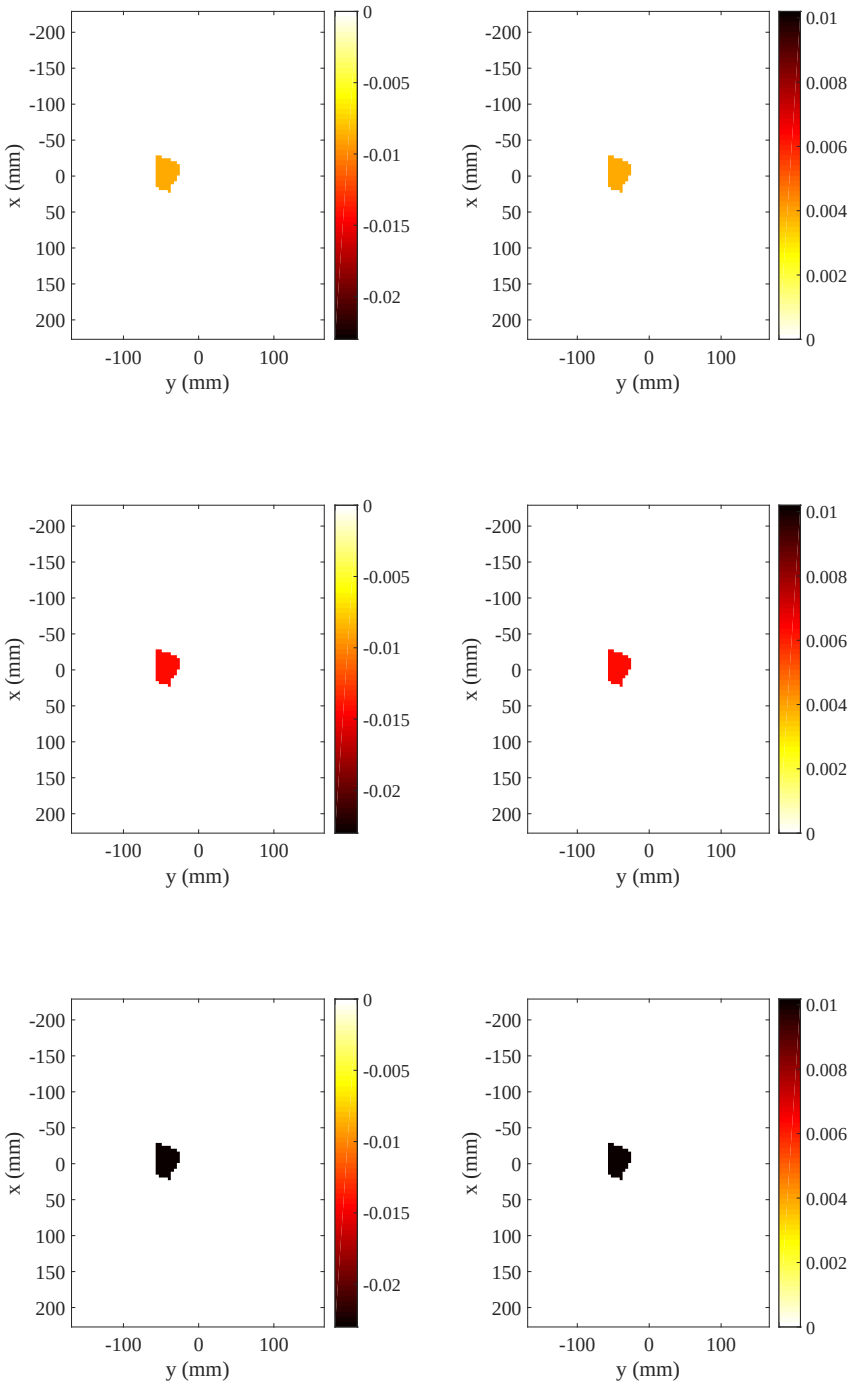

Figure 3.14: Real (left column) and imaginary (right column) part of the actual differential contrast starting from the body temperature of 37 °C for the three considered cases: (top row) $\vartheta = 42$ °C ; (middle row) $\vartheta = 45$ °C ; (bottom row) $\vartheta = 50$ °C .

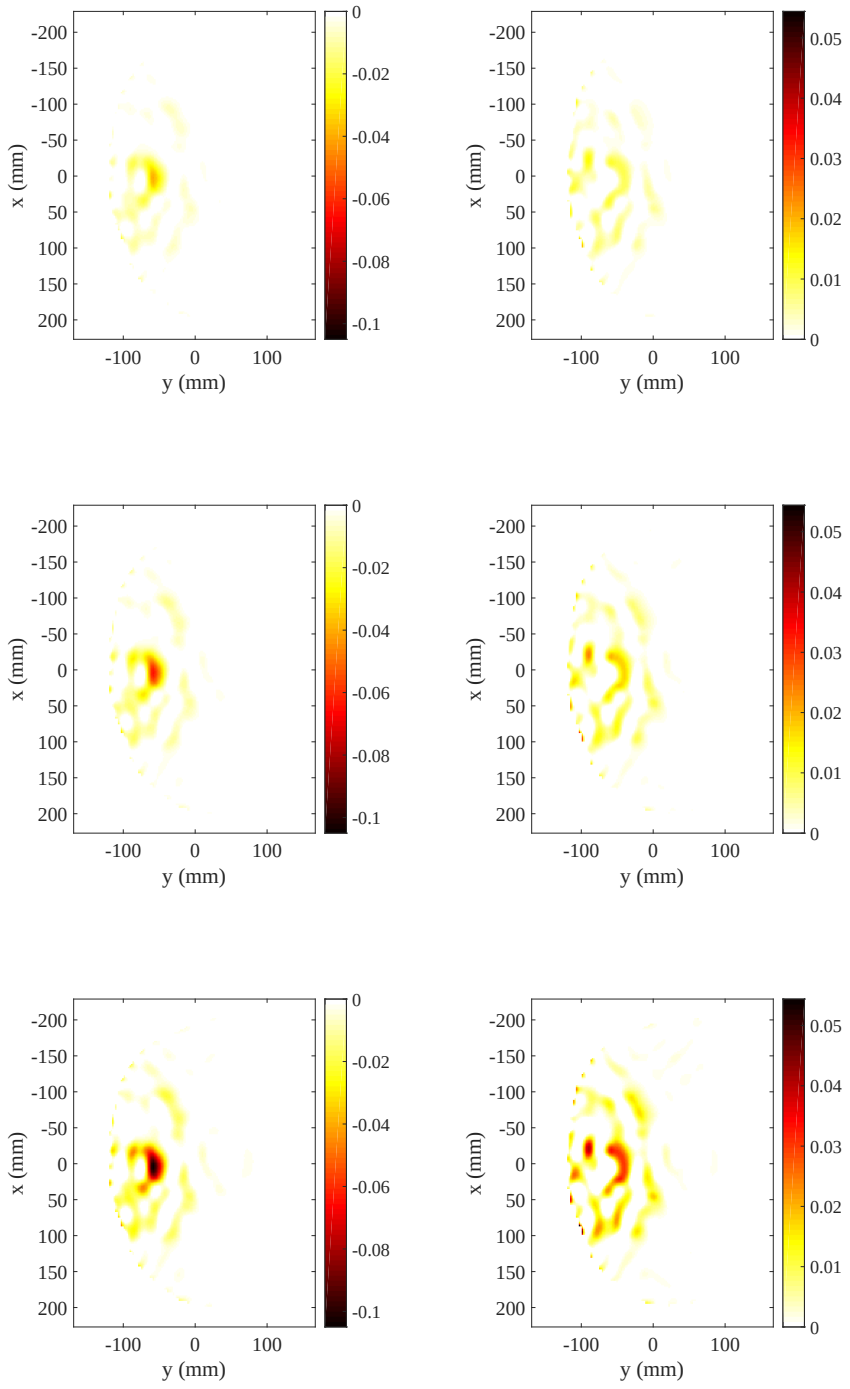

Figure 3.15: Real (left column) and imaginary (right column) part of the retrieved differential contrast starting from the body temperature of 37 °C for the three considered cases: (top row) $\vartheta = 42$ °C ; (middle row) $\vartheta = 45$ °C ; (bottom row) $\vartheta = 50$ °C . 10 antennas in a line

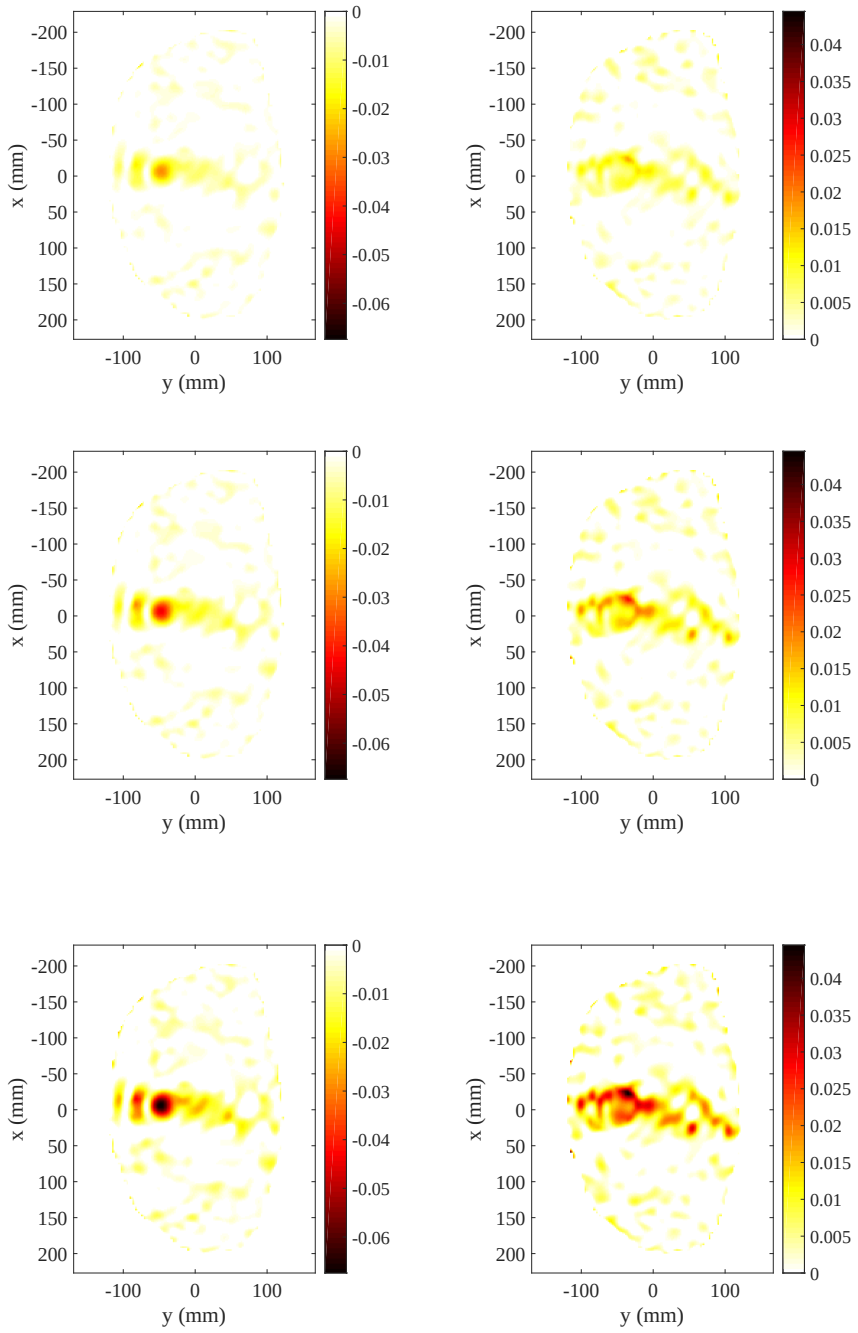

Figure 3.16: Real (left column) and imaginary (right column) part of the retrieved differential contrast starting from the body temperature of 37 °C for the three considered cases: (top row) $\vartheta = 42$ °C ; (middle row) $\vartheta = 45$ °C ; (bottom row) $\vartheta = 50$ °C . 24 antennas on an octagon

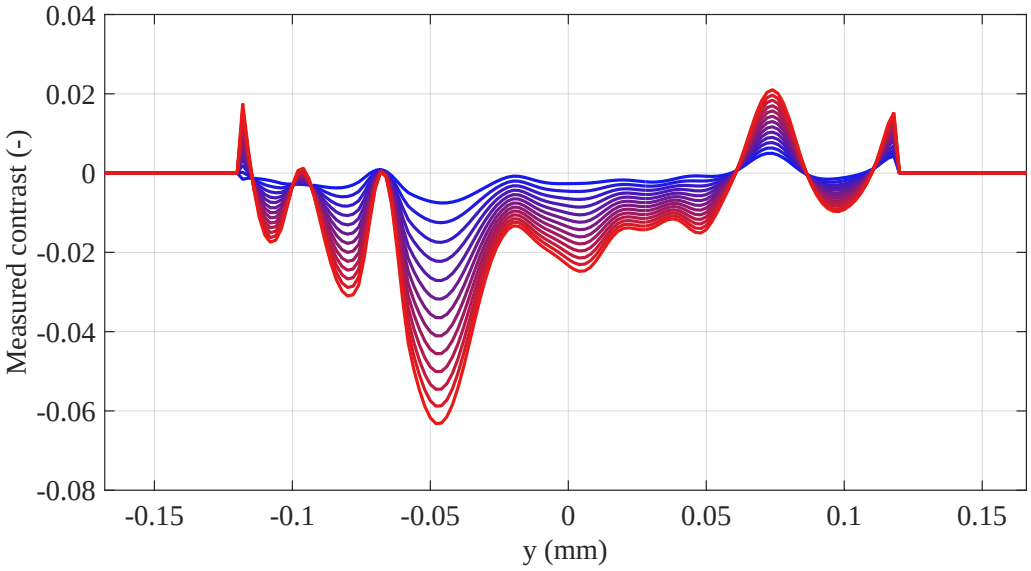

(a) real part

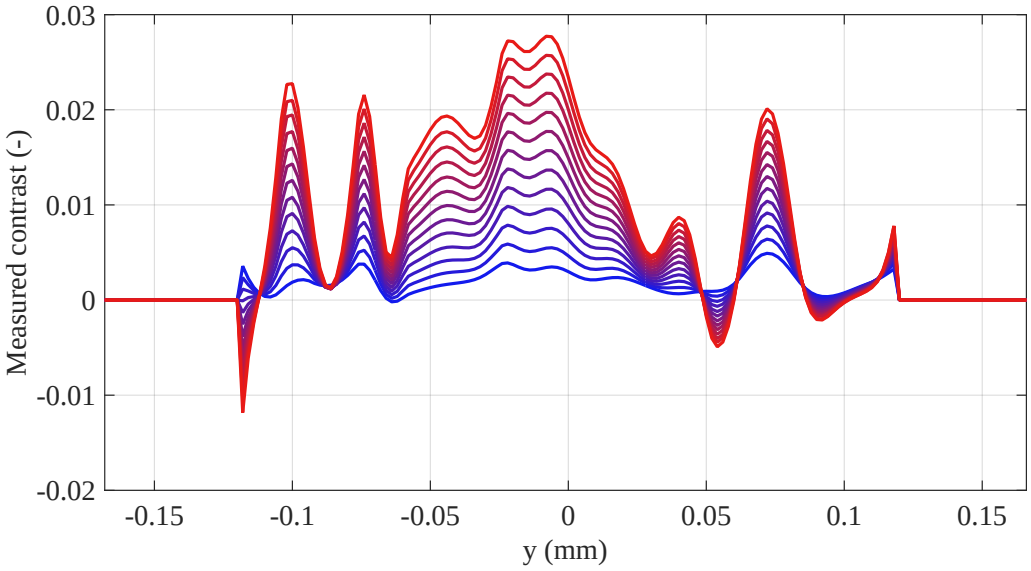

(b) imaginary part

Figure 3.17: Horizontal cut line of the measured changes in dielectric properties for different temperatures. The blue temperature is the change of 1 °C and the red is 13 °C

Retrieved contrast in a horizontal line in the middle of the bladder was depicted in a plot for temperature scenarios in range from 1 to 13 °C , being the blue color the coldest and

red color the hottest scenario (Fig. 3.17). Again, the results confirm that with an increasing temperature, higher amplitude can be retrieved in resulting picture. This dependence is even linear which clearly shows a following Fig. 3.18. The minimal values (both real and imaginary) of each retrieved differential contrast (sign x) were organized into a plot together with the actual differential contrast (sign o) depending on a temperature change. The value decrease is linear, except for few samples with low temperature difference. This is understandable because such a small change evokes very small signal which is then masked under the artefacts caused by approximation. The promising fact one can observe is that the retrieved value exceeds in amplitude the actual contrast.

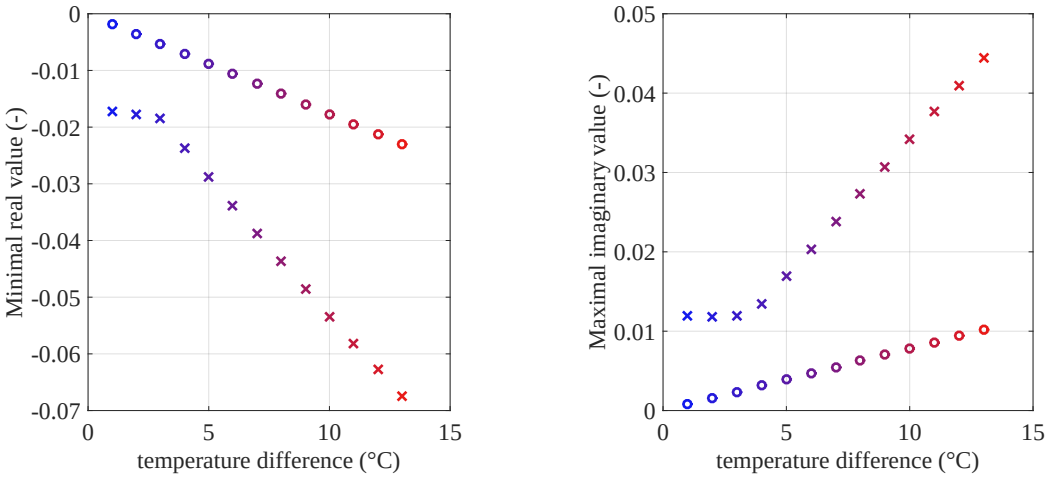

(a) real part (b) imaginary part

Figure 3.18: Minimal real and imaginary part of the retrieved (x) and actual (o) contrast in the dependence on a temperature difference of a bladder. 24 antennas around on an antenna holder

Hot spot detection was analysed in the following Figs. 3.19 and 3.20 by imaging. Always, real and imaginary part of retrieved contrast is shown while black circle represents the location of an actual hot spot. In scenario a, the hot spot was located on a fat and muscle interface and the varying amplitude of actual change complicated the optimal imaging. Despite this fact, the location of the hotspot was correctly determined. In scenario b, hot spot occurred in the muscle tissue. Surprisingly, the target wasn't located accurately and a lot of high intensity artefact were detected.

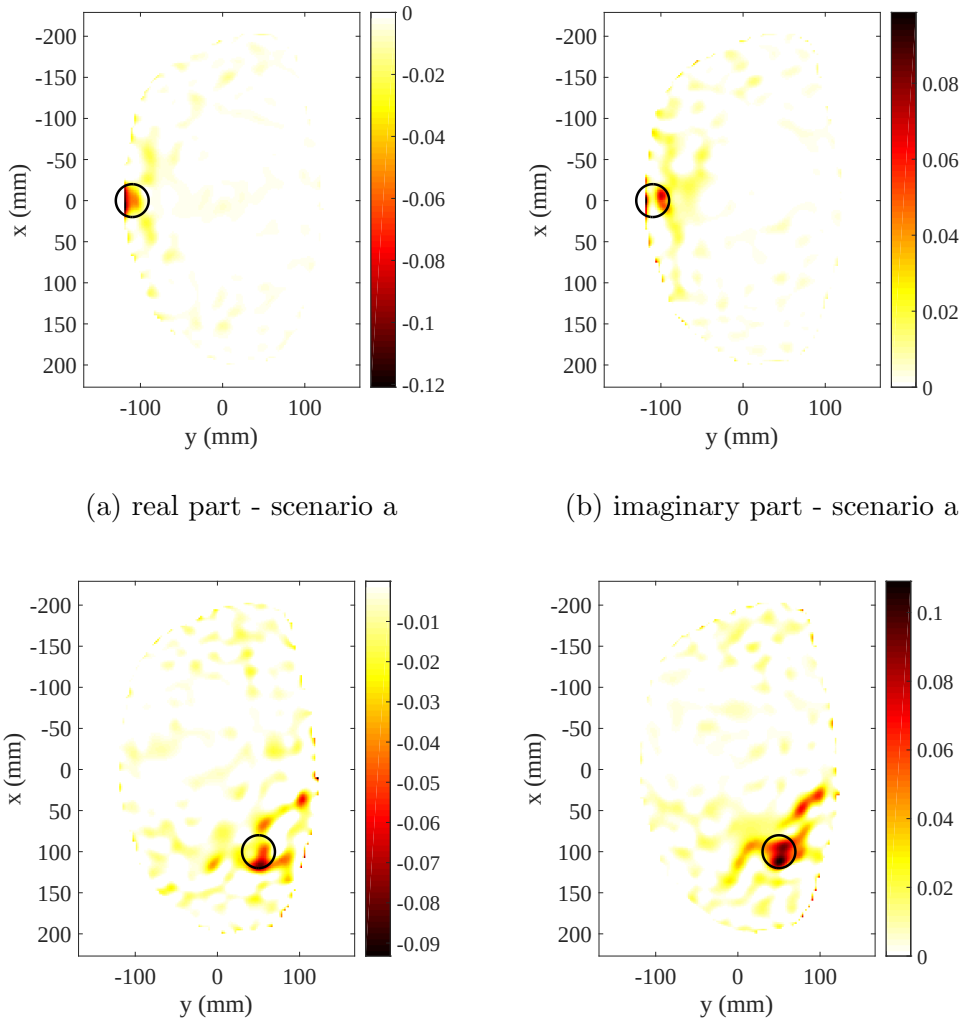

(a) real part - scenario a

(b) imaginary part - scenario a

(c) real part - scenario b

(d) imaginary part - scenario b

Figure 3.19: Real and imaginary part of retrieved contrast of only hot spots scenarios a and b (Table 2.2). ($\vartheta_{hotspot} = 50$ °C) black circle represents the hot spot location

The two differently heated targets have been imaged in Fig. 3.20. In scenario c, the amplitude of change in muscle exceeds the amplitude of bladder change which complicates the imaging, but still in case of real part of the contrast the location of both targets is recognizable. When setting the same temperature of both bladder and muscle tissue - scenario d, the imaging resulted in similar contrast in both targets which indicates the ability of the algorithm to find more targets at once. Very small hot spot was modelled at the interface of muscle and fat in scenario e. Although the radius of the hot spot is tiny, his high temperature change enables the detection in case of imaginary part while in real contrast the location is lost in the artefacts.

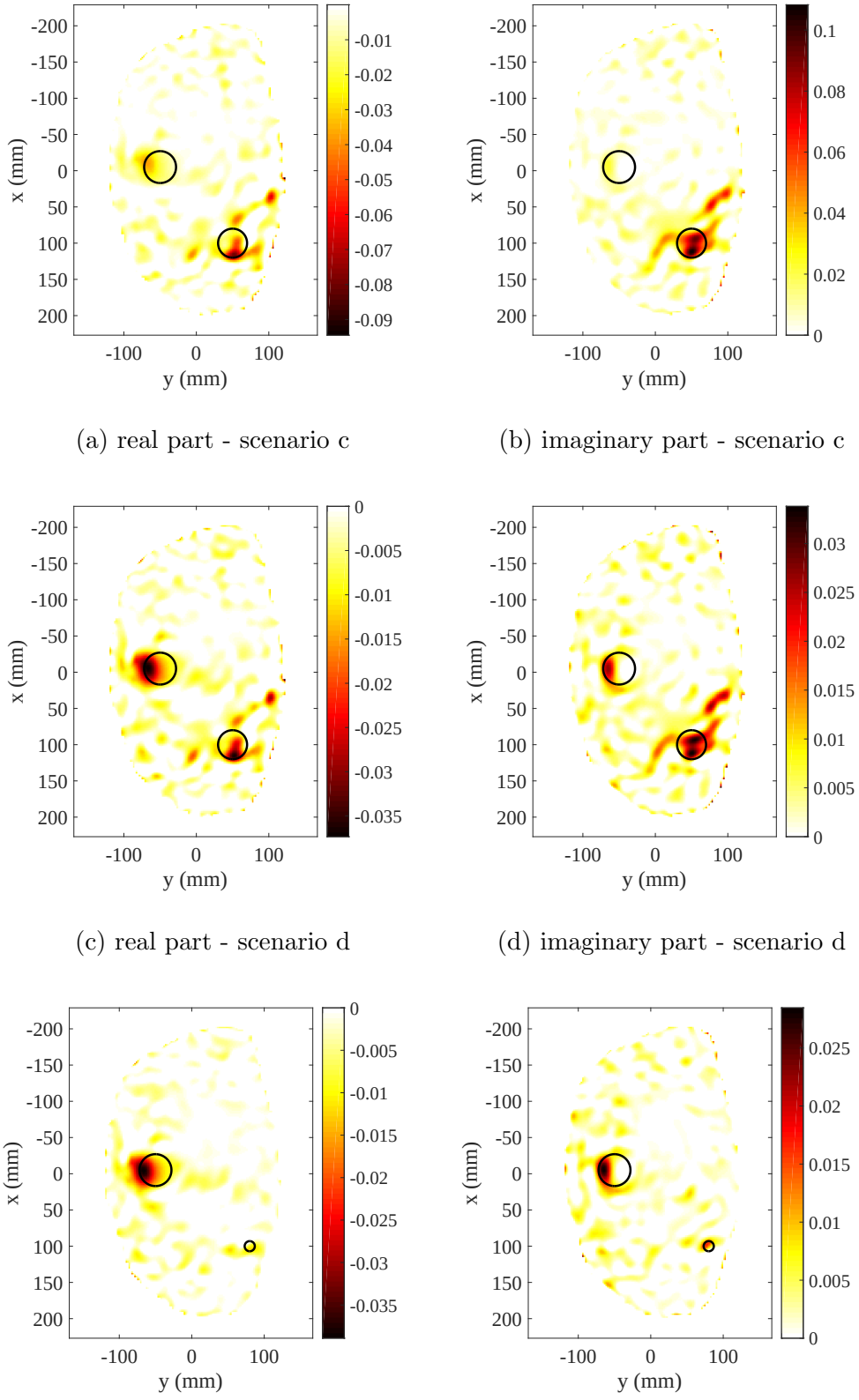

(a) real part - scenario c

(b) imaginary part - scenario c

(c) real part - scenario d

(d) imaginary part - scenario d

(e) real part - scenario e

(f) imaginary part - scenario e

Figure 3.20: Real and imaginary part of retrieved contrast of hot spots and heated bladder: scenarios c, d and e (Table 2.2), black circle represents the hot spot location

Differential contrast computed from data gained by numerical simulations with variability in electric tissue properties is shown in Fig. 3.21. The change between these results and the images without variability (Figs. 3.16(top row) and 3.20c, 3.20d) is not recognizable which indicates, that the variability doesn't have an effect on hyperthermia target detection.

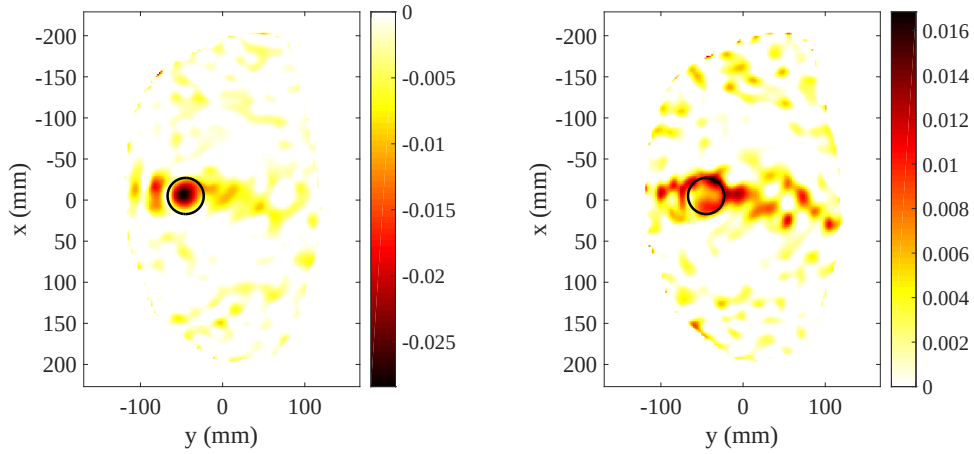

(a) real part - scenario f

(b) imaginary part - scenario f

(c) real part - scenario g

(d) imaginary part - scenario g

Figure 3.21: Retrieved and actual contrast of scenario with simulated tissue properties variability ($\vartheta_{bladder} = 42$ °C , $\vartheta_{hotspot} = 42$ °C)

Modified imaging method was used for data gained by simulations with 24 antennas on an octagon with their working frequency 1 GHz - the imaging was focused only on a bladder framed by square shape. Due to this fact, the curve of normalized singular values of linear operator falls rapidly which means that only a few of the values are needed for the inverse TSVD calculation and the the computation time gets shorter.

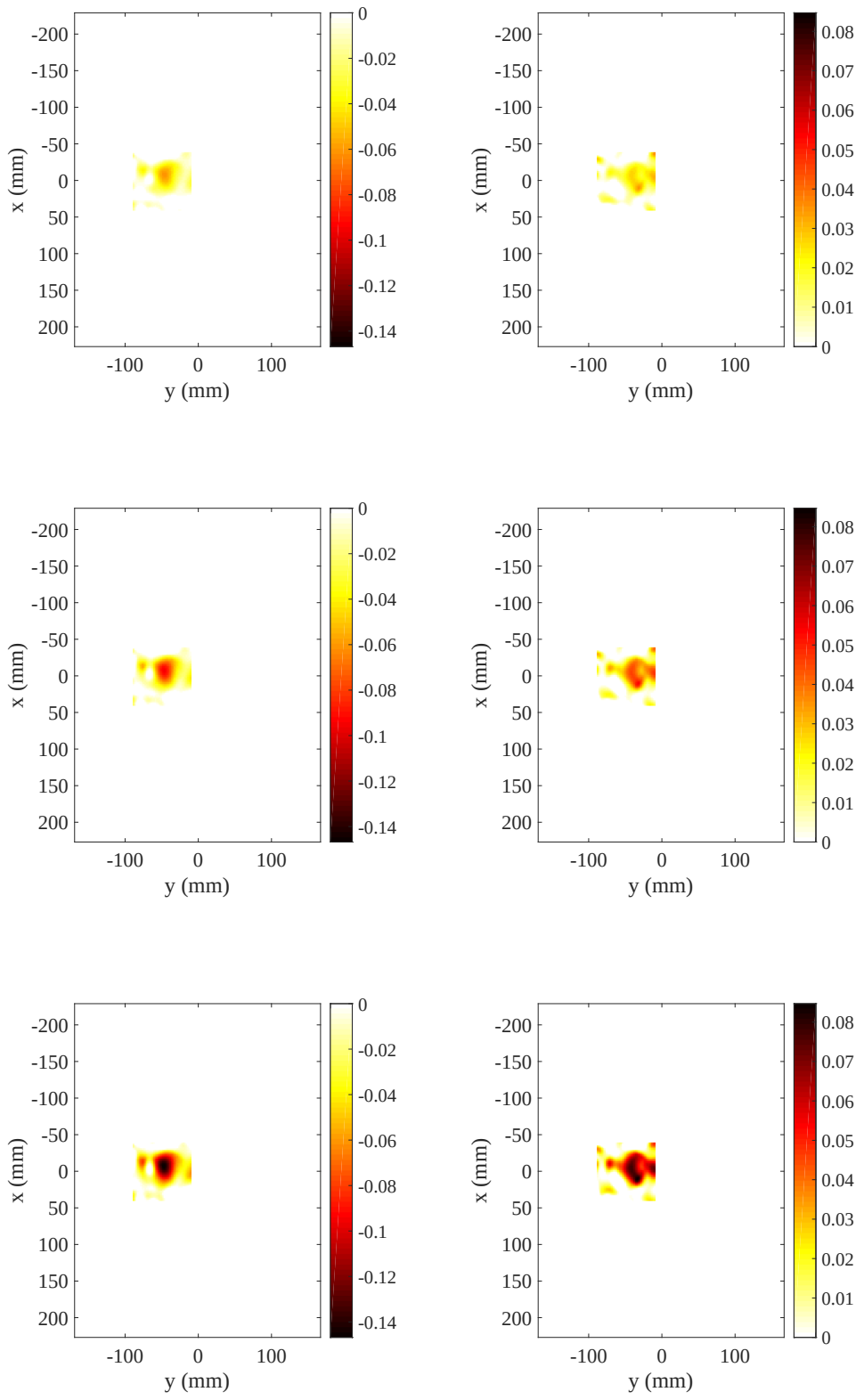

Figure 3.22: Real (left column) and imaginary (right column) part of the retrieved differential contrast starting from the body temperature of 37 °C for the three considered cases: (top row) $\vartheta = 42$ °C ; (middle row) $\vartheta = 45$ °C ; (bottom row) $\vartheta = 50$ °C . 24 antennas in an octagon, targeted on bladder

The Fig. 3.22 represents results imaged with the help of focusing on the target - the bladder. The accuracy can be compared with the actual contrast in Fig. 3.14. With an a priory information about the location of the heated tissue, more accurate results can be obtained, however still some artefacts occur.

Multifrequency imaging algorithm was tested and the results in form of real and imaginary part of actual and retrieved differential contrast are shown in Fig. 3.23. The location of the target was found clearly and smaller number of artefacts can be observed with respect to monochromatic imaging in Fig. 3.16. The positive information is that the retrieved contrast matches the actual contrast more quantitatively accurate than the previous methods, on the other hand, the data necessary for this imaging demand a lot of time for being gained and also being processed and transformed into the image.

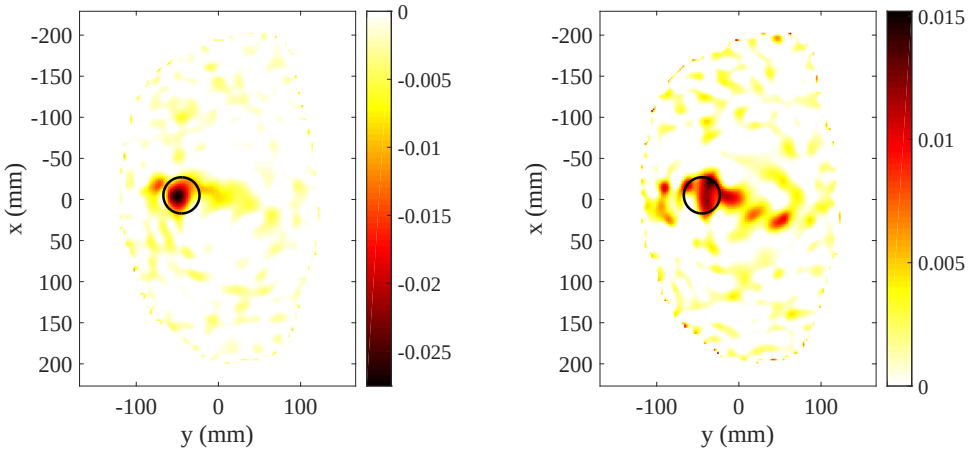

(a) real part of retrieved contrast (b) imaginary part of retrieved contrast

Figure 3.23: Retrieved contrast of scenario ($\vartheta_{bladder}$ = 42 °C), multi frequency imaging algorithm was used.

The results in Fig. 3.24 stand for the number of antennas analysis, where the real and imaginary parts of the retrieved contrast (gained by different number of antennas) are depicted. When taking only 16 antennas from the antenna array, similar result like in case of 24 antenna arrangement was retrieved. After eliminating 4 other antennas, two different situations happened. When the antennas in clusters of three elements were used for calculation while the antenna closest to the target was included, sufficiently good image was retrieved. However, when the antennas were spread symmetrically around the body, location of the target was not correctly found.

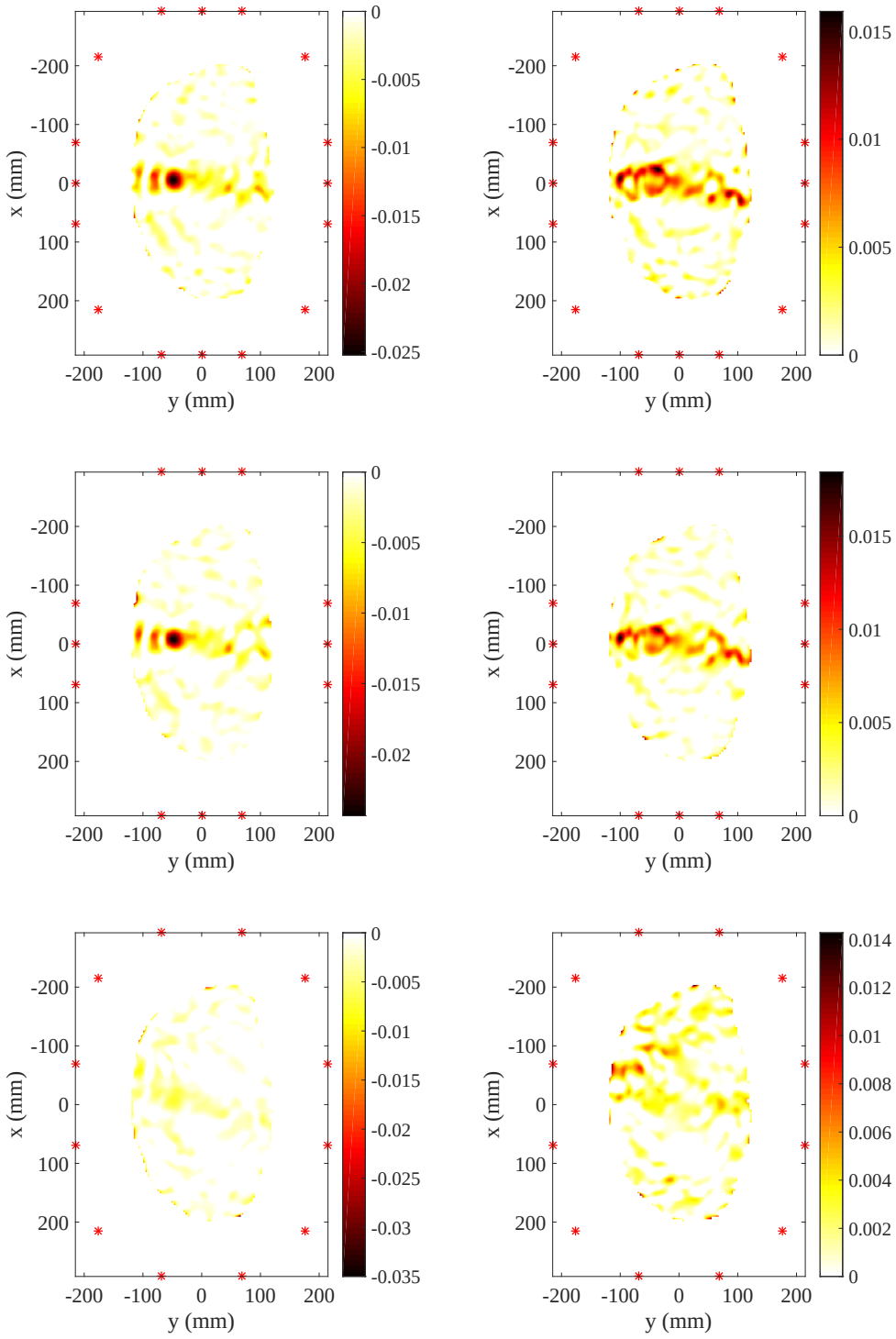

Figure 3.24: Real (left column) and imaginary (right column) part of the retrieved differential contrast starting from the body temperature of 37 °C to the 42 °C for the three considered cases: (top row) 16 antennas ; (middle row) 12 antennas in clusters; (bottom row) 12 antennas spread out; red stars represent the antenna locations

3.4 Images evaluation

In Fig. 3.25, partial results are shown, which led to the final values. Absolute value of the retrieved contrast in 3.25a can be compared with the binary image in 3.25b corresponding to the target which has been chosen according to the threshold −3 dB. At the same figure, center of gravity of the defined target is depicted by a red star. Actual binary contrast (which in reality is also binary) with a green star as its center of gravity can be seen in 3.25c, while the final image - combination of the absolute contrast and a binary mask chosen by the threshold and red and green stars as centres of gravity of retrieved and actual contrast, respectively - is shown in 3.25d.

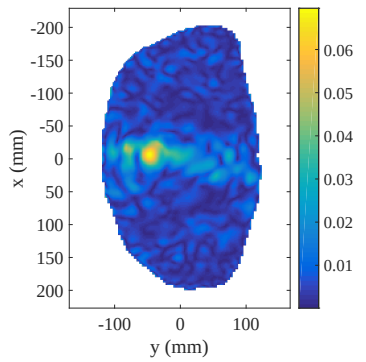

(a) absolute value of retrieved contrast

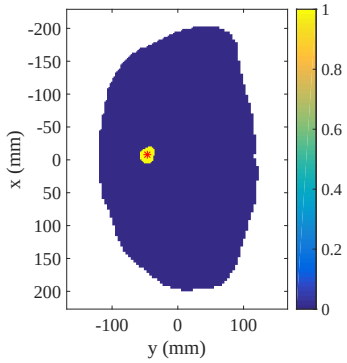

(b) binary mask defining the target

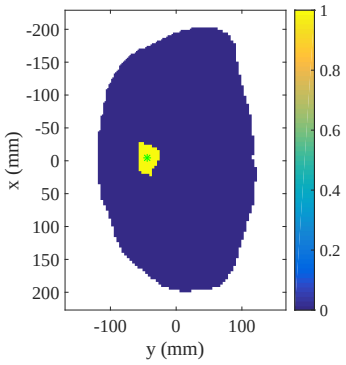

(c) actual binary mask

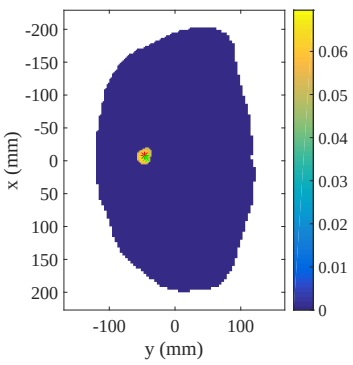

(d) mask applied on a retrieved contrast

Figure 3.25: Results of image evaluation leading to the final values. Red and green stars correspond to the center of gravity of the retrieved and actual target, respectively.

It can be seen, that the −3 dB threshold is quite high and the area around the peak, defining the target, could be also considered. When doing it, the target would increase its

area and thus improve for example the sensitivity and area ratio. From the Fig. 3.25d it is possible to see, how precisely the center of the target was found - the two stars are partially overlapping.

Properties of the retrieved images from scenarios with heated bladder in range from 38 to 50 °C were calculated and their means ± standard deviations were organized into the Table 3.2. This was done in two different ways by changing the threshold for choosing the location and size of the target. When −3 dB was used, no target was defined in case of 1, 2 and 3 °C change because of high level of artefacts and therefore the properties were very different from the others. Because of this, 1-3 °C values were excluded from the means and standard deviations. In case of −6 dB threshold, 1-2 °C values had to be neglected for the same reason. The sensitivity is below 70 % in both thresholds, while with lower threshold better value is obtained. Specificity and accuracy gained in all cases is almost 100 %, but one has to consider the big amount of pixels in the not heated body which makes this value easier to gain. Areal ratio increased with a decreasing threshold as expected, but none of the values reached the actual area. Localization error was measured as ca. 4 mm, being very accurate, and NRMSE around 0.18, saying that the quantitative information of the image is not so different from the truth. The parameter NRMSE is the first one, which shows significantly better results by using higher threshold. One can also see, that the standard deviations are low, meaning that the values didn't fluctuate much. According to this, results from other imaging methods and scenarios were evaluated just considering one image.

Table 3.2: Evaluation characteristics of the 13 scenarios with increasing temperature change according to the used threshold

threshold (dB)	*sensitivity (%)*	*specificity (%)*	*accuracy (%)*	*areal ratio (-)*	*local. error (mm)*	*NRMSE (-)*
−3	35.0 ± 3.4	100.0 ± 0.0	99.0 ± 0.1	0.35 ± 0.03	3.9 ± 0.2	0.178 ± 0.002
−6	66.4 ± 8.8	99.8 ± 0.1	99.3 ± 0.1	0.76 ± 0.12	4.5 ± 0.5	0.191 ± 0.004

Data are presented as arithmetic mean ± standard deviation.

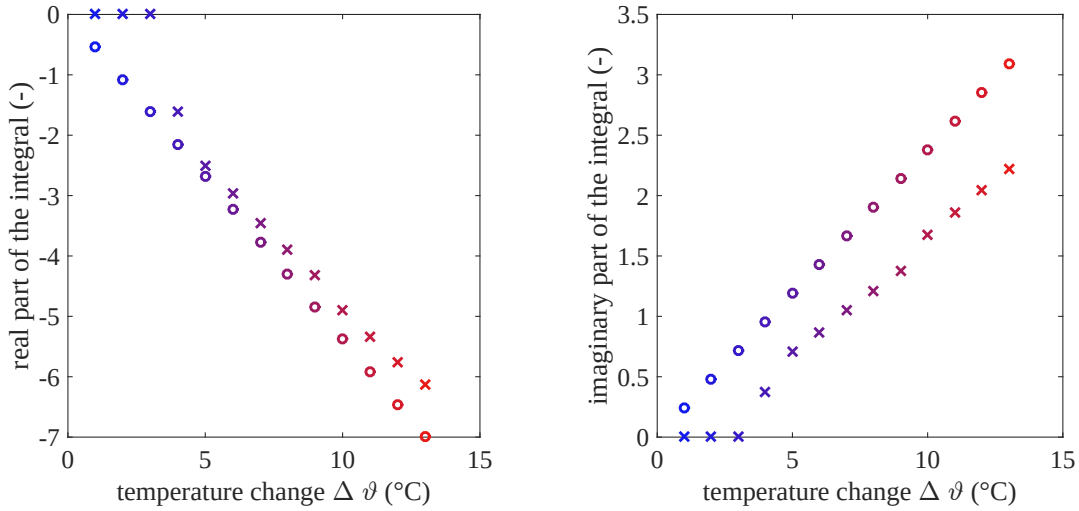

(a) real part (b) imaginary part

Figure 3.26: Real and imaginary part of the integral of the retrieved (x) and actual (o) contrast in the dependence on a temperature difference, threshold −3 dB

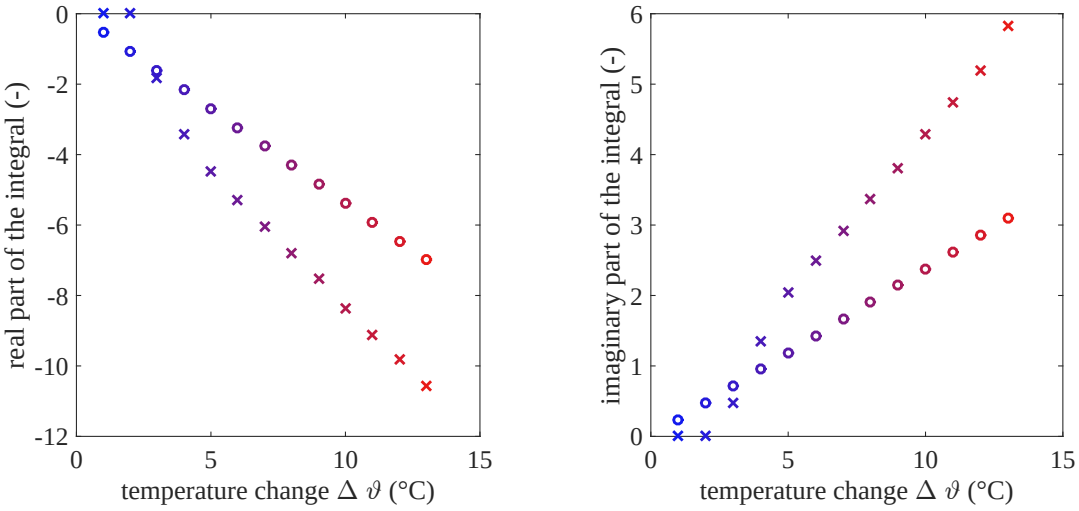

(a) real part (b) imaginary part

Figure 3.27: Real and imaginary part of the integral of the retrieved (x) and actual (o) contrast in the dependence on a temperature difference, threshold −6 dB

The quantitative veracity is described also in Figs. 3.26 and 3.27, where real and imaginary part of the integrals over the target pixels from the retrieved (sign x) and actual (sign o) image are depicted. A clear difference between the two thresholds is noticeable, the higher

one gives much more similar values to the actual. In case of real part of the −3 dB threshold, the retrieved integrals are only 11 % lower in average with respect to the actual. A positive aspect of the integrals is also their linear behaviour with increasing temperature change.

Three different scenarios were evaluated and the results were organized in Table 3.3. The scenario when bladder is heated to 42 °C while focused imaging method is used (Fig. 3.22) is shown in the first two lines. Next two lines belong to the same scenario but imaged by multi frequency algorithm (Fig. 3.23) and the last two lines belong to scenario when bladder was heated to 42 °C and hot spot in the region of muscle occurred at the same time (Figs. 3.20c and 3.20d). The focused case appeared similar to the results from not focused version of the algorithm, mainly the results are slightly better except for NRMSE. All of the results are sufficiently good and focused version at −6 dB even reaches sensitivity over 73 %. Surprisingly, results of the multi frequency imaging were slightly worse than the simple monochromatic imaging, although one would assume the opposite when looking on the retrieved images. The hot spot data deteriorated with respect to the other but still all of the parameters showed the ability to detect both heated targets. When comparing the retrieved and actual integrals, in case of hot spot using −3 dB, only 31 % difference was measured.

Table 3.3: Evaluation characteristics of the 42 °C scenario when focusing on bladder, when imaged with multi frequency and when 42 °C hot spot was present.

	threshold (dB)	*sensitivity (%)*	*specificity (%)*	*accuracy (%)*	*areal ratio (-)*	*local. error (mm)*	*NRMSE (-)*
focused	−3	38.8	100	99.0	0.39	3.0	0.198
	−6	73.4	99.9	99.5	0.79	2.5	0.237
multi frequency	−3	32.2	100	98.9	0.34	4.6	0.181
	−6	63.8	99.8	99.3	0.74	4.2	0.191
hot spot	−3	19.0	100	97.2	0.19	13.8	0.175
	−6	49.3	99.8	98.0	0.55	11.9	0.215

3.5 Experiment

3.5.1 Liquid muscle phantom

The deionized water, IPA and NaCl were mixed and dielectric properties of the mixture were measured afterwards gaining a final recipe for preparing liquid muscle phantom at different temperatures while always a model at 800 MHz frequency was used as a reference. Individual amounts of each ingredient are shown in Table 3.4 for all the chosen temperatures.

Table 3.4: Muscle phantom recipe for different temperatures

temperature (°C)	$H_2O(ratio)$	$IPA(ratio)$	$NaCl(g/l)$
37	0.616	0.384	4.892
42	0.610	0.390	5.636
45	0.606	0.394	6.554
50	0.601	0.399	7.462

In Fig. 3.28, the results of the measurements are shown (in the left the permittivity values and in the right the conductivity values zoomed to the range of interest). The continuous line with the error bar corresponds to the measurement with its type C uncertainty and the dashed line to the computed value from temperature dependent Cole-Cole model. It is possible to compare the three different temperature dependencies: the error bars of the relative permittivity are overlapping, indicating that such small differences are hardly detectable by measurement, while this is not the case of conductivity. A positive result of this analysis is that the liquid phantom's permittivity doesn't correspond to the modelled one only for the 800 MHz frequency but with its uncertainty region it is possible to use this mixture in the whole range from 500 MHz to ca. 1 GHz. On the other hand, the conductivity slopes of measured and computed data are different and in case of using different frequency, the content of NaCl would have to be adjusted. Individual plots of all the temperature measurements are shown in Fig. 5.1 in Appendix.

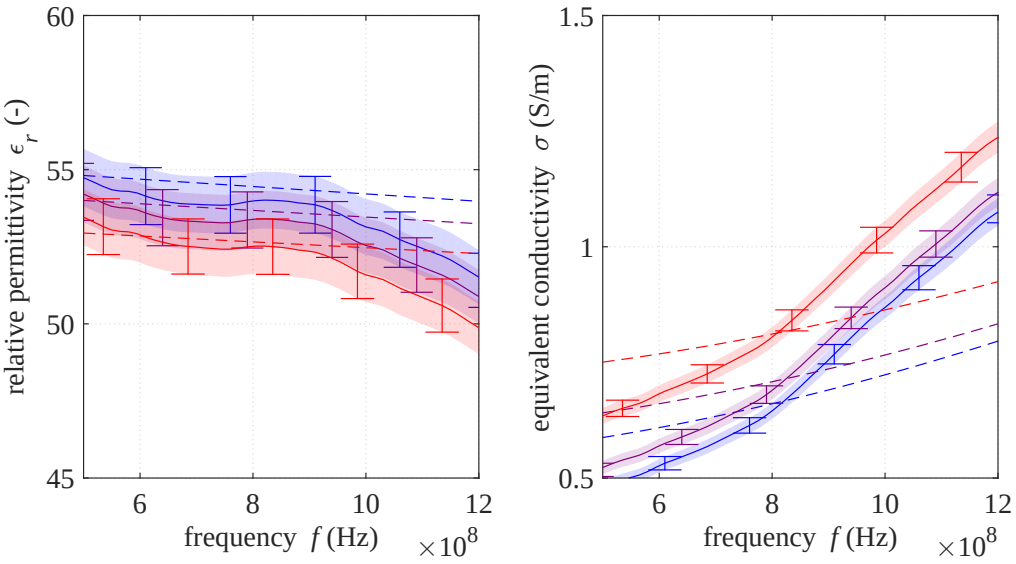

Figure 3.28: Relative permittivity (in the left) and equivalent conductivity (in the right) for different muscle temperatures (blue - 37 °C , purple - 42 °C , red - 50 °C) measured (continuous line) with error bars corresponding to ± type C uncertainty and computed (dashed line).

3.5.2 Antenna holder and pelvic region phantom container

The final assembly of antenna holder and water bolus container, pelvic region phantom container and phantom cover is shown in Fig. 3.29 and technical drawings with all the important dimensions are in the Appendix.

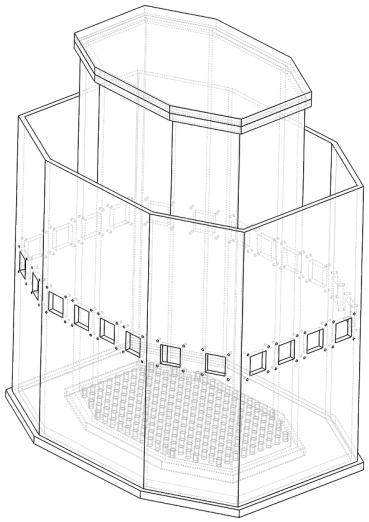

Figure 3.29: Final assembly of all the parts in the measuring system of plexiglass.

The whole geometry was manufactured by an external company and the photographs of the plexiglass components are shown in Fig. 3.30.

(a) pelvic region phantom with a cover

(b) antenna holder

(c) assembly

Figure 3.30: Photographs of plexiglass components of the measuring system

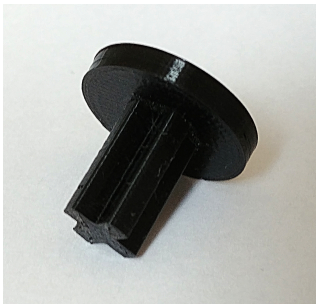

Figure 3.31: Photograph of a pin serving for precise positioning and stabilization of a cylindric phantom.

3.5.3 Protocol of the experiment

Normally, calibration of the measuring device must be done in the beginning of the experiment. However in our case, when differential measurement is performed, vector network analyser doesn't need to be calibrated because the artefacts caused by cables will be subtracted subsequently. On the other hand, DAK device needs to be calibrated before the experiment because the dielectric properties of the liquid phantom will be controlled during the experiment many times.

In the beginning of the experiment, it is important to set a room temperature to 22 °C and in the best case to keep it constant during the whole experiment. Chemicals must be also prepared before the start, namely at least 160 l of H_2O, 63 l of IPA and 870 g of NaCl, which are needed for the liquid phantom and water bolus.

For liquid muscle phantom preparation, following steps must be done. For the 37 °C case ca. 100 l is needed because, 77 l is the volume of the phantom and next 12-14 l will serve for filling the cylindrical phantom of different radii. These phantoms will be inserted inside the pelvic region phantom demonstrating the before treatment state in order to eliminate the influence of the plastic pipe on the result. According to the mixing ratios from Table 3.4, 61.6 l of deionized water must be mixed with 38.4 l of IPA. The IPA should be added little by little so the exothermic reaction doesn't heat the solution too much. The container with the liquid should be kept closed always when it is possible in order to prevent evaporation. Later, 489.2 g must be added to the mixture and dissolve. Mixing of the solution should ensure the homogeneous properties in the volume. When the mixture is prepared and its temperature dropped the 22 °C again, 500 ml sample is taken and its relative permittivity

and equivalent conductivity is measured with the DAK device through the whole frequency range. When this is done, cylindrical containers of 3 different radii are filled with the solution and closed.

For the other liquid temperature phantoms, the same procedure is repeated, but with different ratios and volumes. 20 l will be needed for each of the temperatures, since we have to count with bigger volume used for measuring samples.

Next, the pelvic region phantom must be filled with the liquid 37 °C muscle phantom and into the space around, deionized water must be poured. One cylindrical 37 °C phantom must be inserted into the pelvic phantom into one of the small holes mimicking the bladder position and the coordinates must be recorded. The pelvic phantom is then closed by the cover. In this state, the S-parameters can be measured by the vector network analyser.

When this is done, the 37 °C cylinder is switched by a 42 °C with the same radius. In this way, all of the temperatures are measured and later, different radii and positions can be inserted in the same order.

During the experiment from time to time, the dielectric properties of the muscle liquid phantom should be controlled and recorded.

3.6 3D simulations

Normalized differential scattering matrix was computed from scenario at 600 MHz frequency when target in the center of 10 cm diameter was heated to 42 °C . The result is shown in Fig. 3.32 while the 24^{th} antenna was excluded due to its outlying values. The peak can be found between antennas no. 2 - 3 and 14 - 15, as expected, because these antennas are located on the longer sides of the octagon and the hyperthermia target lies exactly between them. The amplitude of the difference is -36 dB in maximum which even outperforms the scattering matrices gained by 2D simulations.

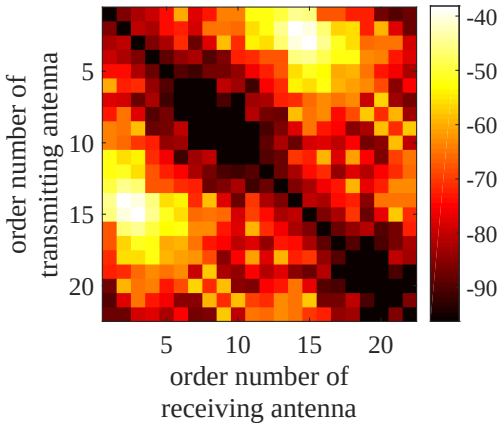

Figure 3.32: Amplitude of normalized differential scattering matrix in dB, $f = 600$ MHz

In Fig. 3.33, real and imaginary parts of the retrieved contrast are depicted, while the area of the heated target is highlighted by a black circle. It is possible to see higher contrast in both parts of the complex values, although there are a lot of artefacts around. When -3 dB threshold was applied in image evaluation, sensitivity 11.7 %, specificity 100 %, accuracy 93.8 %, areal ratio 0.12, localization error 1.7 mm and NRMSE $2.5 \cdot 10^5$ were gained.

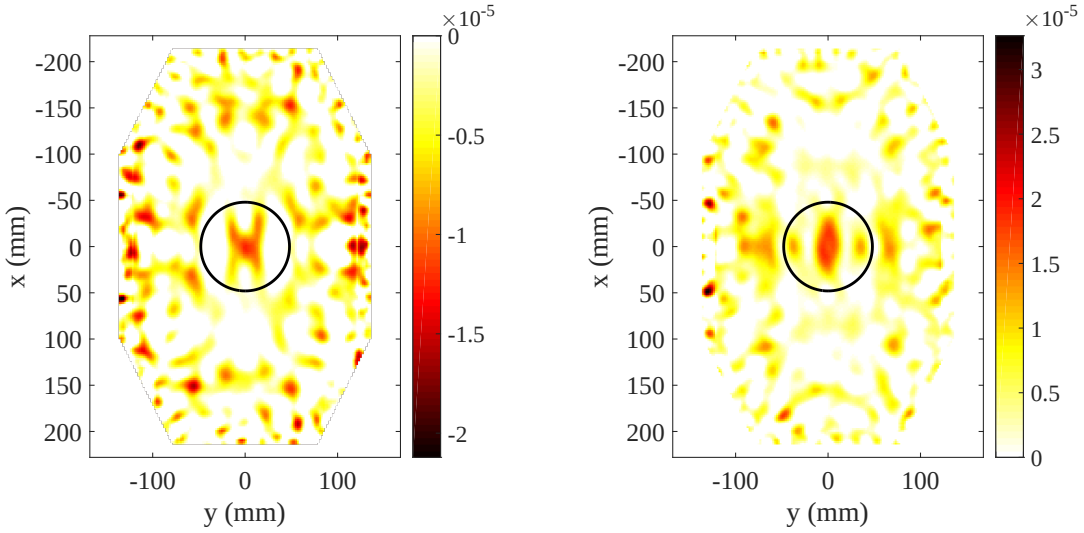

(a) real part (b) imaginary part

Figure 3.33: Retrieved differential contrast, black circle represents the actual location of heated target, $f = 600$ MHz

Scenario, when the target was shifted to the side was imaged and normalized $\Delta\mathbf{S}_{\vartheta_1\vartheta_2}$, is shown in Fig. 3.34 and real and imaginary parts of the retrieved contrast in Fig. 3.35.

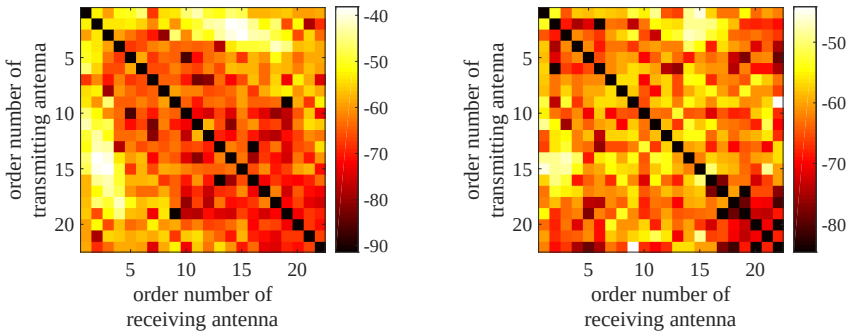

(a) r = 5 cm

(b) r = 2.5 cm

Figure 3.34: Amplitude of normalized differential scattering matrices in dB, f = 600 MHz

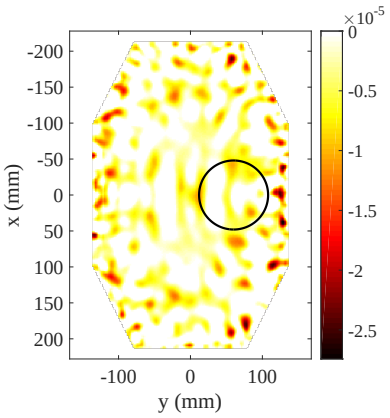

(a) real part, r = 5 cm

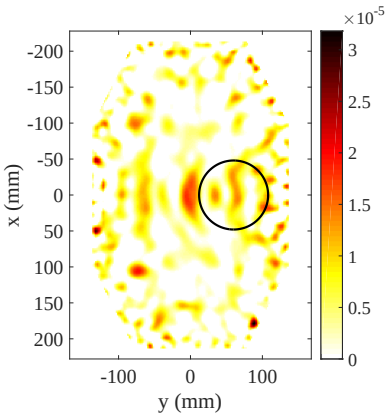

(b) imaginary part, r = 5 cm

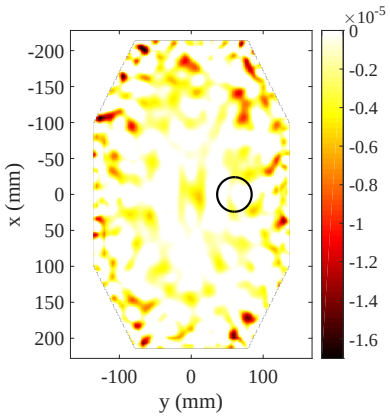

(c) real part, r = 2.5 cm

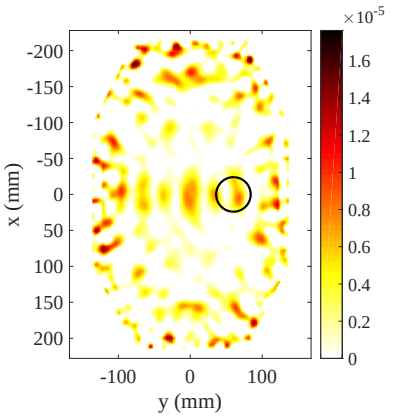

(d) imaginary part, r = 2.5 cm

Figure 3.35: Retrieved differential contrast, black circle represents the actual location of heated target, f = 600 MHz

In both $\Delta\mathbf{S}_{\vartheta_1\vartheta_2}$, one can recognize the peaks similar to the peaks in Fig. 3.32 but the amplitude of the other transmission coefficients intensified and the information about the target is not very clearly defined. Consequently, the retrieved contrast doesn't show any peak except of artefacts in the whole imaging domain. Without any retrieved target location, evaluation properties couldn't be calculated.

Similarly, no target was found in the scenario with small heated region when frequency 800 MHz was applied. However, the results improved a little bit, which can be seen in both differential scattering matrix (Fig. 3.36), where the peak differs a lot from the smallest values, and in the retrieved contrast (Fig. 3.37), where a small correct peak could be recognized in the imaginary values.

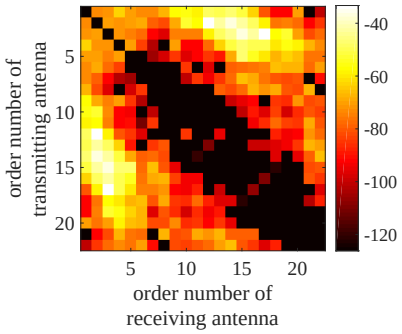

Figure 3.36: Amplitude of normalized differential scattering matrix in dB. $f = 800$ MHz

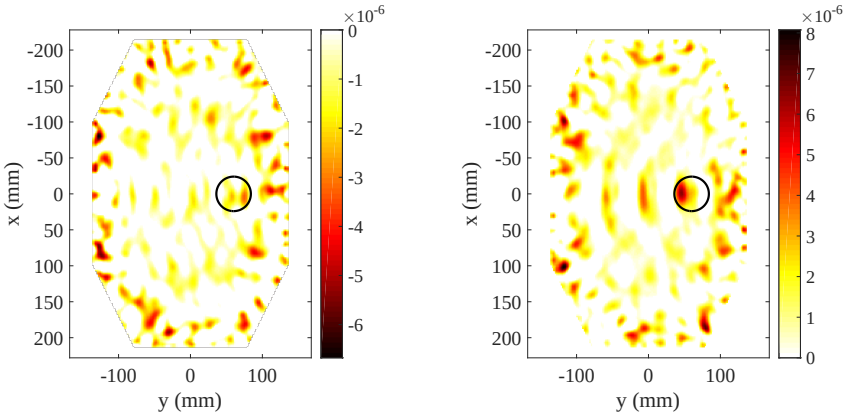

(a) real part (b) imaginary part

Figure 3.37: Retrieved differential contrast, black circle represents the actual location of heated target, $f = 800$ MHz

Chapter 4

Discussion

The main finding of this thesis is the ability of the 2D distorted Born approximation method with TSVD to retrieve a contrast in dielectric properties of human tissues in pelvic region under hyperthermia treatment.

4.1 Numerical phantom

Frequency and temperature dependent numerical anatomically realistic 2D model of the pelvic region was created with the use of Zubal's phantom [26], Cole-Cole model and model of temperature dependency of tissues [16]. This model is highly sufficient for this initial study, although it is still far away from reality. It is important to bear in mind, that the phantom with tissues defined itself is simplified considering only the major internal structures and not their inhomogeneities, and the both Cole-Cole and temperature models only approximate the behaviour of ex-vivo tissue under special conditions. In case of some tissues, for example bladder, the temperature dependence was even estimated from known tissues and not from measured data. As long as the bladder plays such an important role in regional hyperthermia treatment in pelvic region, measured data about its frequency and temperature dependency could bring beneficial information and data about dielectric properties changes of tissues afflicted by tumour or other disease would also help the study. However, the available information gives a sufficiently true picture of the situation.

The Zubal's phantom correspond to a healthy male with hip circumference approx. 111 cm exceeding average value of 94 - 105 cm [61]. When temperature change during hyperthermia should be monitored at a thinner patient, the task would be easier thanks to shorter distance

to the important organs. On the other hand, question may arise what would happen, if an oversized cancer patient was monitored. This scenario was not tested and therefore is not clear if the EM waves could penetrate through such a thick layers. In the end, one should consider, that the analysis is affected by the size of the phantom and can't be related to whole population and further research comparing different types of phantoms could clarify the problem.

4.2 1D analytical analysis

An analytical layered 1D model was created on the basis of the 2D model, while the main organ of interest remained the bladder either filled with urine or empty. The pelvic region layers are unfortunately not very symmetrical and the thickness of each of them changes a lot with a slight change of direction of passing waves. In this thesis, the shortest way from skin to bladder was chosen, because it is easy to define and logical when monitoring the bladder. A movement of the internal organs brings another variability into this model, the bladder itself enlarges when filled with urine and oppositely and so does some of the other organs. Despite of this, the 1D analysis is a simple starting procedure for the feasibility study of temperature monitoring and helpful tool for a quick overview about the optimal measuring conditions. A suitability of each combination of frequency and matching medium permittivity and conductivity was expressed by a power transmission coefficient. The results showed as the most suitable frequency values lower than 0.8 GHz or very low permittivity of matching medium. Because of the common usage of water bolus at the hyperthermia treatment, we accepted the high permittivity value of the matching medium as a requirement and no lower permittivity conditions were tested. Validation of this information wasn't done in this thesis, but if the benefits are proven in the future, it could change a general view on the cooling bolus.

Analysis, which takes into consideration the rising conductivity of deionized water, compared full and empty bladder scenario with the result, that in case of lower frequencies than 0.8 GHz, the full bladder and in range from 0.8 to 1.5 GHz, the empty one seems more suitable.

4.3 Numerical simulations

Different hyperthermia treatment scenarios have been simulated numerically in 2D using MoM. Implementation of this method enabled to easily import anatomically realistic phantom, which in COMSOL Multiphysics would be more complicated. Another positive aspect was the possibility to extract the incident and scattered EM field separately and calculate the direct field from transmitters to receivers which was used for evaluation of signal level of differential scattering matrices. Their level was found measurable with existing devices in different antenna numbers and configurations. The comparison of $\Delta\mathbf{S}_{\vartheta_1\vartheta_2}$ at different hyperthermia temperatures showed, that the signal level increases with rising temperature, as expected. Distribution of normalized induced current density confirmed expectations about higher attenuation in higher working frequencies. Frequency 1.2 GHz was found as the highest possible, although frequency between 800 MHz and 1 GHz would be the most preferable. Induced current density calculation didn't reveal if full or empty bladder is more suitable for temperature monitoring. However, in practise before the hyperthermia treatment, the patients body would have to be imaged by a conventional imaging technique such as MRI or CT to get the information about the complex relative permittivity distribution. This would be used for estimation of the total fields and later for differential contrast retrieval. The more accurate the estimated permittivity distribution is, the more accurate is also the imaging and therefore it is desired that the bladder's shape and size does not change. Empty bladder is a state in which a reference could be considered, since it is the lowest limit of the bladder volume.

In bladder radiotherapy, two methods are used to treat the cancer. The most common is to irradiate the whole bladder and in this case, patients are asked to empty their bladder in order to decrease the volume as much as possible and minimize the size of the target. On the other hand, the second method uses only partial bladder irradiation - just the tumor. Sometimes, it would be beneficial to fill the bladder and move in this way the other healthy organs further from the treatment fields. In [62], it was tested, that bladder wall movements don't differ between full and empty bladder and they can be calculated taking into account the expected treatment time. It is preferable to use a full bladder protocol when partial treatment is applied and healthy tissue is more protected, when the position of the tumor and bladder is aligned, for instance thanks to lipidiol markers. [62]

A similar conclusion can be made about the bladder state during microwave temperature monitoring. If its location and shape is well known, it can be empty or filled based on an organ at risk criteria.

4.4 Imaging and images evaluation

2D Data from different hyperthermia scenarios have been processed by algorithm based on distorted Born approximation and TSVD. Results showed the ability to find the location of heated target with very low error around 4 mm, when the temperature difference exceeded 3 °C . Despite of not optimal gained contrast quantities, the linear behaviour has been found in the differential contrast caused by increasing temperature change which could serve for calibration and quantitatively informative results. Because of the fluctuation of the values in the retrieved function, better comparable quantitative information lies in the integral over the target region. In some cases, these integrals almost matched the actual values, which is a promising finding.

However, the method was not able to reconstruct the shape of the target properly and the size was always underestimated gaining areal ratio between 0.4 to 0.7.

The method showed the ability to reconstruct hot spots occurring individually or in a combination with a desired bladder hyperthermia although again some artefacts were measured and the location and shape wasn't found perfectly. Still, this is an improvement in comparison to what is now used for hot spot localization - patient's complaint and his description of the location. The localization error exceeded the results of scenarios without hot spots, but the NRMSE values demonstrated gaining of a similar quantitatively truthful information.

Variability in dielectric properties distribution was modelled and scenarios with and without hot spot showed almost identical results as when homogeneous tissue properties were used. This finding suggests that the imaging method works also in more realistic conditions. Except of variability in tissue properties itself, one could expect variability in temperature dependency which was not modelled in the study but it could be an interesting part of the further research.

Bringing an a priori information into the algorithm, namely the specification of the location of bladder or other organ of interest, and focusing the imaging only in this region,

led to higher sensitivity, areal ratio and smaller localization error as expected. However, NRMSE got slightly worse, surprisingly.

The multi frequency imaging didn't meet the expectations, that with more input information, more truthful result will be gained. Similar, but slightly worse characteristics were measured for this image and therefore, when also the long measuring and image reconstruction time is taken into account, this method seems not suitable for real time temperature monitoring.

Different antenna element number and positions were tested and an optimal one was searched. The results revealed, that not only number but also the position is important according to the location of the target. When 10 antenna elements were placed in front of the body, the target was localized, which on the other hand didn't happen in a symmetrical 12 antenna configuration. However, 12 antennas distributed in clusters around the body were sufficient for target finding. As a conclusion, it seems that for successful image reconstruction it is desirable to use antenna elements closest to the target and then, the number doesn't have to be so high. In case of preventing hot spots, when the heated spot's location can't be foreseen, 24 antennas seem as a good choice.

Overall, the algorithm based on DBA and TSVD was found useful in temperature change monitoring, because it gave us information about the target temperature and location in a reasonable time (except of the multi frequency approach). Subject of a discussion can be a choice of truncation index. In this study it was mainly done subjectively according to the final result and with respect to the noise added to the scattering matrices. Topic of a further research could be a proper setting of the index maybe also reversely with a help of some image evaluation. Other factor, which affected the target evaluation, was the limit used for thresholding when the size of the target was defined. Two different limits showed that lower limit defines bigger target and improves the sensitivity of the measurement. On the other hand, due to this fact, the NRMSE grows and the integrals over the target differ more, in other words, the quantitative information becomes less truthful. Now, question is if the best choice is to focus on the qualitative results and use lower limit, focus on quantitative results and use the higher limit or find a compromise between both of them.

4.5 Experiment

Antenna chosen for the experiment has its advantages. For example its UWB characteristics could be beneficial if the microwave temperature monitoring was combined with a radar based method. Thanks to this, the precise information about the patient's position could be gained and therefore also more accurate results of the imaged temperature difference could be retrieved. Another positive aspect about the antenna is the UWB balun, which ensures the balanced feeding and proper bow-tie antenna radiation. Although the antenna was optimized for being attached directly to the muscle, numerical simulations revealed, that a meaningful signal is transmitted also in the water bolus in the desired frequency range. Another advantage is the small size of the antenna and therefore a possibility to incorporate such a big amount of them around the pelvic phantom. On the other hand, the small size could be seen also as a disadvantage, because it causes weaker radiated signal.

The temperature change in the liquid muscle phantom was not simulated by microwave hyperthermia and also not by heat delivery through another system, because of too hardly predictable heat transfer and a complexity of finding proper temperature dependent liquid phantom. In this initial study, the main goal was to test imaging method and this is done the most easily when actual measurement conditions are fixed and well known. Having stable and clear conditions enables us to find changes in the imaging process and optimizing the shortcomings. A future research on imaging should involve temperature dependent phantom and real heat delivery, which would bring a challenge about maintaining constant temperature in space and time. The most complex research would combine microwave imaging with microwave hyperthermia system and would have to deal with the compatibility of two antenna types working on different frequencies and with different power.

When searching for a recipe for the liquid muscle phantom, one should bear in mind, that the DAK device has its own limitations just as the measuring tools like graduated cylinder and automatic pipette do. Also the measuring procedure requires the sample to be in contact with air, which causes the evaporation (IPA faster) and change in content ratio. By every single measurement a small amount of the sample is lost due the cleaning of the measuring probe which again distorts the known content. Last but not least, it is complicated to maintain the temperature of the samples constant and if it would be measured so, the thermometer has its own error. However, the accurate relative permittivity and equivalent conductivity is not the most important output of the measurement, since it can vary from

patient to patient and also in one patient's tissue. Also, the desired value coming from the temperature dependent Cole-Cole model is only an estimation and approximation of the real values. The important characteristic of the prepared temperature phantoms is their difference and this was reached successfully by the different content of the mixtures.

The control temperature phantoms measurement showed that the approximate value of the samples (calculated from the model [16]) was found in the range of the type C uncertainty of the DAK device. A positive aspect is, that the relative permittivity of the prepared mixtures corresponds to a wider range of frequencies, than just for the 800 MHz. Therefore, when different frequency is used, just conductivity of the solution should be adjusted by adding NaCl.

The disadvantage of the liquid phantom is the quick evaporation of the IPA and therefore instability of the dielectric properties. Also, IPA is flammable and harmful. On the other hand, it is relatively non-toxic and accessible.

System of mimicking a temperature change in specified region of the pelvic phantom was found. The cylindrical containers are practical, because they can be prepared before the experiment starts, closed and inserted in the pelvic phantom when necessary. The screw cap facilitates the repeated measurement of the liquid or its replacement and the pin eliminates the dealing with cylinder position measurement.

Thanks to the change in orientation of the antenna holder and pelvic region phantom to vertical, we decreased the volume of liquid phantom needed for measurement from 108 l to ca. two thirds: 77 l. The vertical orientation makes the incorporation of the different temperature phantoms and manipulation with them easier and also positively affects the water pressure on the antennas: the pressure is the same on all of them and it is only partial with respect to the pressure on low located antennas in the horizontal position. The homogeneous pressure distribution should help to avoid the different antenna behaviour in the low part of the holder just as big problems with sealing up the small holes between antenna substrate and a balun. However, the perfect sealing up of the holes still remains challenging.

The most challenging part of the experiment probably lies in the work with the huge amounts of liquids. The differences between the various temperature phantoms are small, so the material content ratios must correspond to the determined values precisely. Together with the accuracy, it will be desirable to work quickly because of the fast IPA evaporation.

In an optimal state, some measuring device could be used for the measuring such a big volumes accurately and quickly. Once all the liquids are prepared and some of them sealed in the cylindrical containers, the measurement process shouldn't be problematic because of experience from many similar projects successfully done in the CTU laboratory.

4.6 3D simulations

The planned experiment was modelled in 3D using COMSOL Multiphysics. The geometry truthfully copied the real measurement system, except of the temperature phantom container shape with screw cap and other details. This modification should not affect the result since the cylinder wall is only 2 mm thick and with very low relative permittivity and conductivity. Disadvantage of these 3D numerical simulations lies in the computationally high demands. The simulations with more than 5 million elements running on the computer with AMD Ryzen 5 3600 6-Core Processor 3.59 GHz with 63.9 GB RAM were finished in ca. 3 days.

The results of the central target case (600 MHz) showed only partially positive results. A peak was clearly defined in the normalized differential matrix with reasonable signal level, but in the retrieved contrast, only a small indication of target was found. The thresholding method found the target with only 1.7 mm localization error, but the NRMSE was extremely high. For the other target localization and shape, no target was found and the imaging domain was only filled with artefacts. The reason is probably too low signal level penetrating into the pelvic phantom caused by the small size of the antennas and by big difference in conductivity between matching medium (water bolus) and muscle. Also according to the reflection coefficient of the UWB antenna, which is around -7 dB, the transmitted energy is quite low. Majority of the signal gets lost in the matching medium and is measured on the neighbouring antennas. The reason why the 2D simulations resulted in such a good contrast is probably the fact, that the antennas were modelled as incident fields radiated by line sources and the antenna with real geometry radiates with lower intensity.

Results of 800 MHz scenario showed higher contrast in both scattering matrix and retrieved function, but still the target was hardly recognizable. It confirmed, that the transmitted power from the antennas increased, but it wasn't enough. Higher attenuation in higher frequency, on the other hand, can play against the increasing of the working frequency.

In the future, before the experiment is realized, changes must be implemented into the model and better results must be retrieved. One of the possibly improving modification is an increase of the matching medium conductivity, second option is a different positioning of the antenna's bow-ties - not vertically but horizontally. This should reduce the signal coupled on the neighbouring antennas which doesn't carry any meaningful information.

Chapter 5

Conclusion

A feasibility study of microwave temperature monitoring in the pelvic region during regional microwave hyperthermia treatment was conducted. In 2D case, it was proven, that a microwave imaging system can be capable of detecting slight changes in dielectric properties arising due to the temperature change. The algorithm based on distorted Born approximation with TSVD enabled to retrieve both qualitatively and quantitatively informative image. Due to the linearity in the retrieved signal with raising temperature change, there is a potential to calibrate the system in order to appraise the accurate temperature distribution.

As emerged from the analysis of a layered 1D model and antropomorphic 2D model, the most suitable frequencies are between 0.5 and 1.2 GHz while lower matching medium relative permittivity is preferable at higher frequencies. Neither full nor empty bladder was found as a requirement with respect to treatment and monitoring. If the shape and location of the bladder is known, its state can be chosen according to the preceding or subsequent treatment. During whole pelvic region monitoring in order to prevent hot spots occurrence, use of 24 antennas is recommended. However, when the imaging is focused on some organ or region, lower number of antennas should be sufficient when placed close to it.

Imaging method based on DBA with TSVD applied to 2D synthetic data revealed target detection with $35 - 70$ % sensitivity, 4 mm localization error and NRMSE around 0.2. Temperature change higher than 3 °C was successfully found, similarly to hot spots occurring individually or in combination with desirable hyperthermia target.

An experiment representing the temperature monitoring during hyperthermia was designed optimizing the already existing system and combining it with proper antenna elements. The temperature change in the system is mimicked by an insertion of a cylindrical

container with different liquid content. As a material for liquid phantoms, water, IPA and NaCl was chosen and suitable ratios were measured for reaching dielectric properties of muscle at different temperatures.

Corresponding numerical experiment was done in COMSOL Multiphysics and the data were used for imaging. The target was found in only 1 of the four scenarios and therefore modifications must be implemented into the experiment in order to gain successful results.

References

[1] SCAPATICCI, R., O. M. BUCCI, I. CATAPANO and L. CROCCO. Differential Microwave Imaging for Brain Stroke Followup. *International Journal of Antennas and Propagation*. 2014, 1-11. DOI: 10.1155/2014/312528. ISSN 1687-5869. Available at: http://www.hindawi.com/journals/ijap/2014/312528/

[2] FISER, Ondrej, Ilja MERUNKA and Jan VRBA. Microwave hyperthermia system for head and neck area with noninvasive UWB temperature change detection. 2017 *Progress In Electromagnetics Research Symposium - Spring (PIERS)* [online]. IEEE, 2017, 2017, 1657-1662 [cit. 2020-03-03]. DOI: 10.1109/PIERS.2017.8262015. ISBN 978-1-5090-6269-0. Available at: http://ieeexplore.ieee.org/document/8262015/

[3] KOK, H. P., L. KORSHUIZE-VAN STRATEN, A. BAKKER, R. DE KROON – OLDENHOF, G. H. WESTERVELD, E. VERSTEIJNE, L. J. A. STALPERS a J. CREZEE. Feasibility of on-line temperature-based hyperthermia treatment planning to improve tumour temperatures during locoregional hyperthermia. *International Journal of Hyperthermia* [online]. 2017, 34(7), 1082-1091 [cit. 2019-11-12]. DOI: 10.1080/02656736.2017.1400120. ISSN 0265-6736. Available at: https://www.tandfonline.com/doi/full/10.1080/02656736.2017.1400120

[4] HAYNES, Mark, John STANG and Mahta MOGHADDAM. Real-time Microwave Imaging of Differential Temperature for Thermal Therapy Monitoring. *IEEE Transactions on Biomedical Engineering* [online]. 2014, 61(6), 1787-1797 [cit. 2020-03-03]. DOI: 10.1109/TBME.2014.2307072. ISSN 0018-9294. Available at: http://ieeexplore.ieee.org/document/6746099/

[5] CHICHEŁ, Adam, Janusz SKOWRONEK, Magda KUBASZEWSKA and Marek KANIKOWSKI. Hyperthermia – description of a method and a review of clinical ap-

plications. *Reports of Practical Oncology & Radiotherapy* [online]. 2007, 12(5), 267-275 [cit. 2020-02-20]. DOI: 10.1016/S1507-1367(10)60065-X. ISSN 15071367. Available at: https://linkinghub.elsevier.com/retrieve/pii/S150713671060065X

[6] VAN DER ZEE, Jacoba, Dionisio GONZÁLEZ, Gerard C VAN RHOON, Jan DP VAN DIJK, Wim LJ VAN PUTTEN and Augustinus AM HART. Comparison of radiotherapy alone with radiotherapy plus hyperthermia in locally advanced pelvic tumours: a prospective, randomised, multicentre trial. *The Lancet* [online]. 2000, 355(9210), 1119-1125 [cit. 2020-02-28]. DOI: 10.1016/S0140-6736(00)02059-6. ISSN 01406736. Available at: https://linkinghub.elsevier.com/retrieve/pii/S0140673600020596

[7] ROSER, Max and Hannah RITCHIE. Cancer. *Our World in Data* [online]. 2020 [cit. 2020-03-09]. Available at: https://ourworldindata.org/cancer

[8] DEWHIRST, M. W., B. L. VIGLIANTI, M. LORA-MICHIELS, M. HANSON and P. J. HOOPES. Basic principles of thermal dosimetry and thermal thresholds for tissue damage from hyperthermia. *International Journal of Hyperthermia* [online]. 2009, 19(3), 267-294 [cit. 2020-02-20]. DOI: 10.1080/0265673031000119006. ISSN 0265-6736. Available at: https://www.tandfonline.com/doi/full/10.1080/0265673031000119006

[9] CANTERS, R. A. M., M. FRANCKENA, J. VAN DER ZEE and G. C. VAN RHOON. Optimizing deep hyperthermia treatments: are locations of patient pain complaints correlated with modelled SAR peak locations? *Physics in Medicine and Biology* [online]. 2011, 56(2), 439-451 [cit. 2020-03-02]. DOI: 10.1088/0031-9155/56/2/010. ISSN 0031-9155. Available at: http://stacks.iop.org/0031-9155/56/i=2/a=010?key=crossref.91edda784ba7cdf0e903ce7948bc1eff

[10] DE GREEF, M., H. P. KOK, D. CORREIA, A. BEL and J. CREZEE. Optimization in hyperthermia treatment planning: The impact of tissue perfusion uncertainty. *Medical Physics* [online]. 2010, 37(9), 4540-4550 [cit. 2020-03-02]. DOI: 10.1118/1.3462561. ISSN 00942405. Available at: http://doi.wiley.com/10.1118/1.3462561

[11] LÜDEMANN, Lutz, Waldemar WLODARCZYK, Jacek NADOBNY, Mirko WEIHRAUCH, Johanna GELLERMANN and Peter WUST. Non-invasive magnetic resonance thermography during regional hyperthermia. *International Journal of Hyperthermia* [online]. 2010, 26(3), 273-282 [cit. 2020-

03-02]. DOI: 10.3109/02656731003596242. ISSN 0265-6736. Available at: http://www.tandfonline.com/doi/full/10.3109/02656731003596242

[12] SACCOMANDI, Paola, Emiliano SCHENA and Sergio SILVESTRI. Techniques for temperature monitoring during laser-induced thermotherapy: An overview. *International Journal of Hyperthermia* [online]. 2013, 29(7), 609-619 [cit. 2020-03-02]. DOI: 10.3109/02656736.2013.832411. ISSN 0265-6736. Available at: http://www.tandfonline.com/doi/full/10.3109/02656736.2013.832411

[13] BRUNERS, Philipp, Ganga D. PANDEYA, Elena LEVIT, et al. CT-based temperature monitoring during hepatic RF ablation: Feasibility in an animal model. *International Journal of Hyperthermia* [online]. 2012, 28(1), 55-61 [cit. 2020-03-03]. DOI: 10.3109/02656736.2011.619155. ISSN 0265-6736. Available at: http://www.tandfonline.com/doi/full/10.3109/02656736.2011.619155

[14] ARTHUR, R. M., W. L. STRAUBE, J. W. TROBAUGH and E. G. MOROS. Non-invasive estimation of hyperthermia temperatures with ultrasound. *International Journal of Hyperthermia* [online]. 2009, 21(6), 589-600 [cit. 2020-03-03]. DOI: 10.1080/02656730500159103. ISSN 0265-6736. Available at: http://www.tandfonline.com/doi/full/10.1080/02656730500159103

[15] WINTER, Lukas, Celal ÖZERDEM, Werner HOFFMANN, et al. Design and Evaluation of a Hybrid Radiofrequency Applicator for Magnetic Resonance Imaging and RF Induced Hyperthermia: Electromagnetic Field Simulations up to 14.0 Tesla and Proof-of-Concept at 7.0 Tesla. *PLoS ONE* [online]. 2013, 8(4) [cit. 2020-03-03]. DOI: 10.1371/journal.pone.0061661. ISSN 1932-6203. Available at: http://dx.plos.org/10.1371/journal.pone.0061661

[16] LEY, Sebastian, Susanne SCHILLING, Ondrej FISER, Jan VRBA, Jürgen SACHS and Marko HELBIG. Ultra-Wideband Temperature Dependent Dielectric Spectroscopy of Porcine Tissue and Blood in the Microwave Frequency Range. *Sensors* [online]. 2019, 19(7) [cit. 2019-10-04]. DOI: 10.3390/s19071707. ISSN 1424-8220. Available at: https://www.mdpi.com/1424-8220/19/7/1707

[17] FISER, Ondrej, Marko HELBIG, Juergen SACHS, Sebastian LEY, Ilja MERUNKA and Jan VRBA. Microwave non-invasive temperature monitoring using UWB radar for

cancer treatment by hyperthermia. *Progress In Electromagnetics Research* [online]. 2018, 162, 1-14 [cit. 2020-03-03]. DOI: 10.2528/PIER17111609. ISSN 1559-8985. Available at: http://www.jpier.org/PIER/pier.php?paper=17111609

[18] SCAPATICCI, Rosa, Vanni LOPRESTO, Rosanna PINTO, Marta CAVAGNARO and Lorenzo CROCCO. Monitoring Thermal Ablation via Microwave Tomography: An Ex Vivo Experimental Assessment. *Diagnostics* [online]. 2018, 8(4) [cit. 2020-03-03]. DOI: 10.3390/diagnostics8040081. ISSN 2075-4418. Available at: http://www.mdpi.com/2075-4418/8/4/81

[19] MEANEY, P.M., M.W. FANNING, Q. FANG and K.D. PAULSEN. Initial experience with a microwave imaging system for monitoring temperature change in an animal model. *2001 Conference Proceedings of the 23rd Annual International Conference of the IEEE Engineering in Medicine and Biology Society* [online]. IEEE, 2001, , 2844-2847 [cit. 2020-03-04]. DOI: 10.1109/IEMBS.2001.1017379. ISBN 0-7803-7211-5. Available at: http://ieeexplore.ieee.org/document/1017379/

[20] MEANEY, Paul M., Tian ZHOU, Margaret W. FANNING, Shireen D. GEIMER and Keith D. PAULSEN. Microwave thermal imaging of scanned focused ultrasound heating: Phantom results. *International Journal of Hyperthermia* [online]. 2009, 24(7), 523-536 [cit. 2020-03-03]. DOI: 10.1080/02656730801944922. ISSN 0265-6736. Available at: http://www.tandfonline.com/doi/full/10.1080/02656730801944922

[21] MALLORQUI, J.J., A. BROQUETAS, L. JOFRE and A. CARDAMA. Non-invasive active thermometry with a microwave tomographic scanner in hyperthermia treatments in hyperthermia treatments. *Applied Computational Electromagnetics Society Journal*. 1992, 7(2), 121-127. ISSN 1054-4887.

[22] JOACHIMOWICZ, N., C. PICHOT and J.P. HUGONIN. Inverse scattering: an iterative numerical method for electromagnetic imaging. *IEEE Transactions on Antennas and Propagation* [online]. 1991, 39(12), 1742-1753 [cit. 2020-03-06]. DOI: 10.1109/8.121595. ISSN 0018-926X. Avaialble at: http://ieeexplore.ieee.org/document/121595/

[23] MALLORQUI, J.J., N. JOACHIMOWICZ, A. BROQUETAS and J.Ch. BOLOMEY. Quantitative images of large biological bodies in microwave tomography by using

numerical and real data. *Electronics Letters* [online]. 1996, 32(23), 2138-2140 [cit. 2020-03-06]. DOI: 10.1049/el:19961409. ISSN 00135194. Available at: https://digital-library.theiet.org/content/journals/10.1049/el_19961409

[24] MENCLOVÁ, Jitka. *Applicator array holder and water bolus for regional hyperthermia system*. Kladno, 2019. Master's Thesis. Czech Technical University in Prague, Faculty of Biomedical Engineering. Supervisor Doc. Dr.-Ing. Jan Vrba, M.Sc.

[25] MÍKOVÁ, Kristýna. *Phantom of pelvic region for regional hyperthermic system*. Kladno, 2019. Bachelor's Thesis. Czech Technical University in Prague, Faculty of Biomedical Engineering. Supervisor Doc. Dr.-Ing. Jan Vrba, M.Sc.

[26] ZUBAL, I. George, Charles R. HARRELL, Eileen O. SMITH, Zachary RATTNER, Gene GINDI a Paul B. HOFFER. Computerized three-dimensional segmented human anatomy. *Medical Physics* [online]. 1994, 21(2), 299-302 [cit. 2020-02-07]. DOI: 10.1118/1.597290. ISSN 00942405. Available at: http://doi.wiley.com/10.1118/1.597290

[27] AKKUS, Oktay. Evaluation of Skin and Subcutaneous Adipose Tissue Thickness for Optimal Insulin Injection. *J Diabetes Metab* [online]. 2012, 03(08) [cit. 2019-10-03]. DOI: 10.4172/2155-6156.1000216. ISSN 21556156. Available at: https://www.omicsonline.org/evaluation-of-skin-and-subcutaneous-adipose-tissue-thickness-for-optimal-insulin-injection-2155-6156.1000216.php?aid=8602

[28] IT'IS FOUNDATION. *Tissue Properties Database V3.0*. 2015, DOI: 10.13099/VIP21000-03-0. Available at: https://www.itis.ethz.ch/virtual-population/tissue-properties/downloads/database-v3-0/

[29] MUN, Peck Shen, Hua Nong TING, Yip Boon CHONG and Teng Aik ONG. Dielectric properties of glycosuria at 0.2-50 GHz using microwave spectroscopy. *Journal of Electromagnetic Waves and Applications* [online]. 2015, 29(17), 2278-2292 [cit. 2019-10-16]. DOI: 10.1080/09205071.2015.1072480. ISSN 0920-5071. Available at: https://www.tandfonline.com/doi/full/10.1080/09205071.2015.1072480

[30] CRUCIANI, S., V. De SANTIS, M. FELIZIANI and F. MARADEI. Cole-Cole vs Debye models for the assessment of electromagnetic fields inside biological tissues produced by wideband EMF sources. *2012 Asia-Pacific Symposium on Elec-*

tromagnetic Compatibility [online]. IEEE, 2012, 2012, , 685-688 [cit. 2019-10-17]. DOI: 10.1109/APEMC.2012.6237915. ISBN 978-1-4577-1557-0. Available at: http://ieeexplore.ieee.org/document/6237915/

[31] Bladder. Organs Of The Body [online]. 2019 [cit. 2019-10-07]. Available at: https://www.organsofthebody.com/bladder/

[32] ANDERSSON, Karl-Erik and Anders ARNER. Urinary Bladder Contraction and Relaxation: Physiology and Pathophysiology. *Physiological Reviews* [online]. 2004, 84(3), 935-986 [cit. 2020-05-10]. DOI: 10.1152/physrev.00038.2003. ISSN 0031-9333. Available at: https://www.physiology.org/doi/10.1152/physrev.00038.2003

[33] SCAPATICCI, R., L. DI DONATO, I. CATAPANO and L. CROCCO. A feasibility study on microwave imaging for brain stroke monitoring. *Progress In Electromagnetics Research B* [online]. 2012, 2012(40), 305–324 [cit. 2017-05-17]. Available at: http://www.jpier.org/PIERB/pierb40/14.12022006.pdf

[34] POZAR, David M. *Microwave Engineering.* 4th ed. USA: John Wiley, 2012. ISBN 978-0-470-63155-3.

[35] HAKENBERG, O. W., LINNE, C. , MANSECK, A. and WIRTH, M. P. (2000), Bladder wall thickness in normal adults and men with mild lower urinary tract symptoms and benign prostatic enlargement. *Neurourol. Urodyn.*, 19: 585-593. [cit. 2019-11-07]

[36] COMSOL Multiphysics. *Material Library* [online]. 2012 [cit. 2020-03-16].

[37] ELLISON, W. J. Permittivity of Pure Water, at Standard Atmospheric Pressure, over the Frequency Range 0–25THz and the Temperature Range 0–100°C. *Journal of Physical and Chemical Reference Data* [online]. 2007, 36(1), 1-18 [cit. 2019-10-29]. DOI: 10.1063/1.2360986. ISSN 0047-2689. Available at: http://aip.scitation.org/doi/10.1063/1.2360986

[38] ARVAS, Ercument and Levent SEVGI. A Tutorial on the Method of Moments [Testing Ourselves]. *IEEE Antennas and Propagation Magazine* [online]. 2012, 54(3), 260-275 [cit. 2020-03-11]. DOI: 10.1109/MAP.2012.6294003. ISSN 1045-9243. Available at: http://ieeexplore.ieee.org/document/6294003/

[39] CHEN, Zhizhang and Michel M. NEY. Method of Moments: A General Framework for Frequency- and Time-domain Numerical Methods. *2007 Workshop on Computational Electromagnetics in Time-Domain* [online]. IEEE, 2007, 2007, , 1-4 [cit. 2020-03-13]. DOI: 10.1109/CEMTD.2007.4373527. ISBN 978-1-4244-1169-6. Available at: http://ieeexplore.ieee.org/document/4373527/

[40] COMSOL Multiphysics. *Reference Guide* Version 4.3, May 2012

[41] LOGAN, Daryl L. *A first course in the finite element method*. 4th ed. United States: Thomson, c2007. ISBN 05-345-5298-6.

[42] GOTHARD, G.K. and F.J. GERMAN. Transmission Line Modeling Method. *Time Domain Electromagnetics* [online]. Elsevier, 1999, 1999, , 237-277 [cit. 2020-03-25]. DOI: 10.1016/B978-012580190-4/50009-4. ISBN 9780125801904. Available at: https://linkinghub.elsevier.com/retrieve/pii/B9780125801904500094

[43] BUCCI, O. M., G. BELLIZZI, I. CATAPANO, L. CROCCO and R. SCAPATICCI. MNP Enhanced Microwave Breast Cancer Imaging: Measurement Constraints and Achievable Performances. *IEEE Antennas and Wireless Propagation Letters* [online]. 2012, 11, 1630-1633 [cit. 2019-11-11]. DOI: 10.1109/LAWP.2012.2236676. ISSN 1536-1225. Available at: http://ieeexplore.ieee.org/document/6395801/

[44] FORD, William. Vector and Matrix Norms. *Numerical Linear Algebra with Applications* [online]. Elsevier, 2015, 2015, 119-144 [cit. 2020-05-06]. DOI: 10.1016/B978-0-12-394435-1.00007-7. ISBN 9780123944351. Available at: https://linkinghub.elsevier.com/retrieve/pii/B9780123944351000077

[45] COLTON, David, Houssem HADDAR a Michele PIANA. The linear sampling method in inverse electromagnetic scattering theory. *Inverse Problems* [online]. 2003, 19(6), S105-S137 [cit. 2020-02-11]. DOI: 10.1088/0266-5611/19/6/057. ISSN 0266-5611. Available at: http://stacks.iop.org/0266-5611/19/i=6/a=057?key=crossref.ae8206004142829958dffeaa93a7163c

[46] SONKA, Milan, Vaclav HLAVAC and Roger BOYLE. Segmentation. *Image Processing, Analysis and Machine Vision* [online]. Boston, MA: Springer US, 1993, 1993, , 112-191 [cit. 2020-05-07]. DOI: 10.1007/978-1-4899-3216-7_5. ISBN 978-0-412-45570-4. Available at: http://link.springer.com/10.1007/978-1-4899-3216-7_5

[47] ZHU, Wen, Nancy ZENG and Ning WANG. Sensitivity, Specificity, Accuracy, Associated Confidence Interval and ROC Analysis with Practical SAS® Implementations. *NorthEast SAS users group, health care and life sciences* [online]. 2010, (01) [cit. 2020-04-28]. Available at: http://www.cpdm.ufpr.br/documentos/ROC.pdf

[48] LI, Shutao and Bin YANG. Region-based multi-focus image fusion. *Image Fusion* [online]. Elsevier, 2008, 2008, , 343-365 [cit. 2020-04-28]. DOI: 10.1016/B978-0-12-372529-5.00009-3. ISBN 9780123725295. Available at: https://linkinghub.elsevier.com/retrieve/pii/B9780123725295000093

[49] HRUBÝ, Vojtěch. *Antenna for Microwave Imaging Methods in Medicine*. Prague, 2019. Master's Thesis. Czech Technical University in Prague, Faculty of Electrical Engineering. Supervisor Prof. Ing. Jan Vrba, CSc.

[50] KAUFMAN, Donald S., William U. SHIPLEY and Adam S. FELDMAN. Bladder cancer. *The Lancet* [online]. 2009, 374(9685), 239-249 [cit. 2020-03-09]. DOI: 10.1016/S0140-6736(09)60491-8. ISSN 01406736. Available at: https://linkinghub.elsevier.com/retrieve/pii/S0140673609604918

[51] LUDMIR, JACK a HARISH M. SEHDEV. Anatomy and Physiology of the Uterine Cervix. *Clinical Obstetrics and Gynecology* [online]. 2000, 43(3), 433-439 [cit. 2020-02-14]. DOI: 10.1097/00003081-200009000-00003. ISSN 0009-9201. Available at: https://insights.ovid.com/crossref?an=00003081-200009000-00003

[52] THE AMERICAN CANCER SOCIETY MEDICAL AND EDITORIAL CONTENT TEAM. Cervical Cancer Stages. *Cancer.org* [online]. Atlanta, Georgia, 2020 [cit. 2020-02-14]. Available at: https://www.cancer.org/cancer/cervical-cancer/detection-diagnosis-staging/staged.html

[53] Gynecologic cancer images. In: *Aboutcancer.com* [online]. [cit. 2020-02-13]. Available at: http://www.aboutcancer.com/gyn_cancer1_abnormal.htm

[54] CHOU, Chung-Kwang, Gang-Wu CHEN, Arthur W. GUY and Kenneth H. LUK. Formulas for preparing phantom muscle tissue at various radiofrequencies. *Bioelectromagnetics* [online]. 1984, 5(4), 435-441 [cit. 2020-01-29]. DOI: 10.1002/bem.2250050408. ISSN 0197-8462. Available at: http://doi.wiley.com/10.1002/bem.2250050408

[55] PARK, Jin-Goo, Sang-Ho LEE, Ju-Suk RYU, Yi-Koan HONG, Tae-Gon KIM a Ahmed A. BUSNAINA. Interfacial and Electrokinetic Characterization of IPA Solutions Related to Semiconductor Wafer Drying and Cleaning. *Journal of The Electrochemical Society* [online]. 2006, 153(9) [cit. 2020-01-29]. DOI: 10.1149/1.2214532. ISSN 00134651. Available at: https://iopscience.iop.org/article/10.1149/1.2214532

[56] DAK 4 MHz to 3 GHz, *SPEAG, Schmid & Partner Engineering AG* [online]. [cit. 2020-02-05]. Available at: https://www.speag.com/products/dak/dak-dielectric-probe-systems/dak-4-mhz-3-ghz/.

[57] *Odpadní potrubí HT* [online]. DEK a.s., 2020 [cit. 2020-05-02]. Available at: https://www.dek.cz/pobocka-kladno/produkty/vypis/15562-odpadni-potrubi-ht

[58] THOMAS, P., R.S. Ernest RAVINDRAN and K.B.R. VARMA. Dielectric properties of Poly(methyl methacrylate)(PMMA)/$CaCu_3Ti_4O_{12}$ composites. *2012 IEEE 10th International Conference on the Properties and Applications of Dielectric Materials* [online]. IEEE, 2012, 2012, , 1-4 [cit. 2020-03-16]. DOI: 10.1109/ICPADM.2012.6319009. ISBN 978-1-4673-2851-7. Available at: http://ieeexplore.ieee.org/document/6319009/

[59] BRANDRUP, J., E. H. IMMERGUT and E. A. GRULKE. *Polymer Handbook*. 2nd Edition. New York: John Wiley, 1975. ISBN 0471481718.

[60] XU, Xu, Camilla BREKKE, Anthony DOULGERIS and Frank MELANDSØ. Numerical Analysis of Microwave Scattering from Layered Sea Ice Based on the Finite Element Method. *Remote Sensing* [online]. 2018, 10(9) [cit. 2020-04-01]. DOI: 10.3390/rs10091332. ISSN 2072-4292. Available at: http://www.mdpi.com/2072-4292/10/9/1332

[61] MOLARIUS, A., J.C. SEIDELL, S. SANS, J. TUOMILEHTO and K. KUULASMAA. Waist and hip circumferences, and waist-hip ratio in 19 populations of the WHO MONICA Project. *International Journal of Obesity* [online]. 1999, 23(2), 116-125 [cit. 2020-05-05]. DOI: 10.1038/sj.ijo.0800772. ISSN 0307-0565. Available at: http://www.nature.com/articles/0800772

[62] DEES-RIBBERS, Hermine M., Anja BETGEN, Floris J. POS, Thelma WITTEVEEN, Peter REMEIJER and Marcel VAN HERK. Inter- and intra-fractional

bladder motion during radiotherapy for bladder cancer: A comparison of full and empty bladders. *Radiotherapy and Oncology* [online]. 2014, 113(2), 254-259 [cit. 2020-05-14]. DOI: 10.1016/j.radonc.2014.08.019. ISSN 01678140. Available at: https://linkinghub.elsevier.com/retrieve/pii/S0167814014003491

List of Figures

List of Tables

List of Appendices

Appendix on CD

Appendix 1 Keywords English (keywords.pdf)

Appendix 2 Abstract English (abstract.pdf)

Appendix 3 Abstract Czech (abstrakt.pdf)

Appendix 4 Master's Thesis Assignment (assignment.pdf)

Appendix 5 Complete Master's Thesis (17PMBDP_434206_Hana_Mozerova.pdf)

Appendix 6 Computational scripts and models:

- scripts and data for the image reconstruction and evaluation
- Solidworks files with measuring system components
- 3D model in COMSOL Multiphysics

Appendix A

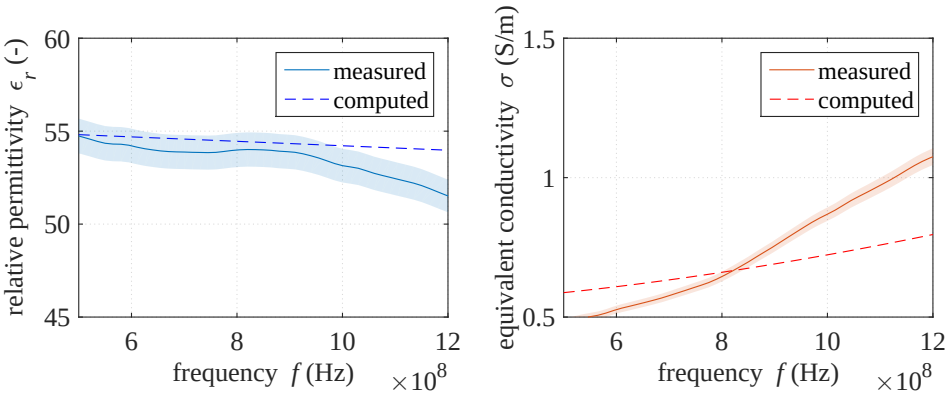

(a) Muscle at 37 °C

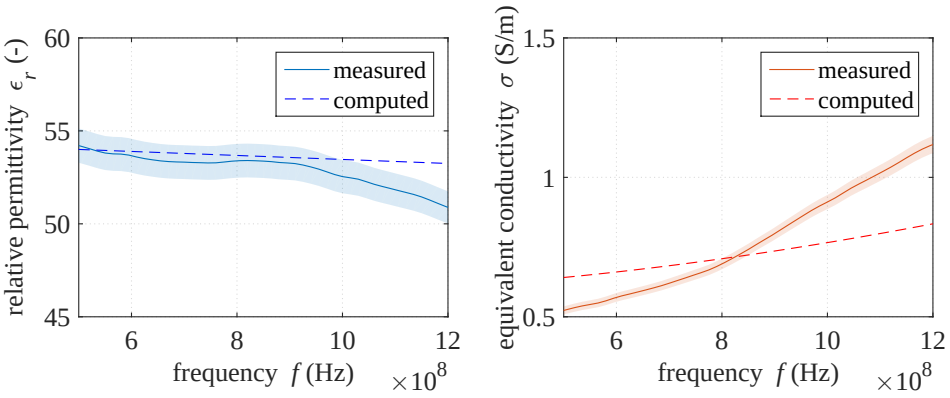

(b) Muscle at 42 °C

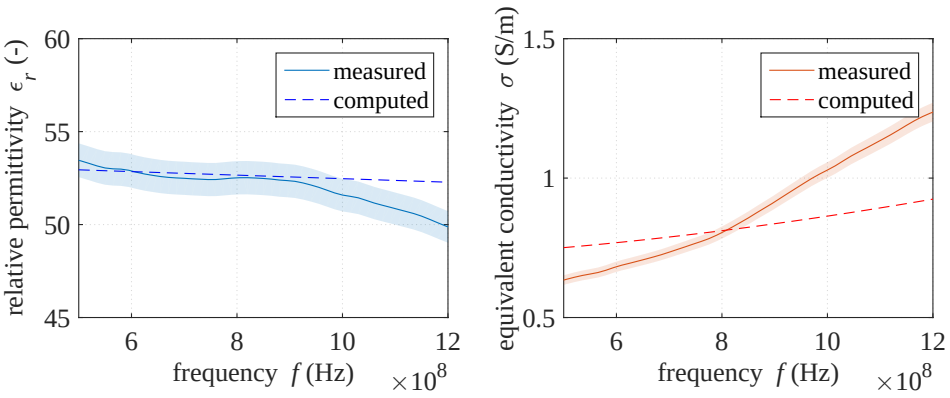

(c) Muscle at 50 °C

Figure 5.1: Measured (continuous line) and computed (dashed line) values of relative permittivity (in the left) and conductivity (in the right) for different muscle temperatures.

Appendix B

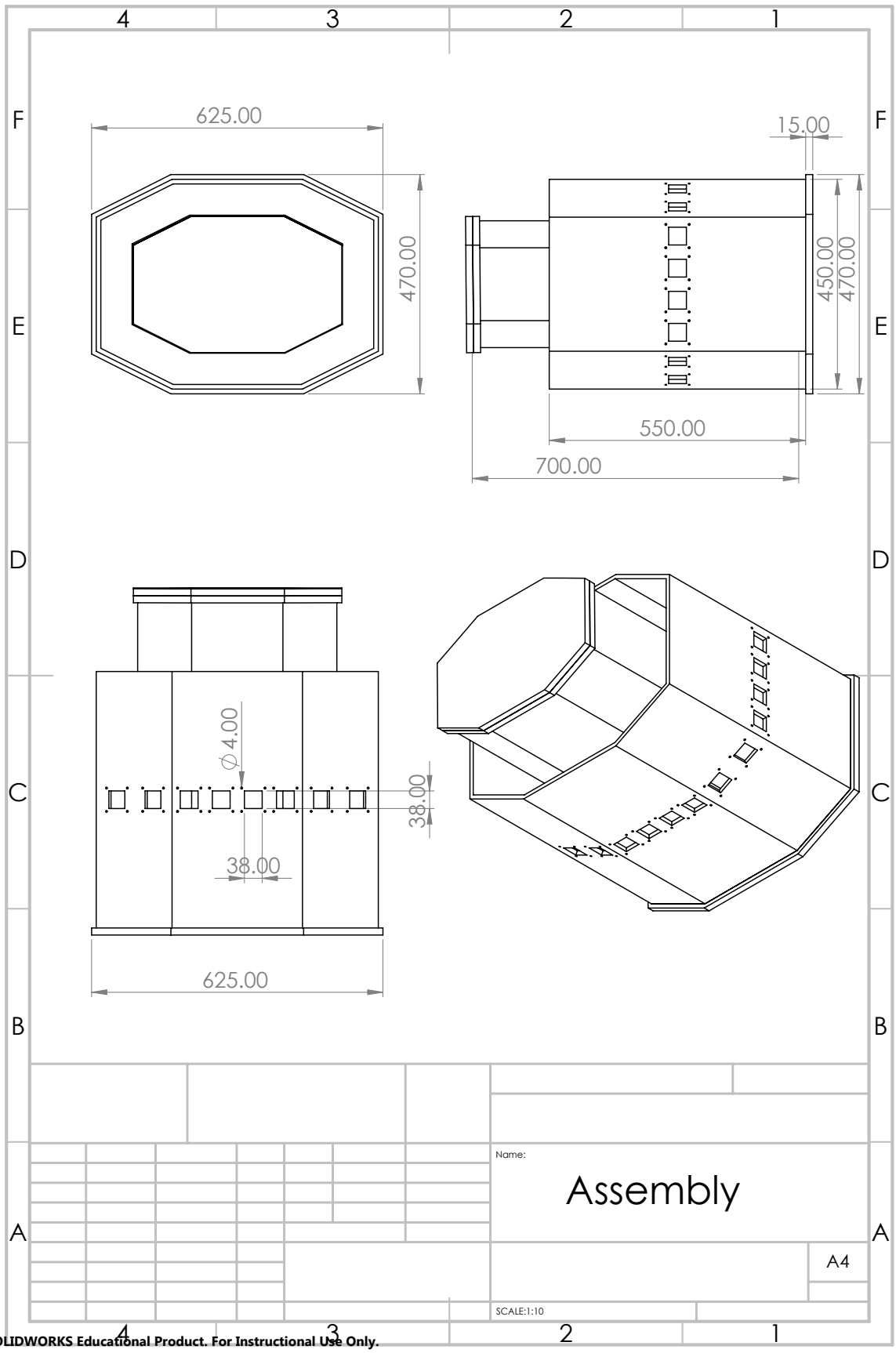

Figure 5.2: Drawing of final assembly of all the parts in the measuring system of plexiglass.

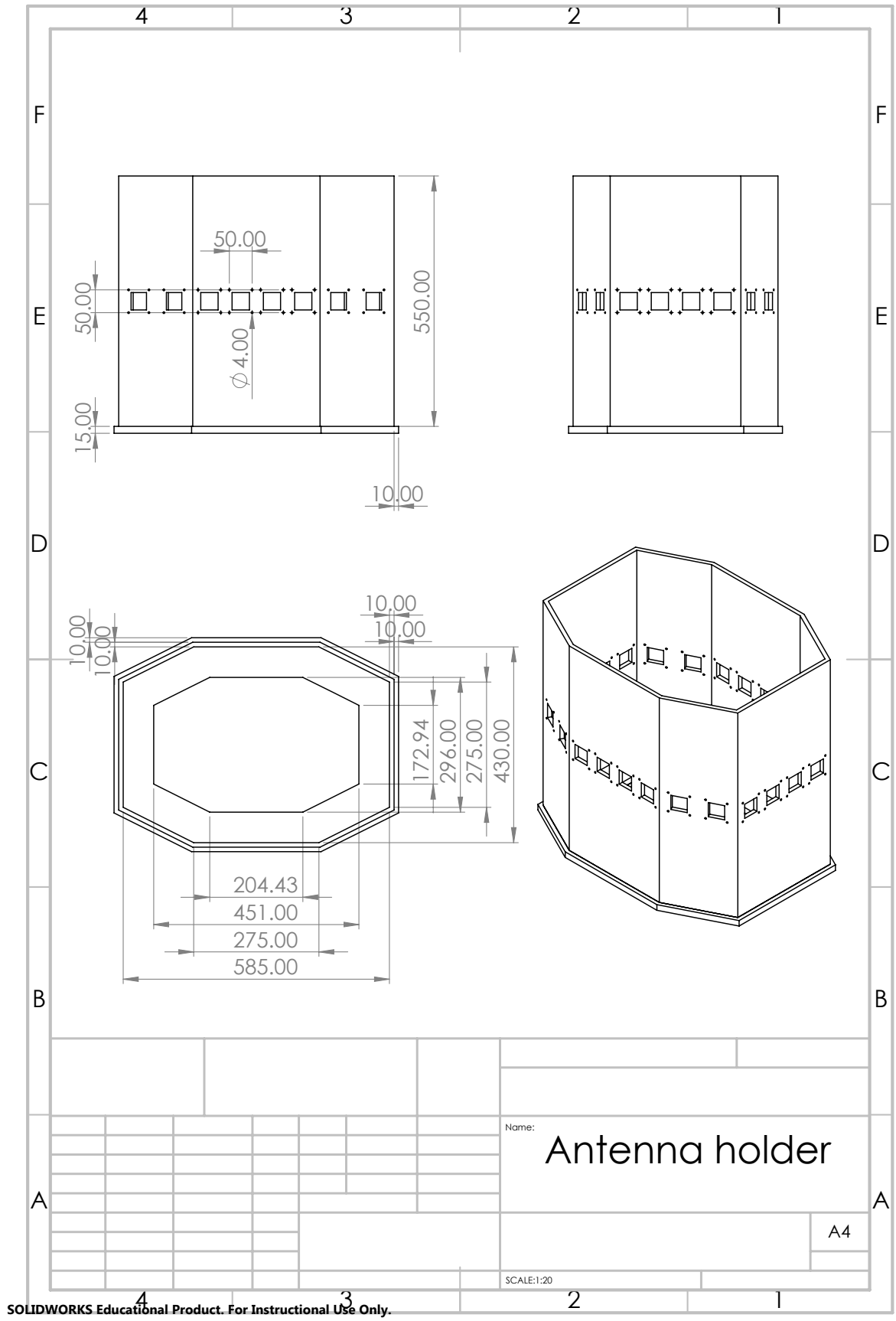

Figure 5.3: Drawing of antenna holder

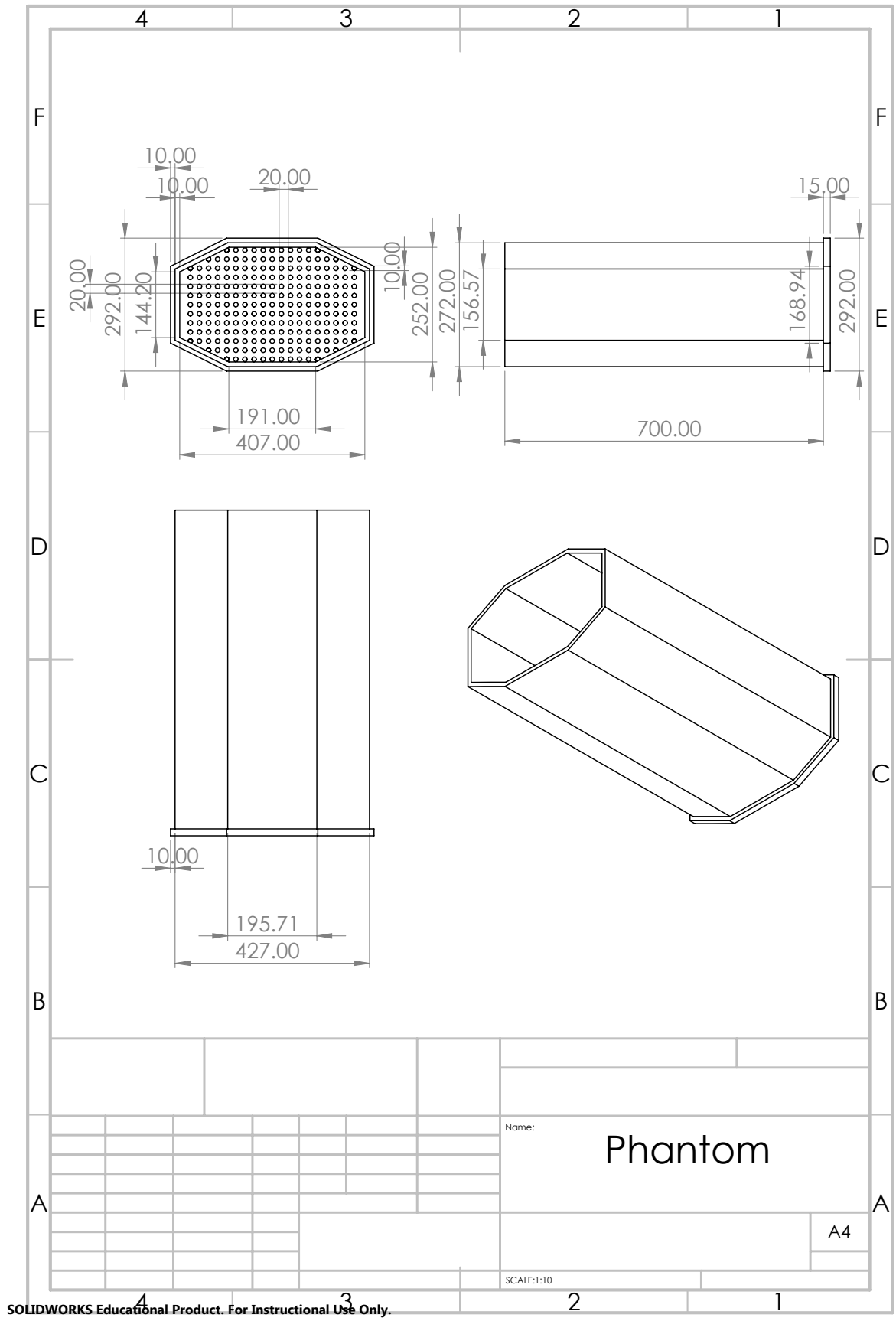

Figure 5.4: Drawing of plexiglass phantom

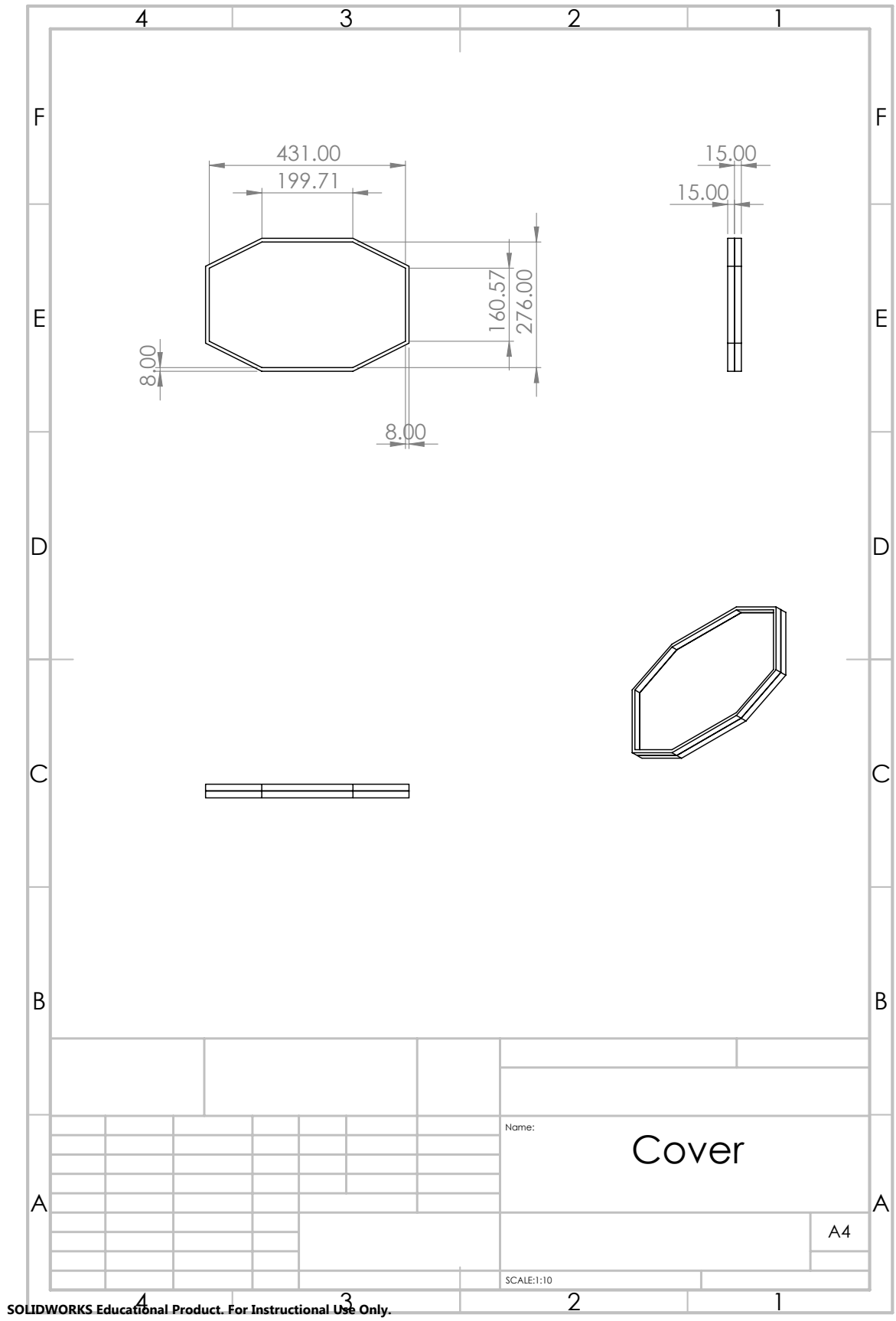

Figure 5.5: Drawing of plexiglass phantom cover